Thermally Actuated Mechanical Systems

Onejae Sul

A dissertation submitted to the faculty of the University of North Carolina at Chapel Hill in partial fulfillment of the requirements for the degree of Doctor of Philosophy in the Department of Physics and Astronomy.

Chapel Hill

2006

Approved by

Sean Washburn

Richard Superfine

Frank Tsui

Jianping Lu

Russell Taylor Jr.

© 2006

Onejae Sul

ABSTRACT

Onejae Sul: Thermally Actuated Mechanical Systems

(Under the direction of Sean Washburn)

This thesis will discuss the generation of controlled sub-micron motions using novel micro actuators. Our research focuses on the development of an arm-type actuator and a free-motion locomotive walking device. Nano-science and nano-technology focuses on the creation of novel functional materials and also at the development of new fabrication techniques incorporating them. In the fields of novel fabrication techniques, manipulations of micron or sub-micron objects by micro actuators have been suggested in the science and engineering societies for mainly two reasons. From a scientific standpoint, new tools enable new prospective sciences, as is evident from the development of the atomic force microscope. From an engineering standpoint, the miniaturization of manipulation tools will require less material and less energy during a material's production. In spite of such importance, progress in the actuator miniaturization is in a primitive state, especially for the micro mobile devices. The thesis will be a key step in pursuit of this goal

with an emphasis on generating motions. Our static actuator uses the excellent elastic properties of multiwall carbon nanotubes as a template for a bimorph system. Deflections in response to temperature variations are demonstrated. The mobile device itself is a bimorph system consisting of thin metal films. Control mechanisms for its velocity and steering are discussed. Finally, fundamental limits on the capabilities of the two devices in a more general sense are discussed under via laws of physics.

ACKNOWLEDGEMENT

To my parents and my academic colleagues.

TABLE OF CONTENTS

Page

LIST OF TABLES……………………………………………………………………………ix

Chapter

1 Driving Force and Surface Forces

1.1 Introduction………………………………………………………..........1

1.2 Origin of Adhesion, Friction, and Magnitude per Contact……………......4

1.3 Continuum Mechanics Models of the Contact Area…………………......8

1.4 Comparison of Surface Forces with Various Actuation Forces and Their Scaling……………………………………………….....11

1.5 Review of Actuators and Mobile Devices………………………………18

1.6 Conclusion……………………………………………………….....22

2 The Locomotive Devices Driven by a Radiometric Thrust and Estimations on Thrust/Friction against Surface

2.1 Introduction to the Radiometric Effect...………………………………...24

2.2 Fabrication (Common to Chapter 3 and Chapter 4)……………………...26

2.3 Experiment Setup…………………………………………………...39

2.4 Proof of Existence of the Radiometric Effect……………………………40

2.5 Driving a Device Using the Radiometric Effect……………………………47

2.6 Finite Element Analysis Simulation on the Magnitude
of a Thrust Based on a Threshold………………………………………...48

2.7 Demonstration of the Translation with the Radiometric
Devices…………………………………………….………………56

2.8 Summary……………………………………………………………………59

3 The Locomotive Devices Driven by a Micro Impact Drive

3.1 Previous Results on Thermal Actuators and Bimorph
Beam Bending Theory………………………………………………60

3.2 Introduction of a Symmetrical Tripod Thermal Walker
Device……………………………………………..…………...63

3.3 Power Delivery and Movement Detection………………………………67

3.4 Proof of the Existence of the Thermal Modulation
Thrust………………………………….……………………..69

3.5 Dynamic Properties of the Devices in Terms of the
Thin Film Mechanics……………………………………………..73

3.6 The Control of the Contraction by the Laser Power and
the Pulse Width for Symmetric Tripid Device……………………....79

3.7 Conclusions in section 3.5 and section 3.6………………………….......83

3.8 Proof on the Inertial Impact Drive……………………………………….84

3.9 Control of Velocity……………………….……………………...……87

3.10 Steering…………………………………………………………..….91

3.11 Behaviors of Devices under Friction……………………………......95

3.12 Consideration on Miniaturization Limits………………………………97

3.13 Summary of Chapter 3…………………..…………………………101

APPENDICES

Appendix A: Metal-Multiwall Carbon Nanotube Bimorph Actuator………………104

Appendix B: Consideration on Small Angle Approximation………………………124

Appendix C: Determination of the Absorptivity of Thin Au Film…………………125

Appendix D: Determination of the Convective Heat Transfer
Coefficient and Thermal Radiative Coefficient…………………………….127

REFERENCES……………………………………………………………………..130

LIST OF FIGURES

FIGURE Page

1.1 Surface tension and contact tip radius……………………………………………………5

1.2 Comparison of magnitudes of the various surface forces…..……………………………12

1.3 Flow chart for quantity relationship……………………………………...………...15

1.4 Power dependencies of various forces……………………………………………...17

1.5 Schematic of the operation of a scratch drive actuator………………………………..22

2.1 Schematic illustrating the radiometric (photophoretic) effect………………………...…26

2.2 Schematics of device fabrication and transfer………………………………………...27

2.3 Screen capture of Seegerizer edit window…………………………………….…...32

2.4 Two peeled and curled up devices after dry etching step……………………………..34

2.5 Substrate for the peel test……………………………………………….……………..35

2.6 Schematic interpretation of the stress variation …………………………………........37

2.7 Adjustment of an initial curvature with a test device….………………………………...37

2.8 Two types of devices standing of flat HOPG surfaces……………………………….…38

2.9 Optics schematics used for control and monitor of curvature of the devices……………………………..…………………………………………….….40

2.10 Five possible mechanisms……………………..………………………………..43

2.11 An angled SEM image of a con-contact device that can be free to wheel around the contact………………………………………………...……46

2.12 Angled picture of a device with the extension……………………………………….48

2.13 Edit window of Femlab3.1i……………………………………………….……..…49

2.14 Model geometry for the simulation……………………………………………..50

2.15 Geometry for radiometric force calcualtion………………………..……...…………54

2.16 Schematics of the staggered walking based on the thrust movements…………………58

2.17 Staggered walking……………………………………………………………………58

3.1 Thermal actuators…………………………………………………………………..….61

3.2 Twisting thermal leg.……………………….………………………………………....61

3.3 Symmetric tripod device and walking modes………………..……………………..65

3.4 Optics diagram to actuate and monitor the motions……………………………..69

3.5 Device used for the actuation test………………………………………………..70

3.6 Band device………………………………………………………………………72

3.7Angled SEM pictures of trapezoid device and a rectangular device…….…………………72

3.8 Deflection dependence on the laser power……………………………………………75

3.9 Measurements of deflections……………………...…………………………………..76

3.10 Simulation of a time constant………………………………………………...………79

3.11 Reflection amplitude measurement with different laser power………..………………79

3.12 Velocity of the tip sliding depending on the laser power…….……………………...80

3.13 Finite element analysis results on the temperature evolution……………………...…...81

3.14 Time evolution of device deformation……….……………………………………82

3.15 Deflection estimation and measurements by reflection…………………………….…..84

3.16 Proof of the inertial impact mechanism……….…………………………………….…....87

3.17 Velocity dependencies on laser parameters…………………………..…….………..90

3.18 Demonstration on steered movements….……………………………………………93

3.19 Velocity dependency on laser location………………………………………..……..95

3.20 Various devices standing with 2 contacts………………………………….….…..98

3.21 Parameter space plot for the device feasibility……………………………………..102

A.1 Cold evaporation……………………………………………………………………109

A.2 Metal depositions on carbon nanotubes……………………………………………..110

A.3 Various Al deposition…………….…………………………………………………110

A.4 SEM sample sledge and button heater……………………………..………………..112

A.5 Diagram of experimental setup………………………..……………………………..112

A.6 Variation of curvature in two cycles of temperature shuttling
between 303K and 473K……………………………………………………………113

A.7 Tube tracing algorithm………………………………………………………………114

A.8 Cross-section of Al film……………………………………………..………………….116

A.9 Simulation of two cross-section models……….……………………………………116

A.10 High magnification TEM pictures on bare…………………………………………...118

A.11 Fit result plot on metal film strain, ζ for each tipchip………..………………………119

A.12 Fit result on thermal strain…………………………………….……………...…121

A.13 Accumulation of amorphous carbon…………………………………………………….121

B.1 Large deflection approximation………………………………………………………..126

LIST OF TABLES

Table Page

1.1 Comparison on the various contact adhesion models……………………………………9

1.2 Scaling laws under classic continuum mechanics with characteristic
magnitudes at L=10nm……………………………………………….…………...……16

2.1 Important input parameters for Seegerizer……………………………………………31

2.2 Parts list……………………………………………………………………………..40

2.3 Theoretical expectations on the actuation by photon momentum transfer………………44

2.4 Observed results in the four conditions…………………………………………………46

2.5 Simulated temperature elevations at the center of the laser spot………………………..52

2.6 Temperature and thrust dependence on the size of a device…………………………….56

3.1 Extended parts list from Table 2.2……………………………………………………69

3.2 Expected results of the actuation test if an under-threshold laser power
is used.…………………………………………………………………………70

3.3 Actuation test results in the four conditions……..……………………………………....71

A.1 Parts list…………………………………………………………………………..112

A.2 Measurements on thickness of metal film, diameter of CNT, bimorph
length, bending angle, and initial curvature calculation with
corrected curvature……………………………………………………………124

A.3 Measurements on thermal bending parameters……………………………………..125

Chapter 1 Driving Forces and Surface Forces

1.1 Introduction

1.1 Motivation, Problems, and Significance of Current Research

Microelectromechanical Systems (in short, MEMS) refers to micro-devices, smaller than 1mm that can sense changes in their environments or can do mechanical work. The development of the MEMS research field runs parallel to the maturity of the silicon based micro-machining technology. Various kinds of MEMS have already been demonstrated in the laboratory. Some devices, such as micro-mirrors in display applications or micro-valves in micro-fluidic systems for medical purposes, are already employed in industry. It will be more beneficial if an arbitrary micro-object can be fabricated by micro-actuators for a better efficiency of substance and energy usage. Fabrication of a microscopic object starts from a macroscopic bulk material. Anyone can easily understand that enormous amount of material and energy is used for creation of a MEMS device. For example, material deposition by evaporation is an important step in MEMS development and the evaporation requires millimeter scale raw materials. But a MEMS device comprises only tiny fraction of the initial material.

If a micro-manufacture is to become feasible, it will need anchored actuators that can pick up and release an object at a desired location, along with mobile devices that can carry a cargo from one location to another. This thesis will discuss the developments of mobile devices with micro-actuations. The mobile function will greatly enhance the applicability of MEMS devices in various environments. Thus the importance of this thesis lies at the expansion of the MEMS capability.

As the start of this thesis, I will address problems. The first problem is the determination of a physical principle to be used for device actuation. I also need to consider non-controlled environmental forces such as adhesion. After this determination, the next problem will be the choice of materials and the realization method. After I have a device, I need to prove the truthfulness of an actuation mechanism based on the chosen principle in controlled environments. For example if I want to use inertial impact drive through thermal modulations, I will test the possibility of movements in various situations to prove the principle. Sudden motion of a portion of a device will generate momentum and the sudden motion will be generated by thermal actuation. Thus the possibility of motion of a device will be different for a constant temperature and for a modulated temperature cycle. I will also investigate the range of valid conditions when the actuation mechanism is effective. The range also defines the miniaturization limit. The method of energy supply to the device and the parameters of the energy source will affect the performance of the device.

From the knowledge supplied by this thesis, I hope that the reader can gain enough information to access the relative strength of thrust required for the successful actuation of a MEMS device compared to the adhesive surface forces present in the context of micro-

mechanics. Although other actuation principles may be adopted for other kinds of actuation devices, the information on force generation and on the magnitude of these forces will be a valuable reference in the design of novel devices. The function of the devices described here can be extended to more complicated tasks such as carrying a cargo. In other respects, this research is a proof for a functional micro-mobile device. Until now, realized mobile micro-devices have been a few in numbers due to the difficulties in device release and mobility. I hope that this thesis and the publications based on it will provoke other research activities.

1.2 Roadmap of Thesis

In this introductory chapter, I will first review origins of adhesion, friction and their magnitudes. I will compare strength of surface forces and various kinds of actuation forces by examining their scaling laws. A model of contact continuum mechanics will be chosen to calculate a contact diameter. From the diameter I can estimate friction of our device. I will continue to review the developments of micro-actuators and locomotive devices, with special focus on the thermally motivated actuation.

In the chapter 2 and 3, I will discuss the design and performance of two types of devices. I will first describe the procedures for device fabrication, which consists of double layer stacks of metal formed by electron beam lithography. After the etching step, the stack is released from the silicon wafer and becomes a non-tethered device. After transferring them onto a substrate, my first task is to isolate an actuation mechanism from a field of several possible explanations based on laser heating. I will find the causes of motion to be radiometric effect and inertial impact. In the chapter 2, I will focus on the radiometric devices. From the nature of the mechanism, the power of a driving laser determines the

thrust, and its critical power is used to determine the friction. From simulation results, I can convert the temperature and its gradient into thrusts. In chapter 3, my discussion will be dedicated to the inertial impact device. Because the two mechanisms are simultaneously effective in air, I will find suitable conditions that permit the rejection of the radiometric force. Momentum is generated by contraction, and laser parameters can control the degree of contraction. Thus I will investigate the control of device performance via the adjustment of various laser parameters. Since the focus of my research is miniaturization, I will find the scaling limit both theoretically and experimentally. At the end of chapter 2 and 3, I will have gained knowledge on a novel method of device fabrication, driving mechanism, the relationship between device performance and laser parameters, and the theoretical and experimental miniaturization limits.

1.2 Origins of Adhesion, Friction, and Magnitude per Contact

Before I determine suitable actuation force for the device, I need to consider the kind and magnitudes of surface forces. Two significant surface forces are van der Waals and capillary force. [1] I will first review origins of each force and their magnitudes.

1.2.1 Natures and Magnitudes of Adhesion Between Contacting Objects

The origins of van der Waals force (in short vdW) have three components; Casimir force, Debye force and London force [2-8]. All are related to the electrostatic interactions between polar and non-polar atom/molecules. vdW force has an effective range from 0.2nm

to 10nm. The magnitude of vdW per unit area between an asperity and a surface is given by equation (1.1) [8].

$$F_{vdW}/(Area) = \frac{A}{6\pi s^3} \quad (1.1)$$

where A is the Hamaker constant of metals, ~4×10^{-19}J/m^2 [9], and s is the separation between the two objects. For most elements, s is in the range 2~7Å [10]; I set s = 5Å. Equation (1.1) gives ~ 0.17nN per square nanometer.

The second force is the capillary force. For every microscopic asperity contacting a flat surface in air, water molecules condense and form a meniscus (Figure 1.1) [5].

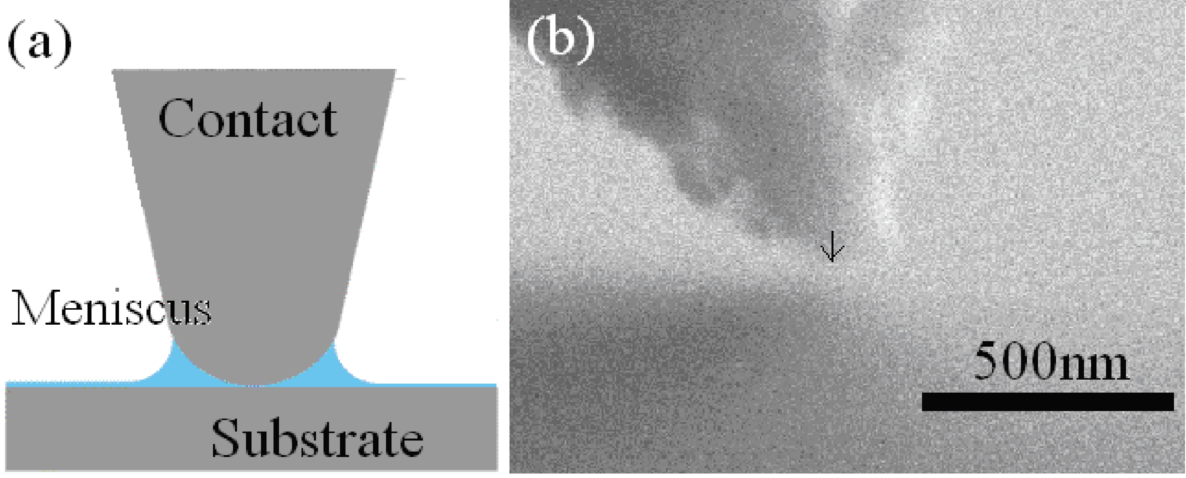

Figure 1.1 Surface tension and contact tip radius. (a) A meniscus formation. (b) An angled SEM image of a contact of a device. The size of an arrow is the radius of a contact, 50nm.

When a contact touches a flat surface covered by a film of water, the film forms a meniscus. The water wets the contact surface because the water-asperity contact is energetically advantageous as compared to the water-air contact. It is intuitively clear that the

curved surface at the meniscus will tend to flatten itself that is available only at the expense of the contact being pulled down. This means that the tip is attracted toward the substrate. Assuming a separation distance much smaller than the asperity radius, the magnitude of this force is give by equation (1.2) [11, 12].

$$F_{cap} = 4\pi r \sigma \cos\theta \quad (1.2)$$

where r is radius of the asperity, σ is the surface energy (surface tension) of water, 0.073J/m^2, and θ is the contact angle of water on the graphite. Taking r as 50nm from a high magnitude SEM (Scanning Electron Microscope) image of a contact (Figure 1.1 (b)), σ, 0.073 J/m^2, and θ for graphite, 86° [13], equation (1.2) gives ~6nN.

The total adhesion will be the sum of vdW and capillary force. If a diameter of contact is 5nm (I will calculate this in 1.3.), vdW force is ~1.5nN. Thus a combined adhesion per contact will be ~7.5nN.

1.2.2 Origin of Friction and Friction on HOPG

The final goal of my project is to actuate a device against friction. Then I need to know the magnitude of friction because the friction will determine a device's performance. Although there is no external load at my device, the adhesion plays the role of the load. This virtual load enforces friction of a device. In this section, I will review the origin of friction and friction coefficient of HOPG (highly oriented pyrolitic graphite), which will be used for substrate.

The search for the origin of friction-related phenomenon dates back to the Leonardo da Vinci's work 500 years ago. The first published article on friction was Amonton's work followed by Coulomb's with the well-known friction law, $F = \mu N$, where the friction force, F, is proportional to the normal load, N, mediated by a friction coefficient, μ. He attributed the origin of the resistance against sliding to be the interlocking of asperities on both objects. According to this view, work spent in raising an object to overcome the asperities could be restored when the asperities found their next minimum energy configurations. This model, however, fails to explain that friction is an energy dissipation process, not an energy conservation process.

An alternative explanation was given by Bowden. His idea is that when two surfaces touch each other, the actual microscopic area of contact is much less than the apparent macroscopic area. Nonetheless, many asperities do come into contact and exhibit very high local yield stresses, like cold-welds. When the surfaces are forced to slide over each other, new contact regions are continuously formed while others are severed. If the load is increased, so does the real contact area with increased friction which explains Amonton's law.

The multiple asperity theory as well as the asperity's plastic deformation [14] can be good theories when contacting surfaces are not flat. But researchers found the ultimate cause of the friction even on the atomically flat surfaces [15-26]. We now believe that friction is a process of energy dissipation through various phenomena; phonon generation [15, 16, 18, 19], electron-hole pair generation [17, 18, 21, 24-26], exchange of photons [20, 23, 27], and charge buildup [22]. Among them, the phononic and electron-hole pair generation causes are dominant when nanoscopic or microscopic contacts are concerned [18, 28, 29].

Because I use HOPG as a substrate, I want to predict the friction of a device onto HOPG. Lateral force microscopy (LFM) has been primary method to measure friction between an atomic force microscope (AFM) tip and a substrate. The AFM tips have nanometer scale tip radius like the contacts of our devices. LFM studies on HOPG showed that the friction coefficients were in the range of 0.01~0.1 [30-35]. In the section 1.2.1, I estimated adhesion per contact to be 7nN. Then the total adhesion per device is around 20nN. I expect that friction per device will be 0.2~2nN.

1.3 Continuum Mechanics Models of the Contact Area.

In this section, I will supplement the vdW force calculation in section 1.2.1 by calculating a contact diameter. If we imagine an asperity contacting a flat surface, an external load applied to the asperity and adhesive surface force between the asperity and the surface will make the tip of the asperity being flat with a diameter. This phenomenon has been described by several different classical continuum mechanics models. Up to now there are four mechanics models to describe a contact diameter: (1) Hertz Model, (2) DMT (Derjagin, Muller, Torpopov) Model [36, 37], (3) JKR (Johnson, Kendall, Roberts) Model [38], and (4) Maugis Model [38, 39]. Table 1.1 shows comparison among the models.

Model	Assumptions	Restrictions	Schematics
Hertz	No Surface Forces	Not applicable to small loads in the presence of surface forces	

DMT	Long-range surface forces act only outside the contact area. Model geometry is same as the Hertz model. Applicable to small high stiffness tip.	Contact area can be decreased due to the limited geometry. Applicable only to small λ.	
JKR	Short-range surface forces act only within the contact area. Applicable to a large radius (macroscopic), small stiffness tip.	Force magnitude can be decreased due to surface forces. Applicable only to large λ.	
Maugis	Tip-sample interface is modeled as a ring.	The solution is analytical but equations are parametric. Applicable to all λ values.	
Actual Interaction	None	In the schematic, vdW interaction is displayed.	

Table 1.1 Comparisons on the various contact adhesion models. For the definition of λ, see equation (1.3). γ is the work of adhesion. Schematics are from Carpick et al [40].

The Herz model assumes that there is no adhesive force between two objects, which is not realistic. Considering the size of the tip and the stiffness of materials, the DMT model fits well to my situation. I can check this with a parameter λ from the Maugis model. The Maugis model can be applied to any situations, but the solution is analytical and depends on a parameter λ. This parameter is an indicator of the closeness to a specific model. For example, if λ is ∞, Maugis model becomes JKR model whereas if λ is 0, it becomes DMT model. This parameter λ is defined by [39],

$$\lambda = \frac{1}{\xi_0}\left(\frac{16r\gamma^2}{\pi K^2}\right)^{\frac{1}{3}} \quad (1.3)$$

where ξ_0 is the interatomic distance, r is the radius of the tip, γ is the work of adhesion, and K is the effective Young's modulus. K is defined by,

$$\frac{1}{K} = \frac{3}{4}\left(\frac{1-\nu^{`2}}{E^{`}} - \frac{1-\nu^2}{E}\right) \quad (1.4)$$

where ν and E are Poisson ratio and Young's modulus for the graphite and Cr. The tip radius was assumed to be same, 50nm. When ξ_0 was set to 5Å and γ from the vdW energy, I have $\lambda = 0.15$, close to the DMT model. From the DMT theory, the relationship between the forces (external and surface force) and contact diameter, a is given by [36],

$$F = \frac{Ka^3}{R} - 2\pi R\gamma \quad (1.5)$$

The DMT model assumes that there is an attractive force by adhesive energy, γ (second term on the right hand side), and an external load, F (the term on the left hand side). Because my devices experience no external load, I can set the force, F as zero. Then I have a = 3nm.

As a cross check, I also want to get the diameter from the Maugis model directly. The equations in the Maugis model are expressed in terms of a parameter, m, which is an indicator denoting how far the model is different from the Hertz model. If there is no interaction between the two objects, m becomes 1; otherwise, it becomes larger than 1 [39].

$$1 = \frac{\lambda a^2}{2}\left(\frac{K}{\pi r^2 \gamma}\right)^{\frac{2}{3}}\left[\sqrt{m^2-1} + (m^2-2)\arctan\sqrt{m^2-1} + \frac{4\lambda a^2}{3}\left(\frac{K}{\pi r^2\gamma}\right)^{\frac{1}{3}}\left[1 - m + \sqrt{m^2-1}\arctan\sqrt{m^2-1}\right]\right] \quad (1.6)$$

$$F = \frac{Ka^3}{r} - \lambda a^2\left(\frac{\pi\gamma K^2}{r}\right)^{\frac{2}{3}}\left[\sqrt{m^2-1} + m^2 \arctan\sqrt{m^2-1}\right] \quad (1.7)$$

Setting the external load, F = 0 in the eq. (1.7), I have two equations on the diameter, a, and parameter, m. By plotting the two graphs from the two equations, I get m = 1.00052 with a =

5nm. From the two models, the contact diameter is around 5nm. This information is used for calculation of the vdW force in section 1.2.1.

1.4 Comparison of Surface Forces with Various Actuation Forces and Their Scaling

1.4.1 Surface Forces between a Spherical Object and a Surface

To compare magnitudes of the above two adhesive forces with other types of forces acting on an object, let me consider the forces between a spherical object and a plane. My devices do not resemble a sphere, but the sphere model is the most simple for calculations and makes comparisons easier on the relative magnitudes of the forces. Besides, any sharp contact can be approximated by a spherical object. For comparison I will also calculate electrostatic and gravitational force.

An approximate electrostatic force between a charged sphere and a conducting plane is given by,

$$F_{elec} = \frac{q^2}{4\pi\varepsilon(2r)^2} \quad (1.8)$$

where q is charge of the sphere, ε is the permittivity of the dielectric material (assumed to be air, 8.85×10^{-12}F/m), and r is the object radius. For the electrostatic force calculation, the assumed surface charge density is ~2.6×10^{-5}Cm^{-2} (discharge limit between conductive sphere and uncharged conductive wall) [41].

The gravitational force is given as,

$$F_{grav} = \frac{4}{3}\pi r^3 \rho_{Al} g \quad (1.9)$$

where $\rho_{Al} = 2700 kgm^{-3}$ is the density of aluminum, g is the gravitational acceleration, $9.8 m/s^2$.

The magnitudes of vdW and capillary force are already given in equation (1.1) and (1.2) in section 1.2, so I will not repeat them here.

Figure 1.2b shows a comparison graph between forces assuming the same radius of an aluminum sphere. Below 1mm, the dominating force is the capillary force followed by vdW force. The electrostatic and gravitational forces are negligible. Based on the dominance of the capillary force, I expect that the capability limitation of a MEMS device due to adhesive and frictional forces will be very different depending on the humidity in the air and the surface energy of absorbate liquid.

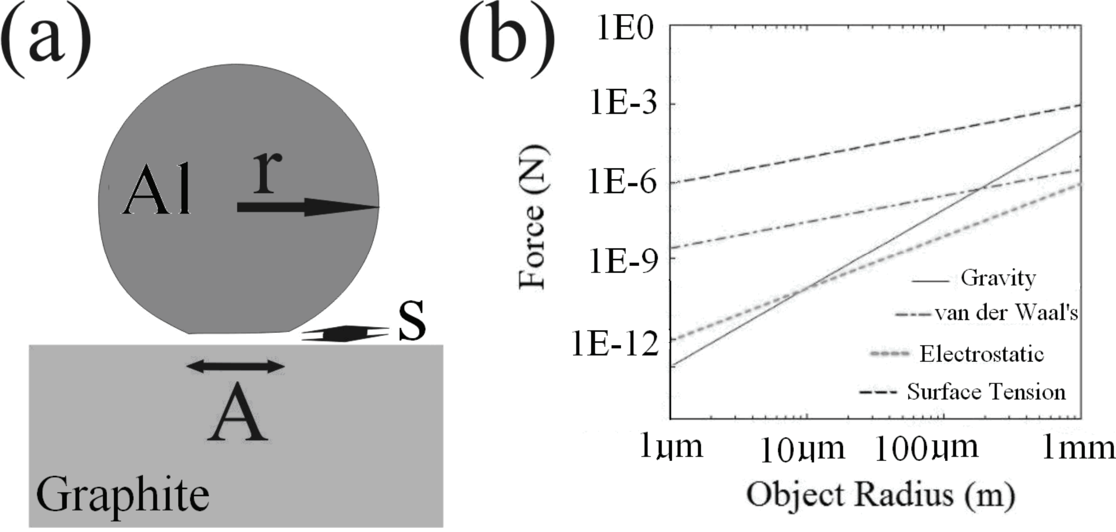

Figure 1.2 Comparison of the magnitudes of the various surface forces. (a) An aluminum sphere with radius, r, is assumed to contact a graphite surface with a gap, s, and a surface area, A. ($A=\pi a^2$, where a is the radius of contact.) (b) A graph from Bohringer et al [1].

1.4.2 Scaling of Various Actuation Forces

Next, I want to consider dependencies of actuation forces on a characteristic dimension, L of a MEMS system. Here I assume that a MEMS system is made of continuous material, because, if a system size is larger than 10nm, the system can be treated by classical mechanics as a continuum rather than a group of atoms. All intrinsic material parameters are assumed to be constant. Extrinsic properties such as volume and mass scale by L^3. A description of scaling laws begins with a choice of a dynamical variable that does not scale. Because I am dealing with forces, natural choices include constant mechanical stress and constant electrostatic field strength. This implies a scale-independent elastic deformation, and a scale–independent shape. Given stress and field strength, both the mechanical force and the electrostatic force will scale with its cross-sectional area,

$$force \propto electrostatic\ force \propto area \propto L^2 \quad (1.10)$$

Adhesion and friction scale with contact area,

$$Adhesion \propto Friction \propto L^2 \quad (1.11)$$

For a magnetic field I need to begin with voltage. Given a scale-invariant electrostatic field strength,

$$voltage \propto electrostatic\ field \cdot length \propto L \quad (1.12)$$

Given the constant electric resistance of a material,

$$resistance \propto \frac{length}{area} \propto L^{-1} \quad (1.13)$$

Thus, the current will be,

$$curent \propto \frac{voltage}{resistance} \propto L^{2} \quad (1.14)$$

Finally power laws of the magnetic field and magnetic force will be,

$$magnetic\ field \propto \frac{current}{distance} \propto L \quad (1.15)$$

$$magnetic\ force \propto area \cdot (magnetic\ field)^{2} \propto L^{4} \quad (1.16)$$

The gravitational force depends on the mass,

$$gravitational\ force \propto L^{3} \quad (1.17)$$

From mechanical force and mass dependency, I have dependency for acceleration,

$$acceleration \propto \frac{force}{mass} \propto L^{-1} \quad (1.18)$$

To obtain frequency, I need to start from stiffness. Stiffness in shear or stretching yields,

$$stiffness \propto \frac{area}{length} \propto L \quad (1.19)$$

Then the frequency of a system will be,

$$frequency \propto \sqrt{\frac{stiffness}{mass}} \propto L^{-1} \quad (1.20)$$

Time is inverse frequency, so I have speed,

$$speed \propto acceleration \cdot time = \text{constant} \quad (1.21)$$

In small scale lubrication, reduction of a thickness of the lubricant layer increases shear rates and hence viscous shear stresses,

$$viscous\ stress\ at\ constant\ speed \propto shear\ rate \propto \frac{speed}{thickness} \propto L^{-1} \quad (1.22)$$

Finally, inertial force will depend on mass and acceleration,

$$InertialForce \propto mass \cdot acceleration \propto L^{2} \quad (1.23)$$

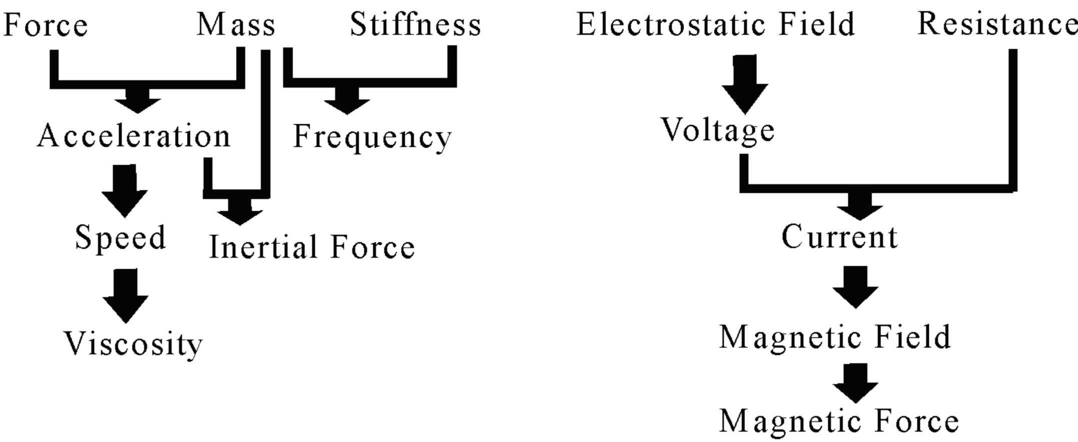

Figure 1.3 Flow chart for quantity relationship.

Name	Power Dependence on Length	Typical value (at 10nm)
Mechanical Force	2	10^{-7}N
Adhesion & Friction	2	10^{-7}N
Electrical Force	2	10^{-11}N
Viscosity	-1	10^{-11}N
Inertia	2	10^{-13}N
Magnetic Force	4	10^{-19}N
Gravitational Force	3	10^{-20}N

Table 1.2 Scaling laws under classic continuum mechanics with characteristic magnitudes at L = 10nm. The typical force values from Drexler [42].

The power dependencies of the above quantities and their typical magnitudes at a 10nm length scale are shown in Table 1.2. Finally I want to compare the magnitudes of surface force with various actuation forces. For that purpose, I calculated the forces in a range of L from 10nm to 1mm. The mechanical force, for example, scales in the power of 2 beginning from 10^{-7}N at 10nm according to Table 1.2. By the same method, all the forces are calculated and plotted in Figure 1.4. One correction to the graph is for the strengths of the adhesion and friction. For a $0.1mm^3$ object such as a dust particle on a surface, the adhesion will be not be 10N as is indicated in Table 1.2, but will still be larger than the gravitational force. For a $1mm^3$ object, the gravitational force becomes larger than adhesive force. Thus the adhesion curve is deflected to match the gravitational force between 0.1mm and 1mm, and the friction is assumed to be 1/10 of the adhesion throughout the whole scale. Based on observation made in Figure 1.4, I can conclude that any force based on mechanical stress will easily dominate adhesion. Thermal stress or electro-mechanical (i.e. piezo) stress are both good candidates for micro-actuation. For free locomotive devices using an inertial impetus, the inertial force will surmount the adhesion at a few tens of microns. If the inertial force were used in a liquid environment, I expect a better limit down to below 100nm.

The gravitational force is too weak to work in the micro-regime. It only matches the adhesive force to scales around 1mm. For this reason, gravity is rarely utilized in the MEMS field. The magnetic force is a good candidate for a MEMS device when it is larger than 10μm, but it can be more useful in fluidic environments as the graph suggests. Viscosity meets the magnetic force around a few hundred nanometers and this has been well demonstrated by the manipulations of magnetic beads in liquids [43]. The electrostatic force has a reasonable strength and many MEMS devices have been designed for this force.

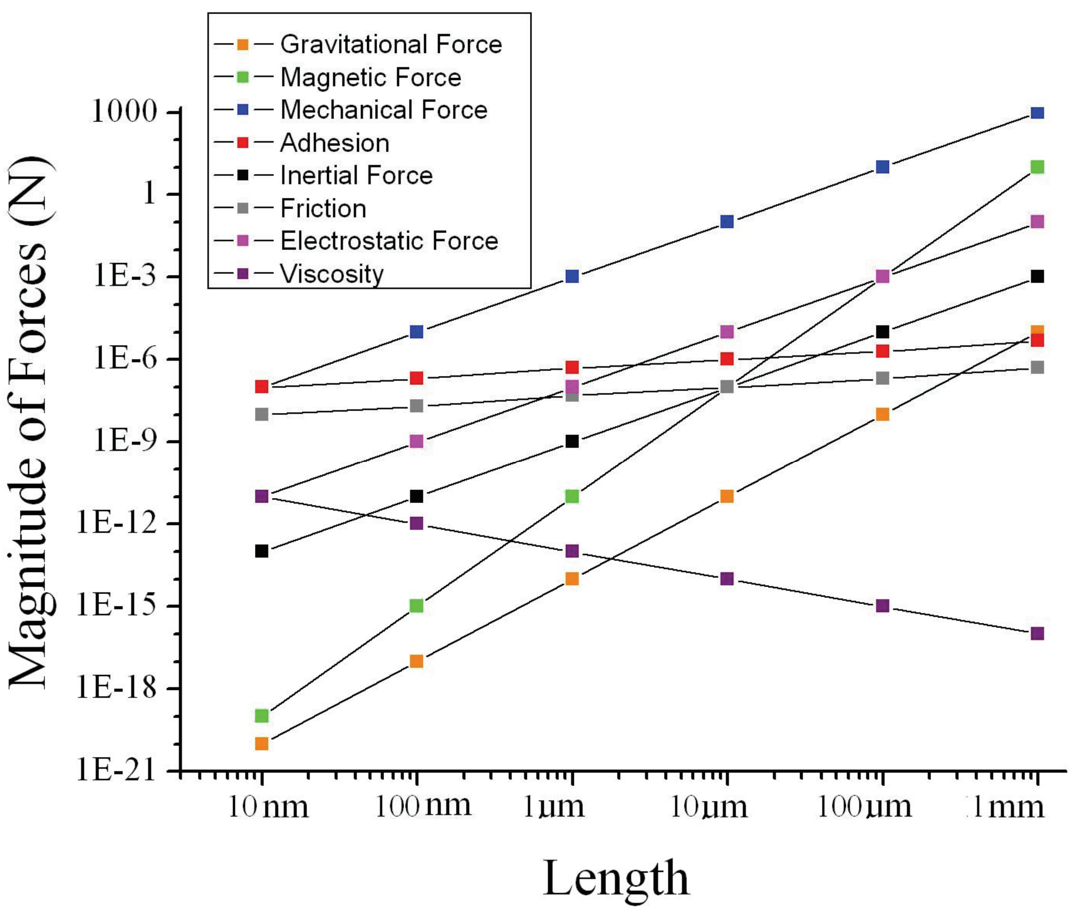

Figure 1.4 Power dependencies of various forces. The coefficient of friction is assumed to be 0.1 uniformly for simplicity. Values at 10nm are from Drexler [42].

1.5 Review of Actuators and Mobile Devices

Although there are numerous types of MEMS actuators, most share a common attribute in their fabrication procedure as they are released from substrates after planar fabrication processes complete. A micro-device is usually fabricated from a silicon or polysilicon substrate in a micro-machining process. Although the fabrication techniques are very diverse, the basic procedure for each includes: A sacrificial layer (often silicon oxide), which is grown, or an etchable film is plated on top of a pure silicon wafer. Next, using photolithography or electron beam lithography, desired patterns of metal films in the shape of a final device are created. After a wet or a dry etching step the sacrificial layer underneath the metal layer is removed so that the devices remain attached to the initial substrate by a support. These attached structures are deformed (i.e. actuated) under a motive force.

There are very diverse kinds of actuators and I will only review briefly here the thermal actuators as they are directly related to my actuation method. I can group actuators by their materials or by application purposes.

By the definition of thermal actuation, materials that generate internal stress under temperature variation are used for mechanical work. In U-shaped actuators, two monolayer pieces of silicon or polysilicon, which have different cross sections, are joined at their ends. Joule heating causes them to extend by different amounts [44, 45]. The unique property of recovering original shape at higher temperature by shape memory alloys (such as TiNi) is

also widely used [46, 47]. Recently polymers have become popular in the fabrication of novel micro-actuators as they provide better thermal expansion rates and accessibility to UV (ultraviolet) and electron beam lithography. In the case of polyimide, the thermal expansion coeffiient is known to be up to 25 times than best metal, Al [48]. Besides polyimide [49-53], polypyrole [54-58], parylene [59], SU-8 [60] have also been used.

If I categorize thermal actuators by application, various kinds have already been developed. For example, mirrors [61-63], conveyer systems [64-75], tweezers [60, 76-78], ciliary system [70, 73-75, 79, 80], and fixtures [81, 82] have been demonstrated. Another interesting application is the manipulation of a biological object in vivo or in vitro. In particular, for the case of manipulating a living cell in a liquid environment, a stricter limitation must be applied on the possible uses of the thermal actuators. Unlike in vitro environment, thermal diffusion in liquid is stronger. Thus this kind of device requires much more power to actuate. Additionally, the temperature of the actuator must be kept low enough not to boil the liquid or to kill the cells [54, 57, 58].

Nanoscience has provided classes of novel micro-scale objects such as nanotubes and nanorods. Their lengths are mostly in the range of tens of micrometers, and their sizes may be useful in the fabricating of micro-actuators. This will enable micro-actuators, not only in terms of actuation ranges but also for the sizes of the entire device. For example, a bimorph is an actuating device, which uses differences of thermal expansion of at least two different materials. Thus the length of the bimorph dictates the amount of deflection. Thus the maximization of deflection based on the size limit of device is a primary concern. The deflection is governed by the internal strain of a layer, and the strain is proportional to

material stress. As I saw from Figure 1.4, the thermally induced mechanical stress is the largest one among various force generating methods. It is therefore natural to choose the thermal bending method for a miniaturized actuator.

The locomotive micro-devices are the core topic of this thesis. A locomotive micro-device is a MEMS device that transforms physical or chemical energy into translation. Fabrication of a locomotive device is more complicated because it has multiple fixed actuators inside of it. Another term, micro-robot, indicates (albeit confusingly) a macroscopic translation device. The term ‘micro-’ in their names means micron in volume, but not necessarily in the length. I will confine the term, locomotive micro-device (or micro-robot) to the devices that are smaller than a millimeter. This research field is currently active, but still far from everyday life applications. Due to their compact size, the micro-robots can do useful work in narrow regimes inaccessible to macroscopic tools. Based on this notion, many possible applications have been suggested in several science/engineering journals [83, 84].

Traveling robots in future can collect, manipulate, and disperse smaller objects with built-in actuators by remote control or under their own intelligence in fluidic environments or on flat surfaces. As far back as several decades ago, typical examples have included the traveling robots for repairing malfunctioned parts inside a machine and for detecting and killing tumor cells inside a human body. However, due to the difficulties in miniaturization of a self-actuating device and also in releasing process after fabrications to overcome surface forces [85-90], this research field is still in a primitive state. Even so, there have been a number of notable reports focusing solely on the locomotive capabilities.

The scratch-drive-actuator (in short, SDA) developed by the Donald group uses the elastic properties of the polysilicon films [91-95]. Since their actuators are electrostatically coupled to one of a pair of conductive surface separated by a non-conducting layer, the L-shaped film deforms itself so that contact area of the longer portion of the shape could be varied repetitively. From the mechanical stress coming from longer portion, the tip of the shorter portion slides a finite distance for every repetition (Figure 1.5). This kind of device has already been developed to maturity and the most recent version is about 200μm long and contains an additional arm to control its relative heading [95].

Another notable result in this field includes a micro-swimmer; it consists of micro-magnetic beads connected in series into a 20μm long oscillator [96]. Based on the magnetic field strength variations, the bead chain waves so that the surrounding fluid can be repelled in a given direction. By adjusting the strength of the oscillating magnetic field and the control of elasticity of the chain, one can control swimming speed.

From this review, I now know that how small the realized devices are and what kind of forces are employed in their actuation. If my research is meaningful in the context of miniaturization history, my device can not be as large as a few hundred micrometers. Also I want my device realized in a novel method of actuation. More importantly I address relative strength of thrust compared to surface forces, which is not well treated in the SDA or micro-swimmer research. I believe that the knowledge obtained in this research will be a first serious treatment of micro-mechanics below 100μm regime.

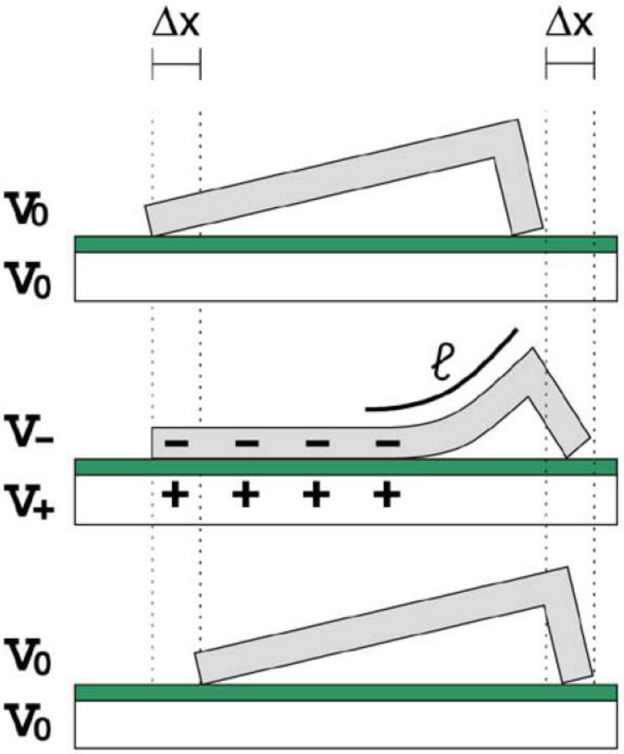

Figure 1.5 Schematic of the operation of a scratch drive actuator. At a parking voltage V_0, the SDA device stands without a deformation (top and bottom). The length of the curved region of the plate, l, and the step size, Δx, are determined by the actuation voltage, V_+ applied on the substrate. Figure from Donald et al [95].

1.6 Conclusion

I reviewed the types and relative magnitudes of surface forces and compared them with various actuation forces. vdW force and capillary force are the most significant surface forces. Among various actuation forces, inertial impact drive is a possible choice in our research. From calculations, the inertial force would be larger than the surface forces above 10μm.

I estimated adhesion and friction per device. Adhesion per device will be 20nN and friction is expected between 200pN to 2nN. Design of our devices requires larger thrusts than

the friction. I also reviewed the developments of various kinds of mobile devices. The development of mobile device will greatly enhance capability of MEMS device. In the context of development history of locomotive device, my research will be the smallest walking device ever built.

Chapter 2 Locomotive Devices Driven by a Radiometric Thrust and Estimations on Thrust/Friction of HOPG Surface

2.1 Introduction to the Radiometric Effect

Although most of this research focuses on devices that use inertial impact as an actuation method, it was also found that there is another mode of actuation, i.e. a radiometric thrust via continuous laser illumination. Because both types of actuations are effective simultaneously under certain conditions, I need to understand how the two mechanisms can be separated. Also, radiometric thrust itself supplies another mode of translation. In this chapter, I will first identify the conditions necessary to isolate one from the other. A critical power threshold capable of driving a device in radiometric thrust is a good measurement for the estimation of friction. Finally, translational motion will be demonstrated and some problems in actuations will be addressed.

Light has been used to propel objects both in air and liquids. Five possible mechanisms of force generation by light energy include photon momentum transfer, laser ablation, levitation due to heated air, the radiometric effect and inertial impact by thermal bending. I identify the

radiometric effect as a possible propulsion mechanism of my device. When light illuminates an object, a temperature gradient is generated inside the object (Figure 2.1). Due to a temperature gradient being present between an illuminated side and a non-illuminated side on a device, air molecules bouncing from the illuminated surface will gain higher energy and transfer relatively greater momentum than the ones from the non-illuminated side. Thus, a net force is generated and this phenomenon is known as the radiometer effect, first discovered by Ehrenhaft in 1918 [97]. The phenomenon has been used as a process of particle collection in fluidic environments, although under a different name, photophoresis [98-101]. In a typical experiment, a spherical bead is charged for levitation against gravity, and it is heated laterally by a laser's energy in a gaseous environment.

Though the magnitude of the force on a spherical bead is well known in free/forced gas convective environments, there has not been any trial of utilizing this force for a locomotive device until now. The radiometric effect has two following advantages. First, it enables fast (on the order of 100μsec) temperature rise/fall in the supply and removal of energy to and from a device. Second, a device is remotely controlled and does not require any additional degree of complexity than a focused laser to generate a thrust. The photophoretic force requires a temperature gradient across a device. Based on the simulations described below, I am guided to fabricate devices with lateral dimensions in the range from 20 to 50 microns. For successful propulsion, the applied force must overcome friction at the point of contact. To minimize the friction, I have chosen a low friction substrate, HOPG as the playground for our devices.

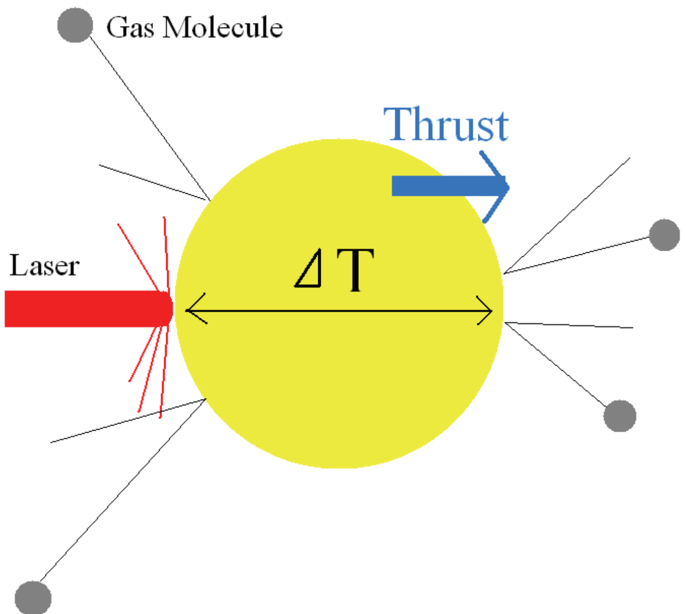

Figure 2.1 Schematic illustrating the radiometric (photophoretic) effect.

2.2 Fabrication (Common to Chapter 2 and Chapter 3)

2.2.1 Substrate Cleaning

The devices are thin metal films prepared on top of a silicon substrate. The silicon wafer is a <100> crystal with arsenic doping. It had a 1μm-thick layer of oxide grown by thermal baking when I bought the wafers from Virginia Silicon, Inc. A wafer was cut into pieces in 3mm by 3mm with a diamond cutter. The wafer pieces are substrates to be used for device fabrication via the electron beam lithograph. I did following cleaning steps before the lithography step.

In a hood, the substrates were rinsed with acetone, methyl alcohol, and water for 10 seconds. After this, any remaining solution was blown dry by pressurized nitrogen gas. To remove organic contaminants, the substrates were placed inside a plasma cleaner at 100W strength about 5 min. In the hood once again, the substrates were rinsed with acetone, methyl

alcohol, and water for 10 seconds each. The whole process described above was done twice to remove contaminants completely.

A polymer based negative mask was used to selectively block metal evaporation. The polymer was PMMA (polymethyl metharcrilate), and has a molecular weight of 1000,000. A PMMA suspension was made in chlorobenzene, 8% by weight. Initial PMMA congregates dissolved after several hours of sonication, resulting in a transparent viscous solution. Drops of PMMA solution were pipetted onto the substrate to cover the surface. The PMMA solution was then spin-coated by a rotational spin coater at 4000rpm for 40 seconds. To evaporate the remaining chlorobenzene, the substrates were left on a hot plate for 5 min. at 170°C. After cooling the substrate in air, the substrates were ready for the electron-beam lithography.

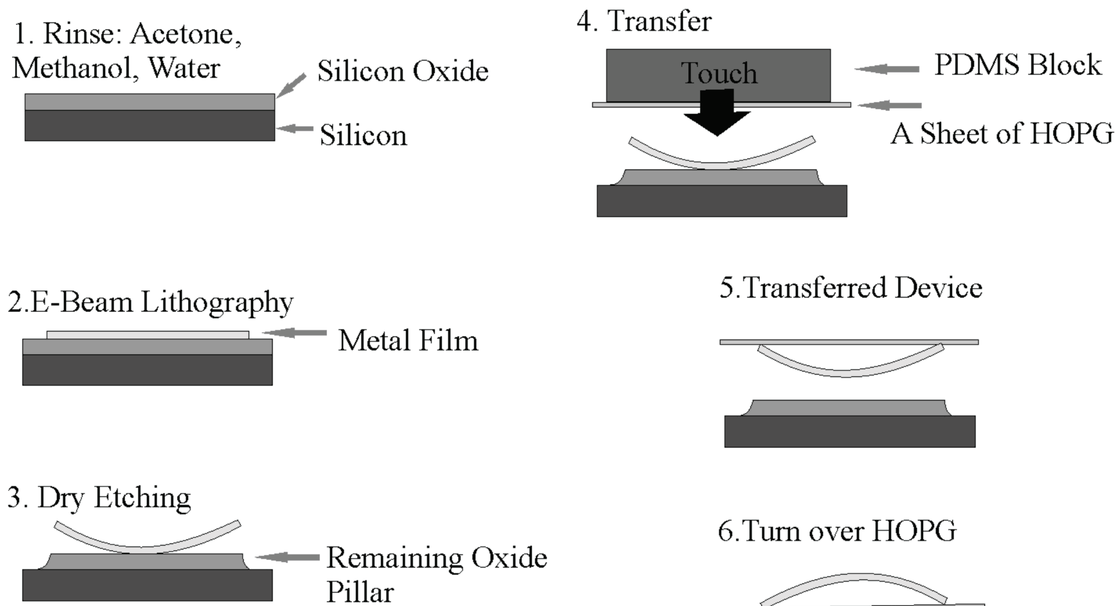

Figure 2.2 Schematics of device fabrication and transfer.

2.2.2 Electron Beam Lithography

The electron beam lithography system is a combination of a field emission scanning electron microscope (FE-SEM, S-4700, Hitachi) with a home-built lithography software, called Seegerizer. The microscope has a resolution of tens of nanometers at 1000X zoom, which is the required precision of this project.

2.2.2.1 Scanning Electron Microscopy (SEM)

The electron microscope uses an electron beam as a probe. The electrons are generated by field emission from a heated filament cathode made of LaB_6. Once the electrons are ejected from the filament, they are accelerated by an electric field. Since the electron can not pass through the air, the path of the particles must remain in vacuum inside the SEM column. To prevent angular spreading of the beam and to focus it, apertures and electromagnetic lenses are used. The aperture is a simple piece of metal with a hole, through which the beam passes. When the aperture is in the middle of the beam with the hole at the center of the beam's axis, the divergence angle of the electron beam outside the beam path will be limited. Thus a narrower beam spreading is obtained. The electromagnetic lens generates a magnetic field to guide the motions of the electrons. The direction of the magnetic field can be determined by the direction of the coil windings in the electromagnet. To focus an electron beam, the coils are wound in a plane that is normal to the beam's direction. The generated magnetic field will be parallel to the direction of the electrons and Faraday's Law will force any stray electrons out of beam axis back to the axis. There are three kinds of the electromagnetic coils; condenser lens coil, objective lens coil, and scanning coil. The condenser lens is relatively weak lens and it determines the focused electron beam spot size. If more current flows in the coil, the strength of the field will be larger making the

beam diameter smaller. The objective lens generates a stronger field providing a focused spot of the electron beam and also adjusts the focal distance. The final type is the scanning coil. It determines the direction of the beam so that the focused beam spot can be laterally rasterized just like the scan line on a television.

When the electron beam strikes surfaces of a specimen, not only are the electrons adsorbed, but they are also ejected from the surfaces. The electrons emerging from a specimen are collected by a positive electric field and fed into an electron detector. The number of electrons collected per unit time will vary from location to location on the specimen surface. Those differences generate an SEM image.

2.2.2.2 Electron Beam Lithography

The size of the electron beam spot is in the nano-meters range. The small size of the spot can be used for fabricating nanometer scale objects. Instead of parallel scanning for the beam in a rectangular frame, the scanning coil can be programmed to deflect the beam in a desired pattern, thus 'writing' on a flat surface as if the beam were being used as a pencil. To deposit solid materials selectively on a surface a mask is needed such as PMMA. The density of the polymer in the solution determines the thickness of the spun layer. I used 8% PMMA, which gave about 1μm thickness. When the polymer layer is exposed to accelerated electrons, the long chains of the polymer molecule are broken, which makes them easier to dissolve in a developer solution, a mixture of 1:3 by MIBK (methyl isobutyl ketone) and IPA (isopropanol). After the lithography, an evaporated material will cover the whole substrate. The material on top of the polymer layer will be removed in the lift-off step while the

material on the bare exposed area will remain on the surface. For the removal of the polymer layer, the substrate was rinsed in acetone for a 10min.

2.2.3 Seegerizer

The 'Seegerizer' software is a lithography tool enabling an SEM user to draw a nanometer scale object on a silicon wafer. It is an interface between the electron microscope and a computer. The Seegerizer controls the lateral motion of the electron beam by controlling the strength of scanning coils in the SEM. As described in the previous section, the SEM can scan in a rectangular shape just like the beam does on a TV screen. Each pixel of the screen has a coordinates and this coordinates can be electrically converted to the strength of the scanning coil current. When a user draws a geometrical pattern in the rectangular screen, the Seegerizer software translates the coordinates into the control current. Any arbitrary shape can be decomposed into simpler shapes such as a rectangle and a polygon. A user can select a line, a rectangle, and a polygon in the software. Any rectangle or polygon can be decomposed again into a collection of dots with some finite inter-dot distance between them. Once the Seegerizer determines the location of each dot, it guides the direction of the electron beam jumping from dot to next dot until all the dots are covered.

The degree of exposure or the amount of charge delivered to a dot is determined by the dwell time and beam current. The dwell time is an amount of time that determines how long the electron beam will stay at a dot. The longer the beam stays in one place, the more charge is delivered. The beam current is the number of electrons per unit time arriving on the surface of the sample. Before any exposure, an SEM user is required to calibrate the beam current using a Faraday cup. The Faraday cup collects all the electrons in the beam and

passes them to a pico-Amp meter. The user can determine how much charge will be transferred to a unit area or unit path length by typing an arbitrary number in the Seegerizer window. If the number is given, Seegerizer can calculate the dwell time for each dot.

The advantage of the Seegerizer over other lithography software (e.g. NPGS (nano pattern generator system)) is that it has versatility in aligning edited patterns on a pre-imaged area. One difficulty of the electron beam lithography is that once the silicon wafer is covered by a PMMA layer, one can not image delicate features on the silicon surface. Only large and thick structures like patterned Au-Cr layers more than 100nm thick can be imaged under the polymer layer. If there is any big landmark such as an Au-Cr pattern, the Seegerizer can use it as a reference mark to align the desired patterns. If an alignment is needed, the user takes images of the intended exposure area before the area is covered by PMMA layer, and uses it as a reference. If such the alignment step is not required, the Seegerizer can be used as a free drawing tool. Below are the parameter inputs frequently used in the lithography.

Name of Parameter	Value	Units
Beam Current	19	pA
Dot Spacing	20	nm
Line Spacing	50	nm
Magnification	1000 (for 12.8cm display)	-
Area Exposure	610	$\mu C/cm^2$
Linear Exposure	1400	pC/cm

Table 2.1 Important input parameters for Seegerizer

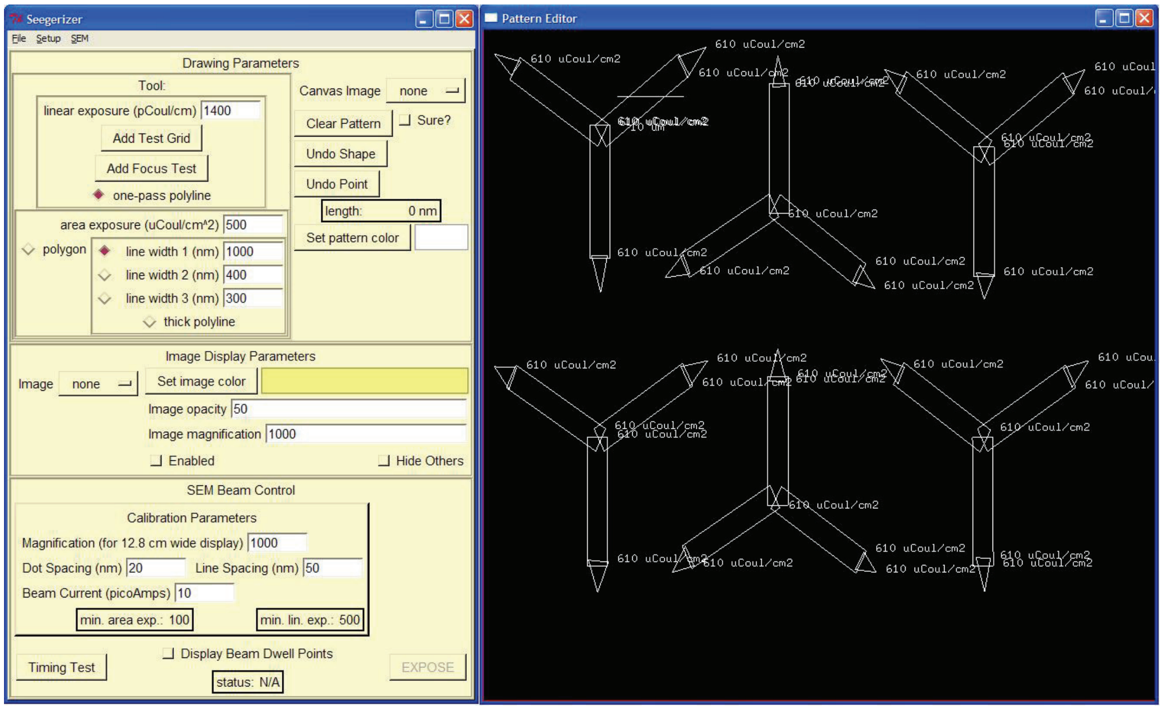

Figure 2.3 Screen capture of Seegerizer edit window

2.2.3 Metal evaporation and Lamination on substrates

A thermal evaporation system from CVC (consolidated vacuum company) developed in 1960's was used to evaporate metals. The materials used were Al, Cr, and Au. The crystal thickness monitoring system had a resolution of a few nm. The vacuum levels were kept under 10^{-5} Torr before evaporation and were maintained at a similar level during evaporation. The evaporation rates were about 100Å/sec for Al, 2Å/sec for Cr, and 5Å/sec for Au, although the evaporation rate is not of great importance. The thickness of each film however was more important ensuring uniformity of a device's deformation under a temperature variation. The thickness of Al was 400±10nm, 200±10nm for Cr, 5±5nm for Au, nominally.

2.2.4 Dry Etching

All of MEMS devices are separated by silicon surfaces by one of several etching techniques. The etching techniques can be divided broadly into two categories, wet and dry etching. For isotropic wet etching, hydrofluoric acid (HF) is commonly used. The three most important anisotropic silicon etchants are potassium hydroxide (KOH), ethylene diamine pyrochatechol (EDP), and tetramethyl ammonium hydroxide (TMAH). These etchants attack silicon along preferred crystallographic directions. The crystallographic plane showing the slowest etch rate is the <111> plane, while the fastest etch occurs into the <100> plane.

Dry etching has several advantages compared to the wet etching techniques. These include smaller undercut regions and higher anisotropy. However, selectivity in dry etching is lower than it is with wet etching. The three basic dry etching techniques; high-pressure plasma etching, reactive ion etching (RIE), and ion milling, utilize different mechanisms to obtain directionality. Ion milling is a purely physical process, which utilizes accelerated inert ions (e.g. Ar^+) striking perpendicular to the surface to remove material. In high-pressure plasma etching, highly reactive species are created that react with the material to be etched. The products of the reaction are volatile so they diffuse away and new materials are exposed to the reactive species. RIE etching, also called 'ion-assisted etching', is a combination of physical and chemical processes. In this technique, the reactive species react with the material only when the bonds of surface materials are broken by the collision of incident ions from the plasma. The directionality of the ion's velocities produces many more collisions with the horizontal surfaces than with the walls, thus generating faster etching rates in the vertical direction.

In my research, wet etching techniques need to be avoided because of the fluidity of the etching solvent. The devices can be lost due to rinsing after etching and capillary force

can exert unnecessary force causing devices to stick to the substrate while drying. I used a reactive ion etching machine (SAMCO RIE) to peel our devices off of silicon oxide surfaces. C_3F_8 gas was used as the etching agent with a flow rate 1.2cc/min. in 8 minutes, 110W power. The dry etching technique initially appears undesirable when considering that there is no undercut beneath the patterned metal devices. However, after the etching step, it was found that roughly 50% of the metal films were curled up from the tip of their spokes. Although dry etching is nominally normal to the surface, some of the etchant gas molecules, C_3F_8, approach the interface of the Au and silicon oxide to initiate separation between the two surfaces. Once a gap starts at the tip of the spoke, the internal metal stress at the spoke raises the separated portion causing the observed curling at the tip. This process continues until the entire portion of the spoke is raised completely except for the center portion that is barely held by the remaining oxide pillar. This can be supported by the observation that the sharp tipped spokes are peeled off more easily than the rectangular-ended spokes.

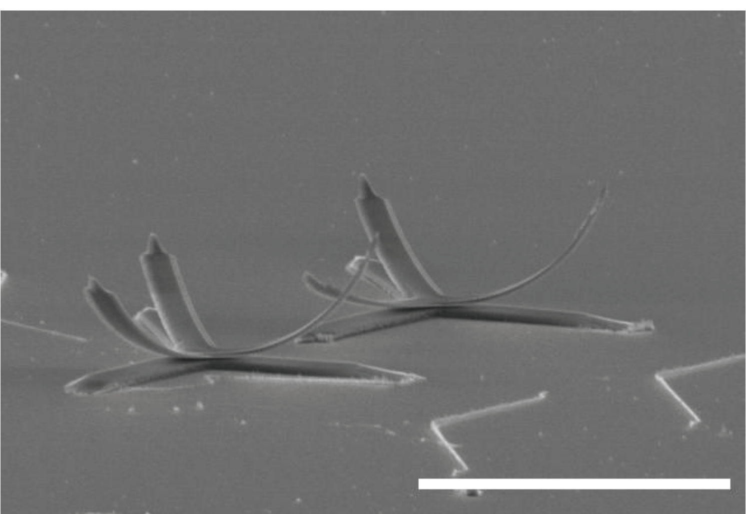

Figure 2.4 Two peeled and curled up devices after dry etching step. Silicon oxide pillars in the device shape are remaining under the devices. The stacks are Cr, Al, and Au from the top. The scale bar is 40μm long.

Of course not all of the patterned metal shapes are easily peeled away. Because the curling process depends on the internal stress of the metal films, if the width of a film is too narrow compared with the total length of a pattern, the film will be remained attached to the surface. If the width is too wide, the curling will happen in an unintended direction. To verify this, an experimental peeling test was done with various aspect ratios (Figure 2.5). The SEM picture teaches two lessons. First, given a finite width, there is a 'limit' on the separation length from the tip of a rectangular pattern (far right column in Figure 2.5). Identical peeling depth is clear in all of the metal films that have various lengths with a constant width. Second, for a complete separation, there is an optimum aspect ratio, about 1/7~1/6 in length versus width (center column in Figure 2.5). Following this rules, I designed all the spokes of the devices to have similar ratios to produce efficient peeling.

This assisted peeling process by dry etching has not yet been reported in any publication, and the exact conditions for better peeling are not studied in depth in this research. Optimization research on this topic should be focused on in future studies.

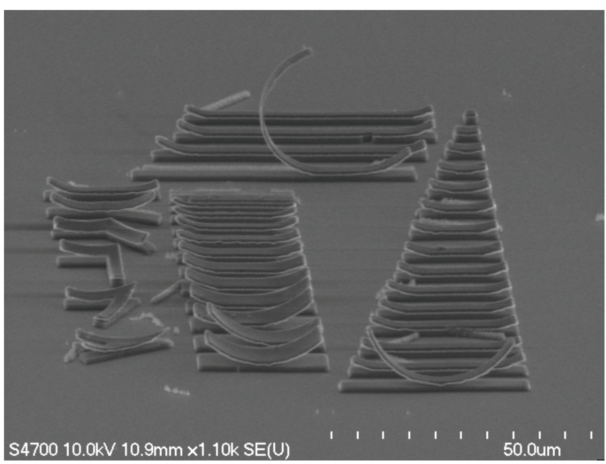

Figure 2.5 Substrate for the peel test. Far right column and center top column have 3μm width. The bottom center column has 20um long for each with various widths from 400nm to 3μm.

2.2.5 Internal Stress of Thin Metal Films

It is well known that the internal stress of thin metal films change under a temperature cycle [102, 103]. Al [104] and Cr [37] films also experience the variations in the stress through baking. The amount of stress variation depends on the maximum temperature achieved during the first baking process. The larger the temperature variation from room temperature, the more stress variation in the film (The first and second thermal cycles in Figure 2.6). After cooling to room temperature, the stress change becomes permanent, and becomes more tensional or compressional depending on metal species. Once the film experienced a saturated permanent stress change, no further baking could induce additional changes, only retracing the same stress curves under subsequent temperature cycles (third and fourth thermal cycles in the Figure 2.6). This is true even when the baking temperature is set higher once the saturation is achieved.

The change in film stress due to baking temperature can be a convenient method for controlling an initial curvature of the devices. After the etching step, if the curvature of a device is too large and the device is relatively flat, the substrate containing the device was put into a tube furnace and baked in air. The temperature range was between 300~500°C above room temperature. Angled SEM pictures verified the variation of the curvature. If the change is not enough, more baking was done by setting a higher temperature in the furnace. This method was used when the length of the spokes in a device is relatively short (circa 10μm). If the length of the legs were large enough, the baking was less necessary.

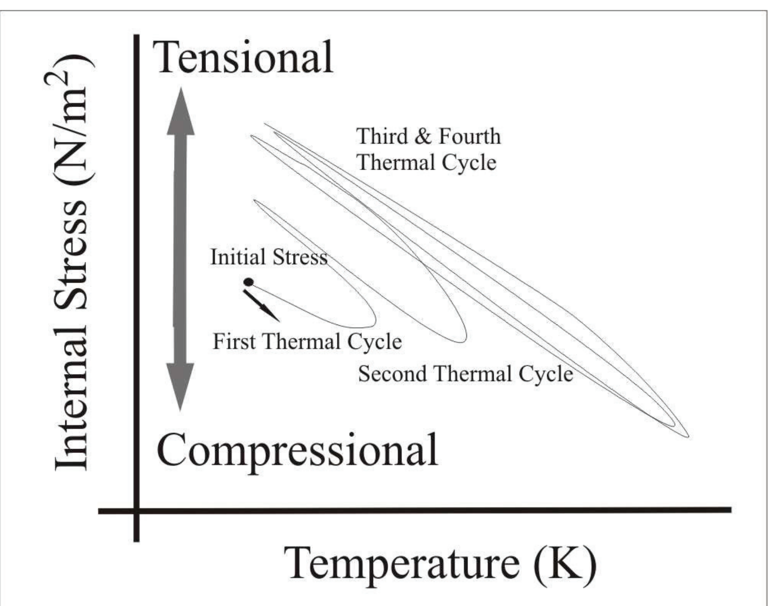

Figure 2.6 Schematic interpretation of the stress variation graph from Hu et al [37]. Starting from an initial stress it undergoes permanent change through first thermal cycle. From the second thermal cycle the stress comes back to its previous newly naturalized value.

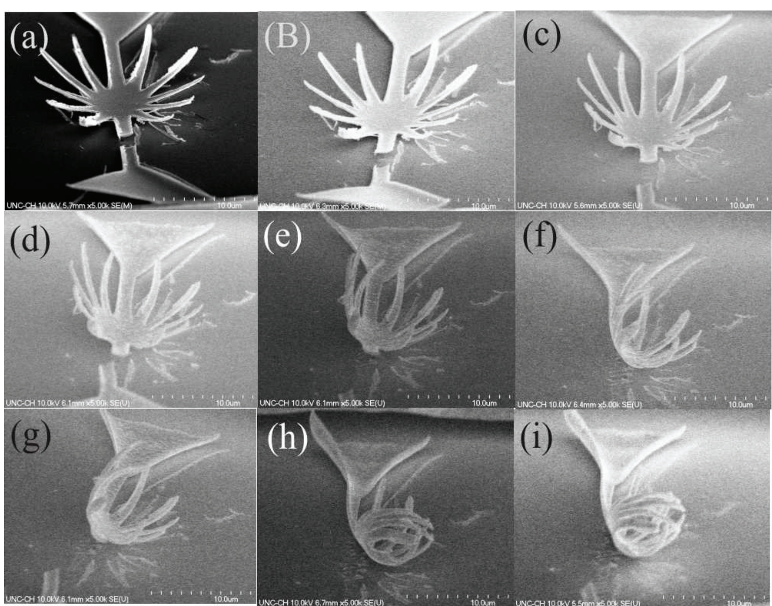

Figure 2.7 Adjustment of an initial curvature with a test device. The claws are made of Al-Cr double layer metal films. Each picture was taken at room temperature after one cycle of temperature change. (a) Right after etching. (b) Furnace set to 50°C (c) Furnace set to 100°C (d) Furnace set to 150°C (e) Furnace set to 200°C (f) Furnace set to 250°C (g) Furnace set to 300°C (h) Furnace set to 400°C (i) Furnace set to 700°C

2.2.6 Graphite sheet preparation and device transfers

A freshly cleaved HOPG sheet was prepared from a piece of HOPG (purchased from GE Advanced Ceramics, pyrolytic graphite, ZYA or ZYB Grade, 12mm by 12mm by 2mm) and used as provided. To cleave a thin film of HOPG, a thin-film sticky tape was prepared and attached on one side of the graphite block in the direction parallel to the graphite's basal plane. Peeling the tape off by hand caused a few layers of HOPG to be separated, providing a fresh surface. The fresh surface was used for the device playground without any surface modification.

The tape-HOPG sheet covered the silicon substrate. A PDMS (polydimethyl siloxane) block was prepared in advance and it was put on top of the HOPG sheet. A gentle press caused the devices to be transferred onto the HOPG by surface forces acting on the spoke tips of the devices. When the devices were transferred they stood with a convex posture (Figure 2.8). Not all of the devices on the silicon substrate were transferred and some devices were broken due to pressure, but some reached clean plateaus of HOPG safely. The overall transfer success rate of a batch, staring from the lithography step, was 10%, but the process itself was found to be highly repeatable, allowing any number of devices to be obtained.

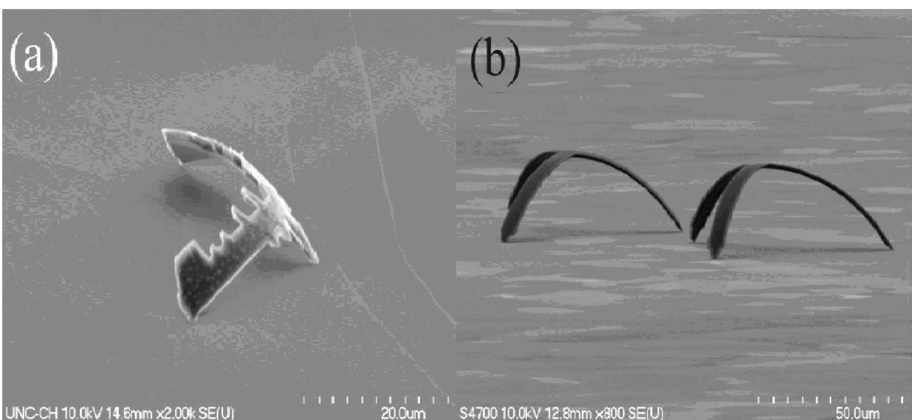

Figure 2.8 Two types of devices standing on flat HOPG surfaces. (a) 'Wing' type device for this chapter. (b) Triangular symmetric devices to be discussed in the chapter 3.

2.3 Experiment Setup

Figure 2.9 is a schematic for the optics setup used for actuating experiments. A 180mW laser was used to control a device's temperature. For visual alignment of a focused laser spot, a CCD camera was used, and for illumination of the substrate, a light bulb was used. Instead of adjusting the locations of the lasers, the substrate was translated by an XYZ stage manually or by a piezo control unit if a fine control of translation is needed.

When a vacuum environment was required, a home-built vacuum chamber was used. The HOPG substrate was attached inside of it, and a glass cover was used to seal the chamber but the background light and lasers can pass through the glass window. I used a mechanical pump and a diffusion pump, which can pump down to 10^{-4}Torrs for a vacuum environment. The vacuum tests in this thesis imply the air pressure level below 10^{-3}Torr.

For the driving of the devices against frictional forces, the power of the actuating laser (L1 in the schematic) becomes important. To keep the amplitude at a maximum throughout the optics setup, polarizing beam splitters were used. Among three beam splitters used in the schematic, BS1 and BS3 were polarizing beam splitters, which have a preferred beam passing orientation and a polarization plane, so that it allows more than 90% of the incident power of the actuating laser to pass. As a result, the laser power directly impinging on the devices was 20±2mW maximum in continuous mode. BS2 is a non-polarizing beam splitter, which passes 50% of power in any direction and polarization so that the CCD camera has enough brightness from reflection.

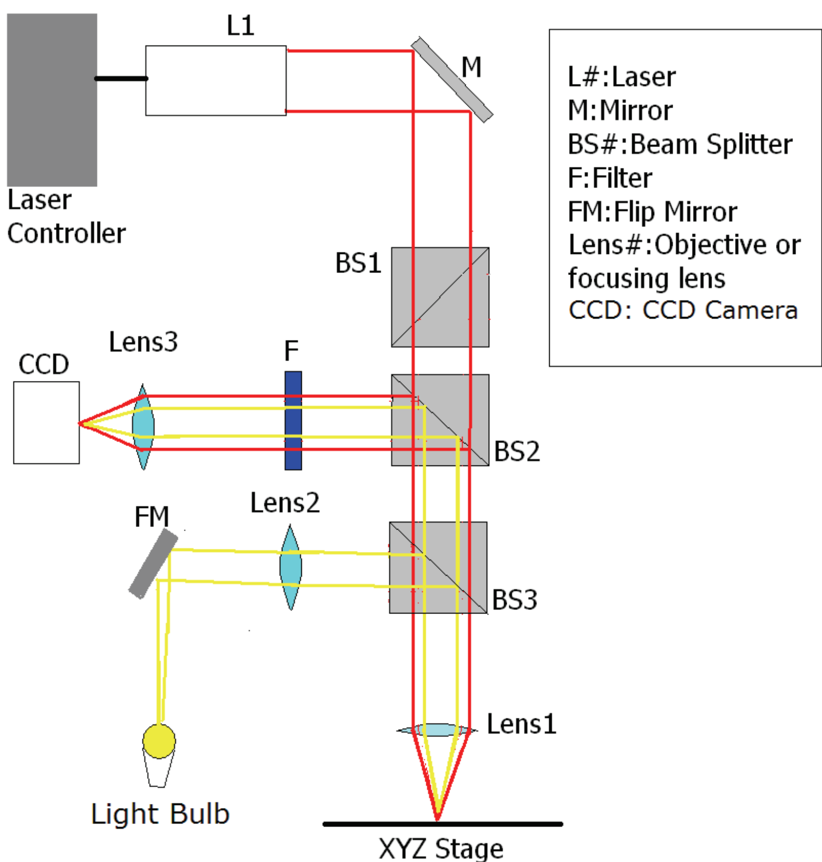

Figure 2.9 Optics schematics used for control and monitor of curvature of the devices.

Item	Catalog	Company
Laser 1 (L1)	DL7147-201, 660nm, 180mW	Thorlabs
Laser Controller	LDC2000	Thorlabs
Objective Lens	M Plan Apo 50	Mitutoyo
Beam Splitter (Non Polarizaing)	U47-122	Edmund Optics
Beam Splitter (Polarizing)	P47-125	Edmund Optics
XYZ Stage	360-90	Newport
Piezo Control Unit	MDT 690	Thorlabs
Pulse Generator	8005B	Hewlett Packard
CCD Camera	WAT-902C	
HOPG	Grade ZYA, ZYB	Advanced Ceramics

Table 2.2 Parts list

2.4 Proof of Existence of the Radiometric Effect

2.4.1 Candidate Theories to Explain the Motions

In theory, there are 5 possible candidate mechanisms; the radiometric effect, photon momentum transfer, inertial impact drive by repeated thermal modulation, ablation, and pneumatic pressure by a free heat convection.

Before discussing the proof of a particular mechanism, I will review the principles of each mechanism briefly. According to Planck's well known theory of the quanta of light [105], the particles called photons have momentum like any other materialistic particles such as protons and electrons. They move straight in space and at the surface of an object, some portions of the photons are absorbed in the form of heat energy, while the rest of them are reflected. When they rebound, their momenta are transferred like colliding macroscopic balls. Thus the illuminated object gains the same amount of momentum. Although a momentum transfer from one single photon is tiny, if the number of photons is enormous, the sum of their momenta cannot be ignored. In my experiment, friction of nano-contacts between a device and graphite will be on the order of nN, so there is a possibility for the photons to drive our devices. According to the LFM (lateral force microscopy) studies done in air on HOPG [106, 107], the magnitude of friction on graphite from point tips of AFM cantilevers is various from 100pN to 1nN. The momentum of a light particle, p, is given as, $p = E/c$, where E is the energy and c is the speed of light. The energy of the laser that directly hits the surface of our device is about 20mW, which gives about 30pN. This number is a little bit smaller than the friction expected, but there is still room for the possibility of locomotion via momentum transfer.

Because an introduction to the radiometric effect is already presented in section 2.1, it will not be repeated here. Concerning of the magnitude of the thrust, I can predict

numerically how large the thrust will be by a finite element analysis simulation study when the power of the laser is known.

Another strong candidate is the thermal modulation. As was described in the introductory chapter, my devices have two different metal films attached to each other. I used Al and Cr among other metals for their greatest differences in their thermal expansion coefficients. Thus, depending on the temperature change, the curvature of the bimorph will modulate. The estimated thrusts will be given in chapter 3, but the magnitude is well above the HOPG friction. Instead, the primary concern is the role of the contact tips. It is not expected that the cantilever's full deflection force will be used to push/pull a device, but it is expected that primarily the contact tips will slide on the surface. Only tiny fractions of this force will be used in an actuation.

The energy of the laser can quickly raise the temperature to the melting temperature of Al (933K) and my devices are basically thin films rather than a bulk. As a result, the actual melting temperature can be a lot lower than melting point of bulk for both Al and Cr. If a metal surface melts down, the evaporated gas will gain momentum. Thus by the Newton's third law, the device will gain momentum.

Finally, pneumatic pressure can be another candidate. Due to heating of the surrounding air molecules energized by a hot metal surface, the air flow speed of the top and bottom sides will be different. By Bernoulli's principle, a pressure difference attempts to levitate a device. Usually, the body of the device has a slope angle against the substrate and because the device is adhered to HOPG, then a lateral directional thrust is generated.

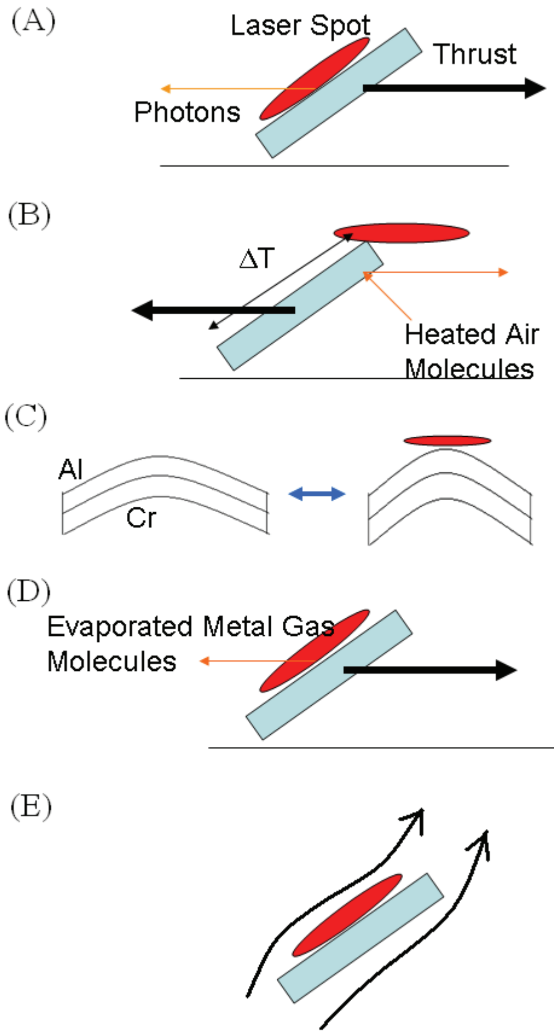

Figure 2.10 Five possible mechanisms: (a) Photon momentum transfer (b) Radiometric effect (c) Inertial impact by repetitive thermal modulation (d) Ablation (e) Air pressure difference generated by natural heat convection.

2.4.2 Examinations of Each Mechanism

I will examine each candidate theory one by one under different conditions. The first one I will consider is the pneumatic pressure. The magnitude of the pneumatic pressure will be $\Delta p = \frac{1}{2}\rho(v_{top}^2 - v_{bottom}^2)$ from the Bernoulli's equation, where Δp is the pneumatic pressure difference between the top and bottom of a device surface, ρ is density of air per unit volume, 0.44kg/m^3, and v_{top} and v_{bottom} are the air flow velocities near top and bottom plate of

the device. The velocities will depend on the device temperature and the incline of a device against the substrate. Given an inclination, the velocities can be roughly calculated at the top/bottom surfaces [108, 109]. From simulation results a typical temperature elevation was up to around 500K. If the estimation is correct, the calculated maximum velocities around the device were in the order of 1mm/sec. Then the pressure will be smaller than $2\times10^{-7}N/m^2$ according to the Bernoulli's equation. Since a total area of a typical device is $\sim1\times10^{-7}m^2$, a thrust will be smaller than $2\times10^{-14}N$. This is a factor of 10^3 smaller than the friction ever measured by LFM studies on graphite. Therefore we can safely reject the pneumatic pressure as a cause of thrust.

For ablation exclusion, SEM pictures on the surface of a device after many actuations show no damage. Thus I can safely reject ablation as a possibility.

To examine the remaining mechanisms, I tested in 4 parameter spaces. Those are: (1) Laser in continuous wave mode (CW mode) and in air, (2) Laser in CW mode and in vacuum, (3) Laser in modulation and in air, (4) Laser in modulation and in vacuum. The cells below in Table 2.3 will clearly show the expectations by all the theories in each condition.

Expectation under 4 conditions	Photon Momentum Transfer	Radiometric Effect	Inertial Impact by Thermal Modulation
Air, CW	Y	Y	N
Vacuum, CW	Y	N	N
Air, Modulation	Y	Y	Y
Vacuum, Modulation	Y	N	N

Table 2.3 Theoretical expectations on the actuation by photon momentum transfer, radiometric, and thermal modulation. Y means that an actuation will be shown in that condition. N means that an actuation will not take place in the condition.

For the photon momentum transfer, as long as the power of the laser is kept above a critical power, devices will move in all of the conditions in Table 2.3. The acquired

momentum only needs to surpass surface friction. If the laser is modulated with a frequency, the motion will be stepwise. But if the frequency is fast enough, it will appear as continuous mode driving. If the radiometric effect is the cause, there always needs to be an environmental gas surrounding the devices. Therefore no movement will be observed in vacuum condition. The inertial impact theory always requires a modulated laser.

Now the test results will be discussed in comparison to the theoretical predictions. To exclude the photon momentum theory, the observation result in CW and vacuum will be sufficient. Unlike the radiometric and the inertial impact effects, the photon momentum deflection predicts that there will be motions in CW, vacuum condition. I observed no actuation in that condition. The actuation test is complicated by the fact that, in vacuum there is no gas acting as a coolant preventing meltdown. However, there was an appropriate level of the laser power in which devices did not melt in the vacuum. Figure 2.11 shows an SEM picture of such a device that was actually being tested. The device in the picture is a T-shaped device, unintentionally standing after the device transfer process by one contact on the graphite. The attractive interacting force was enough to hold the device without making it fallen down. Therefore it can wheel freely around the contact. In the test, a laser spot with a known laser power was brought to a side of one wing of the device and a torque was generated to rotate it. This task was done first in air, second in vacuum and finally in air again with all the same power in continuous mode. The actuation test result shows that under a continuous laser mode, the device was able to turn in air first, next in vacuum it did not show any movement, but finally in air it could be rotated again.

For the remaining two models, I will prove the existences of both the radiometric thrust and the inertial impact thrust. To isolate them, I need to test at CW in air and

modulation in vacuum. I found that actuations were observed in both cases, which is impossible for either model alone. The inevitable conclusion is that both mechanisms exist and each can be isolated at CW in air or modulation in vacuum. When modulations are performed in air, both mechanisms will be in effect simultaneously. To remove the ambiguity, all actuations in air were done with the continuous mode above the threshold for the devices in this chapter.

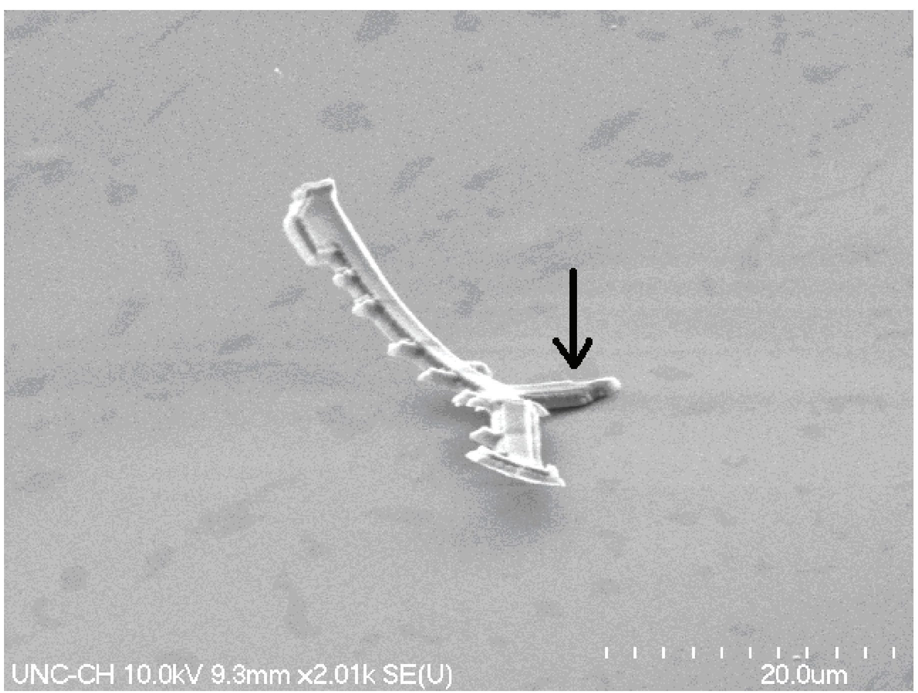

2.11 An angled SEM image of a one-contact device that can be free to wheel around the contact. The arrow in the picture indicates the location of the contact. The small spikes on the wings are heat diffusion pins.

	CW	Modulation
Air	Y (Above critical power) N (Below critical power)	Y
Vacuum	N (Or melting)	Y

Table 2.4 Observed results in the four conditions.

2.5 Driving a Device Using the Radiometric Effect

When driven by the radiometric effect, a device responded to a laser spot by rebounding from the spot. As soon as a laser spot touched an edge of a device, the device was shoved away. But it was not a parallel translation following the direction of the laser's motion. Instead the devices rotated around one of the contacts. It is hard to predict which contact would be a pivot point, but in many cases, the farthest tip from the laser was the pivot point. The possibility of a laser driving actuation strongly depends on a power of the laser; i.e., there is a critical power for a device, which depends on the device size. To discuss the threshold numerically, I must to choose a specific device of this size. As shown in Figure 2.12, the device we chose had a dimension of 20μm in the long axis, and had two arms with sharp tips at the ends of them. Additionally, there was another tip at the center tail. Those three tips were touching the graphite surface. Because the tips are far away from each other, one could be a pivot and the other tip slid when the arm is driven radiometrically by a laser spot nearby.

To increase a temperature gradient, two square pads were prepared in both arms. Heat sink pins are added to suppress overall temperature rise to remain below the melting point. The purpose of the hairpins was to prevent the sticking of the devices to the surface by tip annealing due to a high temperature, but the effectiveness of these heatsinks was not tested. For the measurement of a threshold, a continuous mode laser spot was brought to an edge of one of the pads. The amplitude was 10.0±0.4mW for a specific device shown in Figure 2.12a. Below this critical value the device did not respond to the laser.

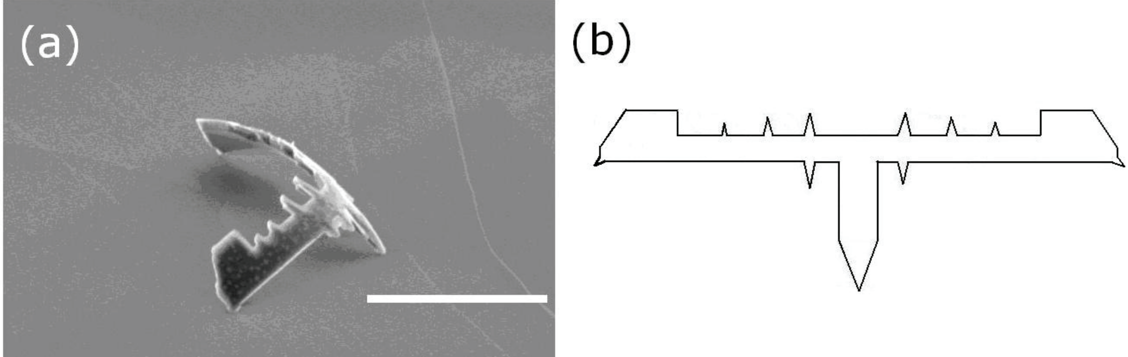

Figure 2.12 Angled picture of a device with the extension. (a) An angled SEM picture of a device with many heat diffusion pins. The scale bar is 15μm long. (b) A schematic pattern of the device. The distance from a tip of one arm to the other is 20μm.

2.6 Finite Element Analysis Simulation on the Magnitude of a Thrust based on a Threshold

2.6.1 Temperature Simulation using a Finite Element Analysis Tool

Femlab 3.1i was used as a finite element analysis (FEA) tool (Comsol, Inc.). The general procedures for the simulation were: (1) Choice of specific physical model to be used. For the temperature simulation, I used 'Heat Transfer by Conduction' model. (2) In the drawing mode, the geometric objects close to the real objects were created. (3) In the boundary mode (surfaces of the objects) and sub-boundary mode (edges of the objects), properties of the materials, initial conditions of the physical parameters, and boundary conditions were given. (4) In the mesh mode, the geometries were divided into smaller tetrahedra. (5) In the simulation mode, Femlab calculates the physical quantities from the initial conditions. (6) Finally, Femlab displays requested physical quantities in visualization. An example of temperature elevation simulation is shown in Figure 2.13.

The geometry for the simulation is a simple rectangular box. For simplicity it is assumed to be flat rather than curved, but the total length, width, and thickness followed the actual dimensions. The schematic for the geometry is shown in the Figure 2.14. A laser illumination area was assumed to be at a corner of the top plate, and its power was about to be equal to the actual laser spot area (shaded region in Figure 2.14).

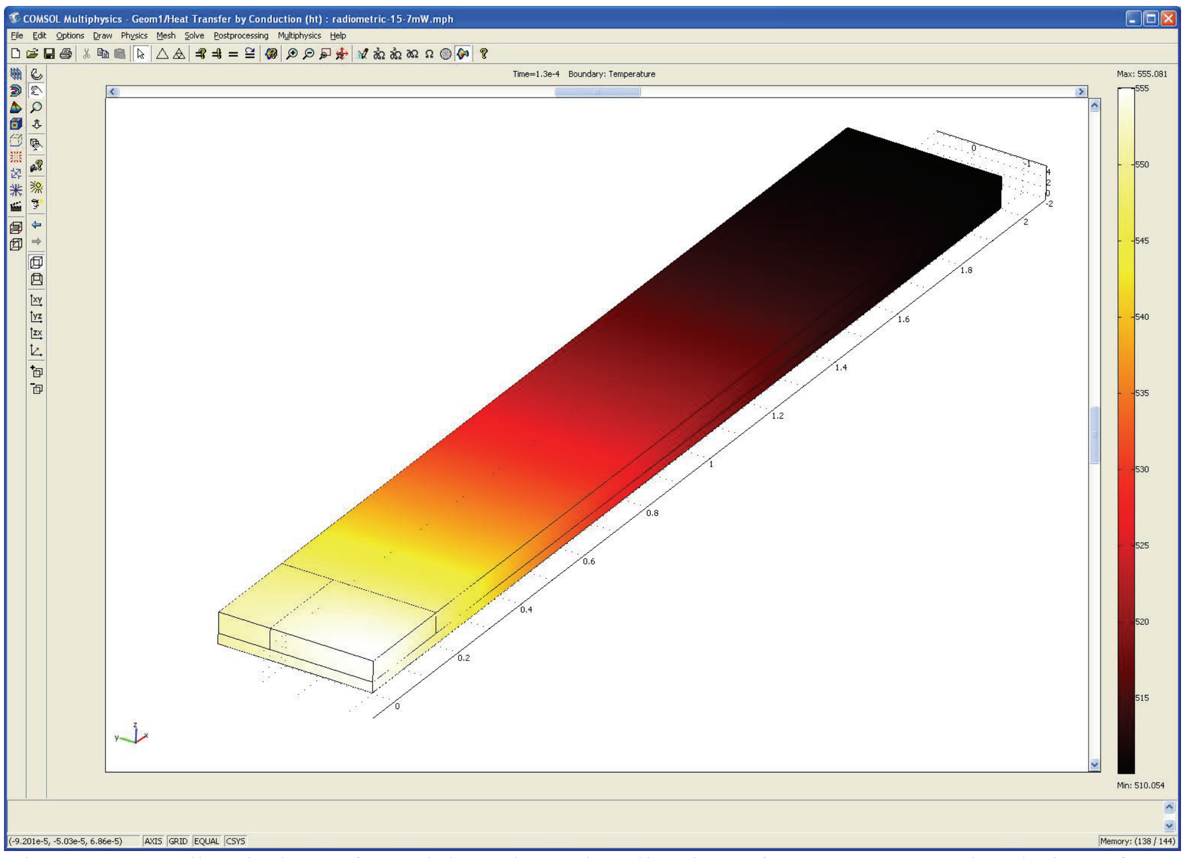

Figure 2.13 Edit window of Femlab 3.1i. A visualization of a temperature simulation after calculations based on the initial conditions is shown in the window. Initial and boundary conditions are explained in section 2.6.2.

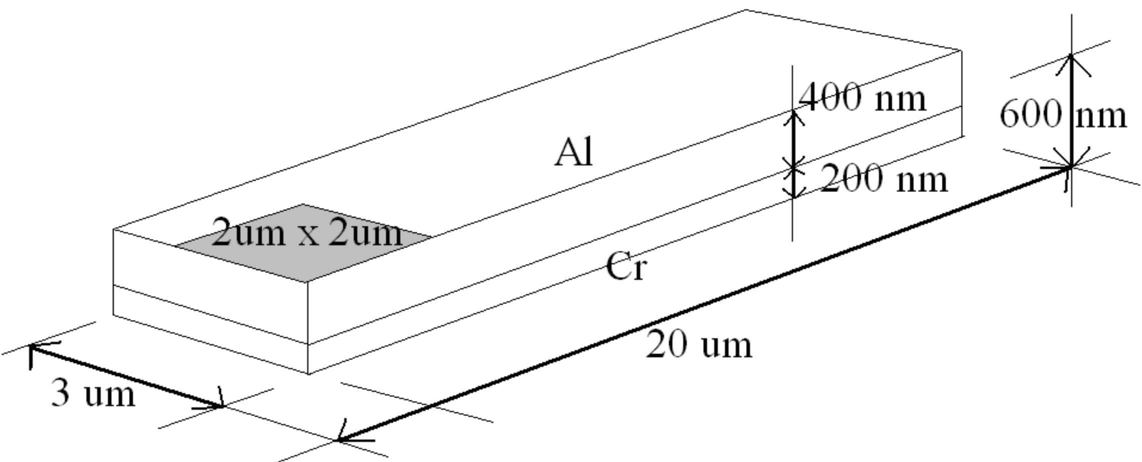

Figure 2.14 Model geometry for the simulation. The shaded area assumed to have an illumination.

2.6.2 Simulation Parameters and Boundary Conditions

The properties of the materials are the Young's moduli, 70GPa, 279GPa for Al and Cr (in the same order here after), the thermal expansion coefficients, 23×10^{-6}/K, 4.9×10^{-6}/K, the heat capacities, 900J/kg·K, 23.3J/kg·K, and the thermal conductivities, 160J/m·K, 23.3J/m·K, the Poisson's ratios, 0.33, 0.21. The power of the laser was assumed to be 10mW and the energy was assumed to be uniformly distributed onto the illumination area, 2µm×2µm. For a better peeling after evaporation in the etching step, a 5nm Au film was plated on top of the Al layer. Thus Au, not Al, determines the property of light energy absorption. The calculated absorptivity for the 5nm of Au is 0.08 (see Appendix C for calculation.) [110, 111]. The initial condition is that the metal box is at room temperature, T_{amb}. The boundary condition is based on the energy balance over a unit surface area in unit time. A normal conductive heat flux, $\hat{n}\cdot(k\nabla T)$, in the unit of power per unit area, is equal to

the sum of energy flow from a laser illumination, q, air convection, $h(T_{\inf} - T)$ and black body radiation, $C(T_{amb}^4 - T^4)$. Then the condition is [112],

$$\hat{n} \cdot (k\nabla T) = q + h(T_{\inf} - T) + C(T^4{}_{amb} - T^4) \quad (2.1)$$

where k is the thermal conductivity of the material (either Al or Cr), q is the energy input (only at illumination area, otherwise 0), h is the convective heat transfer coefficient, T_{inf} and T_{amb} are the temperatures at infinity and ambient temperature of the air, which are set to 293K, and C is the material dependent thermal radiation coefficient. Determination of h and C are in Appendix D.

$$h = 3.8\times10^4 (0.68 + 0.0012\times(T - 293)^{1/4}) W/m^2K \text{ (for all surfaces)} \quad (2.2)$$

$$C_{Al} = 1.9\times10^{-9} W/m^2 \cdot K^4 \text{ and } C_{Cr} = 1.6\times10^{-7} W/m^2 \cdot K^4 \quad (2.3)$$

When a simulation is over, not only the overall temperature, but also a temperature gradient inside any cross sectional slice was obtained. The gradient is important because any thrust is generated by the gradient. In section 2.6.4, the theoretical calculation of the thrust based on the object temperature gradient will be presented.

2.6.3 Evaluation of the Simulation Results

As a simple test for the precision of the simulation, simulated temperatures with known powers were compared with actual melting test. In Table 2.5 temperatures at the center of the illumination (center of the shaded square in Figure 2.14) were calculated based on the steps of laser powers. The size of an actual device was close to the dimension of simulation, 20μm long. At 16.0mW, the temperature in the air reached the melting temperature of aluminum, and this was verified to be true at the melting test in the air.

Power (mW, Error ±0.4mW)	Simulated Temperature elevation at the center of the laser spot (K)	Melting
4.0	561	N
6.0	638	N
10.0	890	N
16.0	970	Y
20.0	1088	Y

Table 2.5 Simulated temperature elevations at the center of the laser spot. The laser mode is set to continuous mode in air. A same type of device shown in Figure 2.14a was used for melt test.

2.6.4 Estimation of Thrust based on Simulated Temperature Gradient

In this section, I will discuss the calculation for conversion from a temperature gradient to a radiometric pressure. The assumed object is the same as given in Figure 2.14 in the air. At the heated surface the gas molecules are rebounding and gaining additional energies and momentum. Since a device has a temperature gradient from one surface boundary to another, there will be a net momentum transfer. When a gas molecule hits a surface, which has a temperature elevation ΔT above the ambient temperature, the molecule's energies before and after the collision will be,

$$E_f = \frac{3k}{2}(T_{amb} + \Delta T + \delta T), E_i = \frac{3k}{2}T_{amb} \quad (2.4)$$

where k is the Boltzmann constant, T_{amb} is the room temperature of air, ΔT is the temperature elevation of the heated surface and δT is the temperature gradient across the facing boundaries. A momentum transfer by an air molecule collision is

$$\Delta p = p_f - p_i = m(v_f - v_i)\cos\theta = \sqrt{3km}((T_{amb} + \Delta T + \delta T)^{\frac{1}{2}} - T_{amb}^{\frac{1}{2}})\cos\theta \quad (2.5)$$

where m is the mass of the gas molecule, v's are the velocities before and after collision and θ is the collision angle against the normal direction of a surface. The net momentum transfer to the heated body is obtained from the difference between this quantity and the momentum transfer from other side (without δT). Then the net momentum transfer is

$$\Delta p_{net} = \sqrt{3km}((T_{amb} + \Delta T + \delta T)^{\frac{1}{2}} - (T_{amb} + \Delta T)^{\frac{1}{2}})\cos\theta \quad (2.6)$$

Using the fact that δT is much smaller than T_{amb} and ΔT (in the simulation results, δT is less than 10K, but T_{air} and ΔT have order of 100K), I obtain,

$$\Delta P_{net} = \sqrt{\frac{3km}{T_{amb} + \Delta T}} \frac{\delta T}{2} \cos\theta \quad (2.7)$$

The net force exerted by a molecule of a species of the gas is

$$F_{net} = \frac{\Delta p_{net}}{\Delta t} = \frac{\delta T}{2\Delta t} \sqrt{\frac{3mk}{T_{amb} + \Delta T}} \cos\theta \quad (2.8)$$

The total net force depends on the mass of a molecule of a species and its partial pressure in air, a temperature gradient, total area of the heated surface and numbers of collisions in a unit time. The mass of N_2 and O_2 gas molecules are 14.0g/mol and 16.0g/mol each. In a cubic meter of the air, there are 32mol of N_2 gas and 8.6mol of O_2 gas. If the area concerned is designated as A, the total number of colliding molecules is equal to the number of gas molecules in a volume, the area multiplied by average velocity of the air molecules in the normal direction to that area at the room temperature (~280m/sec). Then the total net force will be

$$F_{total,net} = \frac{\delta T \sqrt{3k}}{4\sqrt{T_{amb} + \Delta T}} (\rho_{N_2} \sqrt{m_{N_2}} + \rho_{O_2} \sqrt{m_{O_2}}) A\bar{v} \quad (2.9)$$

where the Boltzmann number, k, $1.38\times10^{-23}m^2kg/s^2K$, $\rho_{N2}=1.96\times10^{25}m^{-3}$, $\rho_{O2}=5.3\times10^{24}/m^{-3}$, $m_{N2}=2.3\times10^{-26}kg$, $m_{O2}=2.6\times10^{-26}kg$, $\bar{v}$ =280m/s and A is the area. Putting all the numbers to the above equation, the thrust can be obtained.

According to the direction of the temperature gradient, there are two radiometric forces (Figure 2.15b), and direction for each radiometric force follows the direction for each temperature gradient. Then the radiometric force in z direction, F_z will be

$$F_z = \frac{\sqrt{3k}}{4}(\rho_{N_2}\sqrt{m_{N_2}} + \rho_{O_2}\sqrt{m_{O_2}})\bar{v}\int \frac{\delta T_{betweenB1andB2}}{\sqrt{T_{amb} + \Delta T}} dB_1 \quad (2.10)$$

For the simplicity of the calculation, it can be converted to,

$$F_z = \frac{\sqrt{3k}}{4\sqrt{T_{amb} + \Delta T}}(\rho_{N_2}\sqrt{m_{N_2}} + \rho_{O_2}\sqrt{m_{O_2}})\bar{v}(\int TdB_2 - \int TdB_1) \quad (2.11)$$

where $T_{amb} + \Delta T$ can be an averaged temperature in the numerical simulations.

Likewise, F_y can be obtained. Finally, a thrust parallel to the substrate, $F_{Lateral}$, can be calculated from those forces by an angular consideration. Typical slant angles of the cross section of a device were between 15° ~ 20°. θ = 17° is chosen.

$$F_{Lateral} = F_y \cos\theta + F_z \sin\theta \quad (2.12)$$

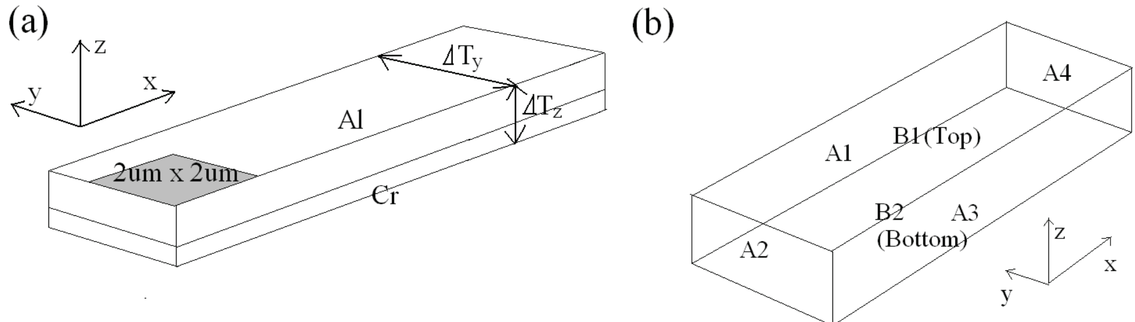

Figure 2.15 Geometry for radiometric force calculation. (a) Two temperature gradients simulated in the Femlab. (b) The Designations on the surfaces. The top surface, which includes the illumination area in (a) corresponds to B1 in the Figure (b).

2.6.5 Estimation of the Thrust and Friction

A device actuation was either on or off, depending on the laser power. From the thrust calculation in the previous section, I can understand this numerically. In the equation (2.11), a thrust depends on the temperature and temperature gradient;

$$F \propto \frac{\delta T}{\sqrt{T_{amb} + \Delta T}} \quad (2.13)$$

When the laser power is increased, a temperature elevation, ΔT increases. But the temperature gradient, δT increases more rapidly than ΔT, resulting in an increase in thrust as well.

When the threshold energy, 10.0mW was given as input to the simulation, the elevation of the temperature, ΔT was 590K, and the integration of the temperature, $(\int TdA_1 - \int TdA_3)$ was obtained numerically by the simulator. Using this information I get F_y = 350pN from equation (2.11). By the same method of calculation, I have F_z = 150pN. The combined thrust in (2.12) gave 350pN. The calculated thrust at the threshold power is equal to the friction per device. The magnitude of the friction well agrees the ranges of other published results obtained from LFM studies on the graphite [31, 32, 113, 114].

2.6.6 Thrust Dependence on the Device Size

The possibility of actuation of a device also depends strongly on the overall size of a device. In many actuation trials, there were fewer actuations if the size of a device became larger than 30μm, and if it was larger than 40μm, actuations rarely could be observed. Unlike observations, the estimated thrusts in the Table 2.6 tell us that thrusts remain constant over

the whole range of device sizes. When the length of the metal films becomes longer, the overall temperature of the device drops, but the surface areas are increased also. Those two factors neutralize any variation of a thrust. However, the model is too simple and it does not account for devices' curvature. When a device is curved, a generated thrust will be dispersed in various directions. The dispersion will be larger if the size of a device is larger. When a device is short (less than 20μm long in our experiments), it has less curvature, which will be more favorable to receive a radiometric thrust in a particular direction.

Length (μm)	Temperature at illumination area (K)	Calculated Lateral Thrust (pN, defined in eq. (2.12))
10	963	350
20	890	350
30	479	370
40	440	360
50	419	370

Table 2.6 Temperature and thrust dependence on the size of a device. A simple rectangular model in Figure 2.14 is used with a fixed laser power 10.0mW.

2.7 Demonstration of the Translation with the Radiometric Devices

The apparent visual distinction of the radiometric drive from the inertial drive is the shoving of the devices by the laser spot. A device body was found being pushed just like a finger pushing an object on a low friction surface. This movement involves a rotation pivot point, which was one of the contacting tips of a device. Since there are three tips supporting the device, one tip served as the pivot point, and the other tips slid if the laser spot was applied to a portion of the device close to one of the sliding tips. In the next step, the pivoting and sliding tips were switched. By the repetition of these two steps, device was driven across

HOPG for arbitrary distance in a predictable direction. Figure 2.16 shows this method via a schematic. The device has two large pads at the ends of two wings enhancing temperature gradients. Thus the laser spot was aimed at the pads.

In Figure 2.17, a series of SEM pictures show progressive steps of the staggered walking. At the beginning (a), the device resided beside a stationary particle on the surface. In (b) and (c) two consecutive applications of thrust are applied to the each pad. When a laser spot was near the right pad (in the direction of arrow in (b)) contact #2 acted as a pivot, and #1, #3 slid. When the laser spot was near the left pad, contact #3 acted as a pivot, and #1, #2 slid. After these two steps, a clear forward step could be achieved. More steps were taken to drive it further making it reach the point seen in (d). Finally a right turn was attempted at (e). After step (e) this device became stuck at this position.

Eventual sticking of devices onto the substrate was inevitable and devices were usually found to stop after fewer than 30 manipulations. I fabricated 17 identical devices and 3 of them could be translated. The other devices merely rotated around one tip or could not be translated at all. Even for a successfully translating device, if a contact tip meets a graphite edge, the device stopped because of increased friction. Except for this obvious reason, mostly I do not know the causes of stops. It is possible that because the temperature of a device was too high, metal contact tips were melted and annealed to the surface. The devices stopped even when the laser power was not above 16.5mW and heatsink pins are added to the bodies of devices. The resolution of the SEM was not high enough to detect the deformation of the contact tip visually after a device stopped.

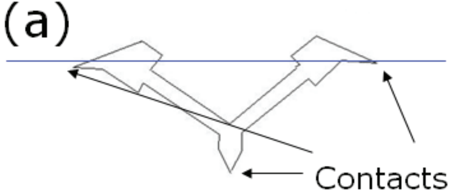

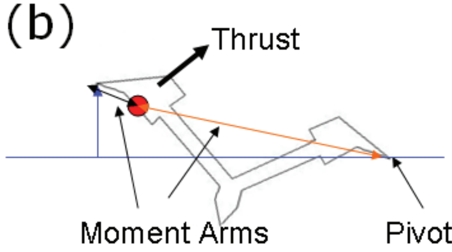

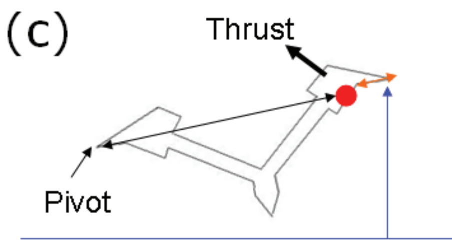

Figure 2.16 Schematics of the staggered walking based on the thrust movements.

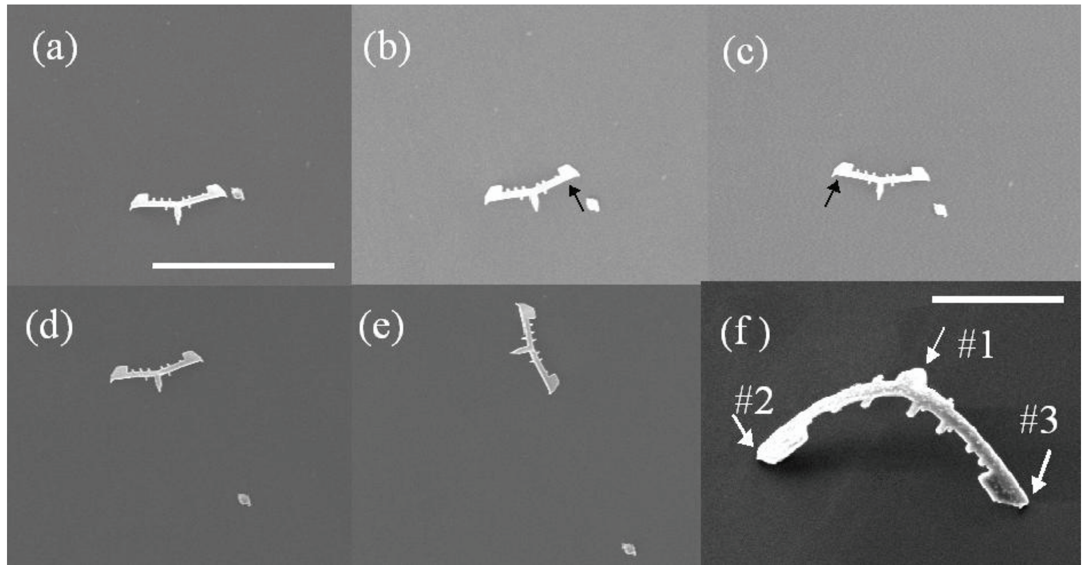

Figure 2.17 Staggered walking. From (a) to (e), a series of SEM pictures showing the walking steps. A dust particle beside the device acts as a stationary landmark. The scale bar is 60µm long. (f) An angled picture of the same device. The three contacts are displayed by numbers. The scale bar is 15µm long.

2.8 Summary

I presented evidence in this chapter that the radiometric effect can be used for propelling a locomotive device. Based on environmental tests, I proved that the radiometric effect was the main cause of thrust if a laser is used at continuous mode in air. A finite element study estimated the thrust and contact friction with a threshold measurement. A mode of staggered walking was suggested and the translational movements were achieved in a predictable manner. However, there remains a problem with the sticking of the devices onto the graphite substrates. Future studies of surface treatments or replacements of the fabricating materials should follow in an attempt to resolve this issue.

Chapter 3 Locomotive Devices Driven by Inertial Impact

In this chapter, I will discuss an inertial impact based device. I can divide the flow of discussions into three parts. In the sections 3.1~3.4 (Part 1), I will discuss the nature of forces, provide an introduction to a symmetric tripod device based on inertial drive, discuss driving conditions and the limits of friction, and describe an experimental setup. In sections 3.5~3.6 (Part 2), the dynamical properties of my devices will be examined. Deflections and thermal time constants will be the subject of those sections. From section 3.7 to the last section (Part 3), I will focus on a specific type of a symmetrical tripod thermal walking device. Because I want a device that can span a two dimensional surface, I chose a triangular device because its symmetry can be used to steer the device.

3.1 Previous Results on Thermal Actuators

As discussed in the chapter 1, the micro-actuator research has been active from the 1990s. In this section I will review publications specifically on thermal actuators and mobile devices.

The primary application of the thermal actuators is a conveyer system made from multiple bimorph beams or the groove joints. Many authors have proposed various types of

locomotive conveyer systems [70-72, 74, 115-117]. The actuator legs were fabricated by a planar fabrication processes and the legs were erected out of the plane by thermal actuation. Since the conveyer system needs lots of legs supporting and translating a load object, the bimorph legs are typically fabricated in an array. Other applications of the thermal actuators include switches [118], valves [78], cages for biomedical applications [119], catheters for medical applications [120, 121], and mirrors for display applications [63, 122].

Two publications are worth mentioning with regards to a mobile device. By simply turning a conveyer device upside down, it can be a walking device. Ebefor et al [51] demonstrated a device carrying a load (Figure 3.1).

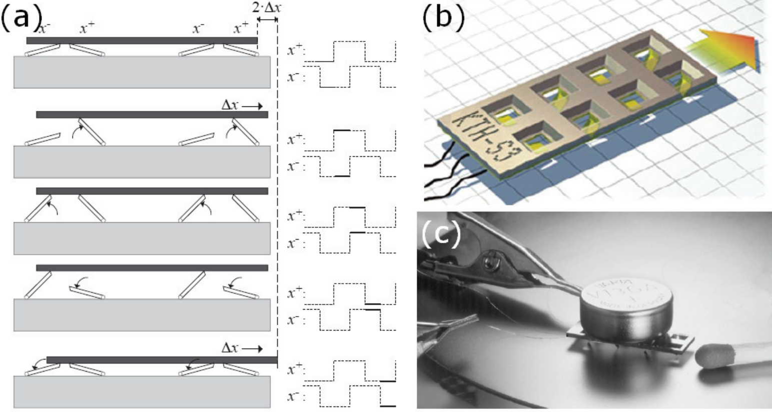

Figure 3.1 Thermal actuators. (a) A cartoon showing a conveyer system describing the gaits of 4 legs in time series (from top to bottom). (b) A model of the mobile device. It is the upside-down version of the conveyer system. (c) A picture of a mobile device with a load (a cylindrical battery). All figures and picture are from Ebefor et al [51].

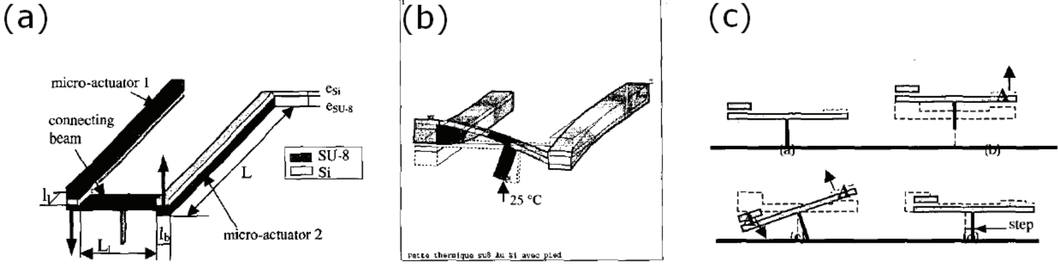

Figure 3.2 Twisting thermal leg. (a) A schematic of the proposed leg made of two bimorphs. L is 2mm long. The arrows indicate their direction of deflections when heated. A short beam

at the center will be tilted. (b) A snapshot of simulation. (c) The schematics of a step translation of the tip of the center beam. The beam is lifted, tilted, lowered and recovered its orientation generating a step in the right direction. Figures are from Wang et al [46].

The second publication worth noting is Bonvilain et al [123]. The authors suggested a twisting leg consisting of two bimorphs. Those bimorphs have a reverse order of bi-material plating from each other and their ends are joined with a center support beam (Figure 3.2). When the structure is heated, the support beam will be tilted. Figure 3.2c shows how a translation can be achieved. At first, the tip of the support is touching the substrate, and then it is raised, tilted by heating, lowered, and cooled to recover the orientation. The authors made 6 legs per, insect-like walking device. The gaits of the legs mimicked the walking of real insects; the legs are actuated three by three. Two groups of three in the extreme legs of one side and the central leg of the other side are actuated in turns. They successfully demonstrated walking and carrying a load.

From the review of actuators, I can understand the status of the developments of the thermal mobile device. Although there have been great progresses in the development of fabrication techniques, the fabrication of a mobile device in the range of micrometers (confined to walking type, but excluding a conveyer system) is still a major challenge due to the release of the structure after the 3-dimensional machining process. Up to the present, there has not a demonstration of an independent mobile device based on a thermal actuator with a size less than 1mm.

If I aim to fabricate a device that is truly in the micrometer regime and wish it to interact with micro/nano objects in microscopic environments, the main focus of my project is to reduce the size of the mobile device and to achieve two dimensional control of

directional motion on a substrate. My devices will also be independent, i.e. there is no tether to limit the motion. Energy will also be supplied wirelessly as well.

3.2 Introduction of a Symmetrical Tripod Thermal Walker Device

My devices have two metal films, Al and Cr, in a doubly layered structure. The shapes of the devices can be determined lithographically. Since any arbitrary standing object has at least three contacts on a surface, it is natural to make the devices having three radial spokes with pointed tips (Figure 3.3a). The lengths of the spokes are nominally identical and are from 5 to 25μm in 5μm step, and the widths are all 3μm. The thickness of each metal film was 5nm of Au, 400nm of Al, and 200nm of Cr. The choice of their thicknesses is based on the facts that, first, if the total thickness is too large, the bending will be too small to generate motions, and second, a better bending moment in a total given thickness of metal requires larger ratio of the Al/Cr (see eq. (2.1) below.).

The fabrication and release of three-dimensional objects are major problems in MEMS development. The internal stress of metal films can be used to surmount the problem. As explained in detail in section 2.2 of chapter 2, those metal films are thermally evaporated and the films can be released with an etching step. Because of the natural stresses of the films, the spokes curl up forming concave shapes. When a device is transferred onto HOPG, it stands in a convex posture with three sharp contact tips. The energy is supplied through a focused laser spot generating a temperature change so that a deformed device will experience a momentum. Among the three contacts, the contact with the least friction will slide towards

the junction of the spokes. Net progress will be produced when the momentum is large enough to overcome the contacts' frictions.

I presume that the cause of net motion is inertial impact, but the so-called inch-worm walk can be another explanation. This mode of walking is frequently used in catheter devices [120, 121]. Figure 3.3b shows the comparison of the two walking models. The inch-worm model assumes that a front contact or a rear contact sticks (or has relatively larger friction than the others) to the surface in turns. In the heating phase the front contact acts as an anchor while the rear contact slides forward. In the cooling phase the roles of the two contacts are switched. Thus after a thermal cycle a forward net motion is achieved. Meanwhile the inertial impact model assumes that all contacts slide forward in the heating phase, and that the rear contact slides backward in the cooling phase. Therefore the heating phase can be used to isolate the two models, where a net progress exists in the heating phase in the inertial impact model but not in the inch-worm model.

Let us estimate the magnitude of the kinetic energy generated by an inertial impact. The mass, m, of a device will be equal to the surface area multiplied by the thickness of two metal layers (ignoring Au layer). From the densities of aluminum and chromium, ρ_{Al}=2.7x10^{3}kg/m^3, ρ_{Cr}=7.2x10^{3}kg/m^3, the mass will be $3\times L\times(0.1\times L)\times(t_{Al}\rho_{Al}+t_{Cr}\rho_{Cr})$, where L is the length of a spoke, width is assumed to be 1/10 of the length, t_{Al}, and t_{Cr} are the thicknesses of each layer. The acceleration depends on how fast a device deforms with a deflection, D in a duration, Δt. The movement of the center of mass of the device is half of D. Thus a kinetic energy dissipated by stiction and dynamic friction will be,

$$Kinetic\ Energy=\frac{mD^2}{8\Delta t^2}=f_{dynamic}l+f_{stiction}d \quad (3.1)$$

where Δt is the thermal time constant, d is the diameter of the contacts and l is a step distance a device slides. The DMT model explained in chapter 1, estimates d ~ 4nm. The deflection, D and time constant, Δt can be obtained by analytical equations or by simulation studies. In the section 3.6, I will verify the calculations of deflection and time constant with measurements. Then in the section 3.9, with the kinetic energy based on the deflection and the time constants, I will evaluate equation (3.1) with slide step measurements.

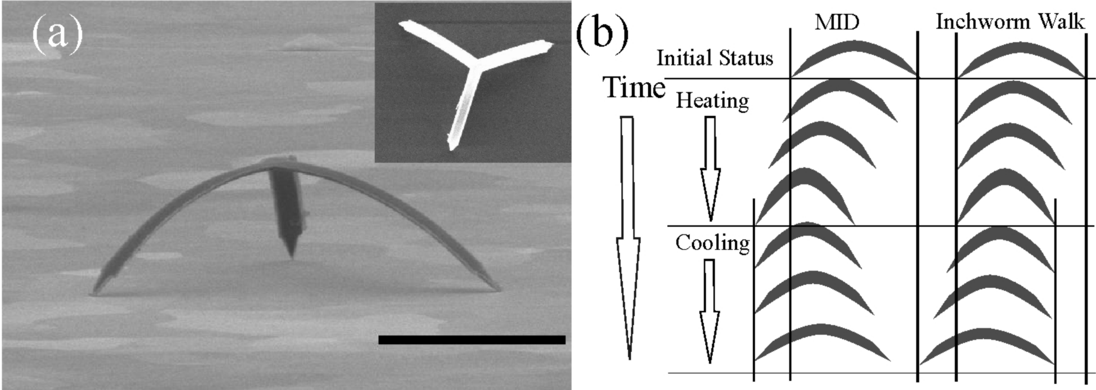

Figure 3.3 Symmetric tripod device and walking modes. (a) An angled SEM picture of a device standing on an HOPG sheet. The scale bar is 20micron long. (Inset: Top view) (b) Comparison cartoons of inertial impact walk and inch-worm walk.

The bimorph beam bending theory was initiated by Stoney [124] and developed later by Timoshenko [125]. Rigorous theoretical consideration of the bending is not a simple problem and calculations of continuum mechanics are required. I will quote the results from Gehring et al [126] on double layer beam bending. Two materials consisting of a double layer are assumed to have isotropic and homogeneous mechanical properties. Due to a thermal stress difference between the two films, the bimorph has a thermal strain. One end of the cantilever is assumed fixed and the deflection (Δ) of the other end is calculated by equation (2.1) with a small deflection approximation [126].

$$\Delta = \frac{3L^2\zeta(t_a+t_b)}{t_a t_b} \times \left[\left(\frac{t_b}{t_a}\right)^2 \frac{Y_b}{Y_a} + 4\frac{t_b}{t_a} + 6 + 4\frac{t_a}{t_b} + \left(\frac{t_a}{t_b}\right)^2 \frac{Y_a}{Y_b} \right]^{-1} \quad (2.1)$$

where ζ is a strain, t's are thicknesses, Y's are modified Young's modulus, $Y = E/(1-\nu)$, E is Young's modulus and ν is Poisson's ratio of two films, a and b. To maximize a deflection, I need to choose two metals, which have a largest difference in the coefficient of thermal expansions (CTE). The highest CTE solid material at room temperature is Al, which has 23.1×10^{-6}/K. For a low CTE material that can be thermally evaporated, there are several choices such as Cr, Fe, Ni, Cu, Ag, and Au. Among them, Cr has the lowest CTE, 4.9×10^{-6}/K. The Young's moduli are 70GPa for Al, and 290GPa for Cr. The remaining parameters such as length and thicknesses are free to control. If the length is larger, then the deflection becomes also larger. If the ratio of the two thicknesses is kept constant, a smaller total thickness gives a larger deflection.

The force generated at the tip of the beam is also an interesting issue because the force generated by my device should be larger than friction. In the same study [126], the recovering force to make the bimorph straight with a same strain, ζ, is:

$$F = \frac{W\zeta}{L}\left(\frac{Y_a Y_b t_a t_b (t_a + t_b)}{Y_a t_a + Y_b t_b}\right) \quad (3.2)$$

where W is the width of the bimorph and the rest of the symbols have the same meanings as in (2.1).

Practical limits of fabrication need to be considered to limit the thickness and length of the device. To maximize both the deflection and the force, the length and thicknesses need to be large enough within the limit that the peeling process allows. I selected 50µm (the longest device built) in length, 3µm in width, 400nm of Al thickness and 200nm of Cr

thickness. From eq. (2.1) the deflection will be ~ 1μm if the temperature elevation is ~300K. When a thermal strain, $\zeta=(\alpha_{Al}-\alpha_{Cr})\times 300K$ is inserted into eq. (3.2), the magnitude of the force is in the range of micro-Newton, which is more than 100 times larger than graphite friction. So I can conclude that there is enough force to overcome the friction of the substrate if the dimensional parameters are not too far from the numbers just mentioned.

In summary of this section, I will list questions in terms of physical motivations as well as technical problems:

1. Is it possible to make a micro-object standing on a flat surface with three pointed tips? If so, what method will be used for the transfer onto a flat surface?
2. Is the kinetic energy of a device generated by inertial impact thrust enough to overcome expected frictions? If so, under what conditions?
3. The kinetic energy will depend on the size of a device. Given power of an energy source, what is the limit of the size?
4. I will use thermal bending of bimorph devices to generate thrusts. What are the deflection and time constants? Do the calculations based on bimorph bending theory and measurements agree?
5. Which model between inertial impact and inch-worm is closer to observations?
6. What parameters of the laser can control the kinetic energy of a device through the deflection and time constant?
7. Is steering possible? If so, how is it possible?

3.3 Power Delivery and Movement Detection

I will not repeat here the fabrication of devices because it is identical to the description provided in chapter 2. The optics setup for the primary laser is identical to the one in the chapter2 except that a secondary laser (L850P100, Thorlabs) with 780nm wave length and 30mW power is added. Its purpose is: (1) to record the amount of deflection of a leg of a device, (2) to prove a walking mechanism, and (3) to measure a walking step distance. The power of the laser is reduced to 2mW and focused into a 3±1μm spot by the same objective lens. The reflection of the secondary laser was filtered through a colored filter to a photo detector. Thus the amount of the reflection was a function of three factors; (1) temporal deformations of the devices, (2) location of the secondary laser spot on the back of the devices, and (3) net motions of the devices. A flip mirror is used for a background illumination when searching for a device on the HOPG is needed. When a specific device is found the flip mirror is flipped down so that the secondary laser reflection can pass without being blocked.

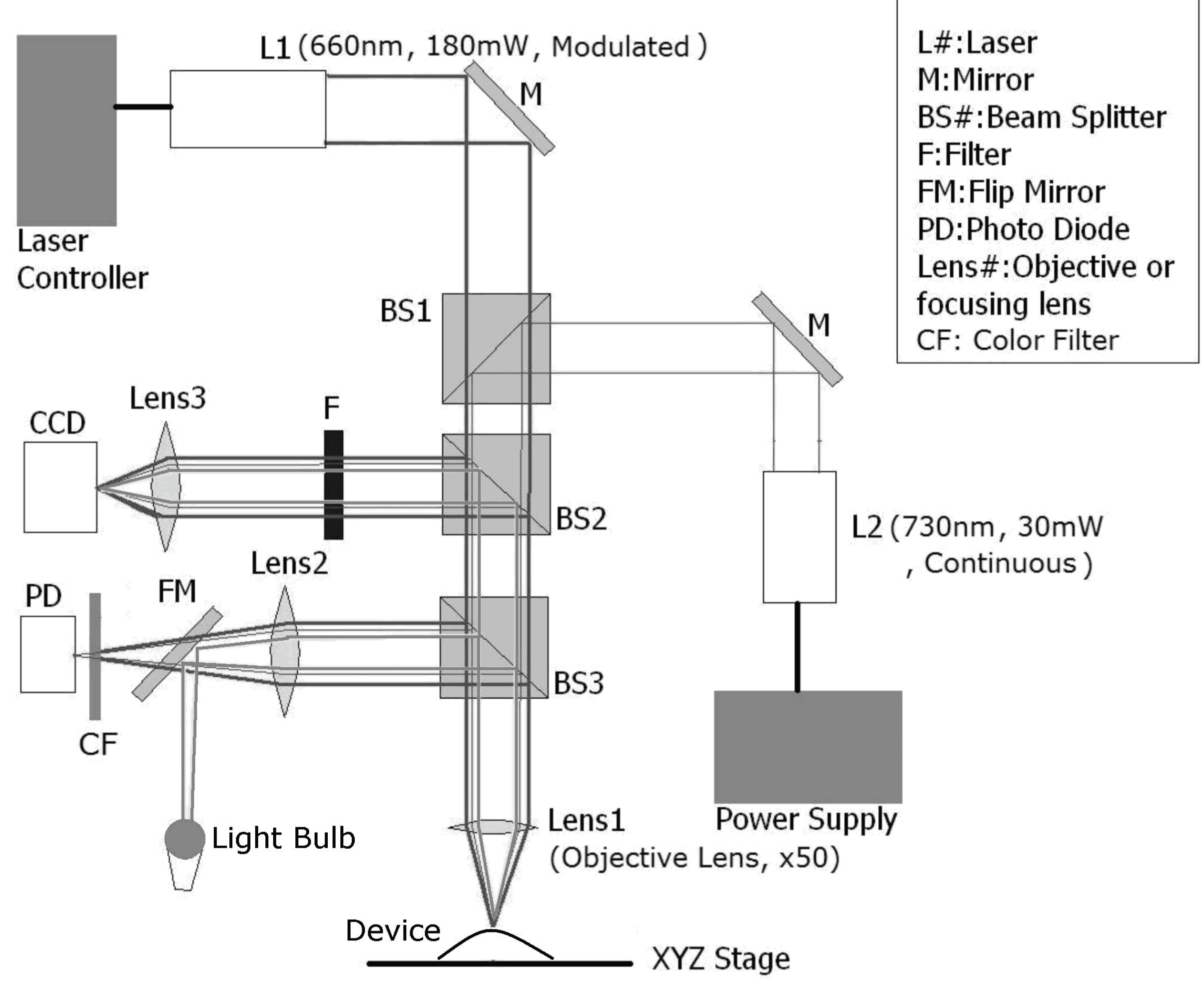

Figure 3.4 Optics diagram to actuate and monitor the motions.

Item	Catalog	Company
Laser 2 (L2), 730nm, 30mW	L850P100	Thorlabs
Laser 2 Diode Mount	TCLDM9, 5.6mm/9mm Laser diode mount	Thorlabs
Laser 2 Controller	LDC220	Thorlabs
Colored Filter (CF)	RG715	Schott
Photo Detector (PD)	DET2-S, High speed silicon detector	Thorlabs

Table 3.1 Extended parts list from Table 2.2

3.4 Proof of the Existence of the Thermal Modulation Thrust

In chapter 2, a thrust caused by the radiometric effect was proved. In this section isolation of another thrust mechanism based on inertial impact will be discussed. By the nature of the radiometric thrust, it needs a minimum level of laser power in CW mode. Below this limit there will still be a contribution from the radiometric effect, but the magnitude of the radiometric force alone will not be enough to overcome the graphite friction. I can therefore choose an under-threshold value as a laser power, and do the actuation tests under four conditions listed in Table 3.2. Then the expected results will then be like those in Table 3.2.

	Continuous	Modulation
Air	No	Yes
Vacuum	No	Yes

Table 3.2 Expected results of the actuation test if an under-threshold laser power is used.

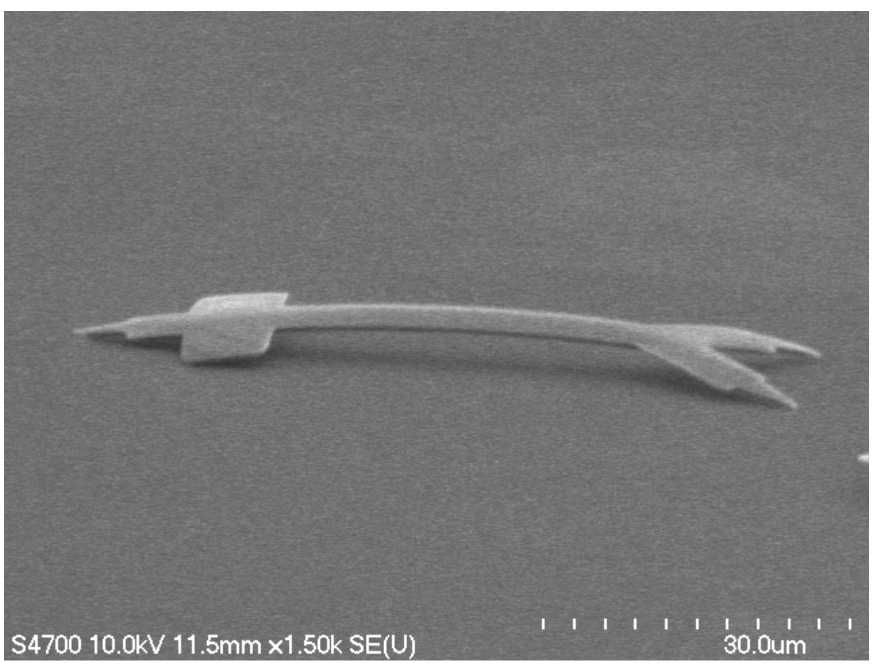

Figure 3.5 A device used for the actuation test.

The device under the driving tests had an arrow shape with a pad near the head and overall length was about 50μm long. The pad was added to maximize the receiving area of

the energy from the laser. An SEM picture (Figure 3.5) shows such a device. First, a CW laser in the air was used on the device. Whenever the laser hits the device, the device contracted, but no translation was observed. One comment is that the actuation also depends on the overall size of a device. The one shown in Figure 3.5 did not move with a CW laser power, but another smaller device did move with the same laser power. This result is based on the radiometric effect I discussed in previous chapter 2. Thus I can remove the unwanted mode by controlling the size or by adjusting laser parameters.

With a CW mode in the vacuum, either instant melting of the devices or gradual melting without any motion was observed due to a heat energy accumulation. When a modulation mode was used, in both the air and vacuum environments, motion of the device was achieved. These results can be summarized in Table 3.3, which is identical to the expectation except for the matter of radiometric force interference.

	Continuous	Modulation
Air	No/Yes (depending on the size of a device and the laser power)	Yes.
Vacuum	No	Yes.

Table 3.3 Actuation test results in the four conditions.

Another proof of the inertial thrust is the actuation behaviors depending on the motion of center of mass of a device. Figure 3.6a is an SEM picture of a device used for the tests. If the device is extended flat and viewed from top, it has a laterally long trapezoid shape. Due to an intrinsic film stress it has a curvature and stands on tips at both end. The slope of the cross-section of the device is not parallel to the substrate and has a slant angle due to two extended tips at the extreme ends.

The standing angles as can be seen at Figure 3.6a could be controlled by the 'foot' angles, which were fabricated by the electron beam lithography process. If the inertial impact drive by modulation is true, the velocity of the movement of the trapezoid will be much faster than the rectangular one when the same laser power (below a threshold power) and driving frequency is used. The lateral shift of the mass per thermal cycle was checked for the trapezoid device under a 100 zoom objective lens, whereas little lateral movement was observed in the rectangular device. The driving movies with these two devices clearly demonstrate that a device with the slant angle moved faster (around 20±10μm/sec) than the other (up to a 3±1μm/sec). From the observation, I concluded that an inertial impact by modulations is the cause of motion with an under-threshold laser power.

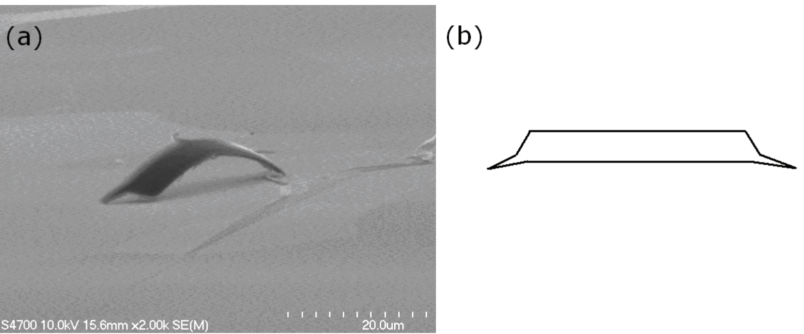

Figure 3.6 Band device. (a) An angled SEM picture of a trapezoid device standing on the HOPG. (b) A top view of the extended device. The length from one tip to the other tip at both ends is about 20μm.

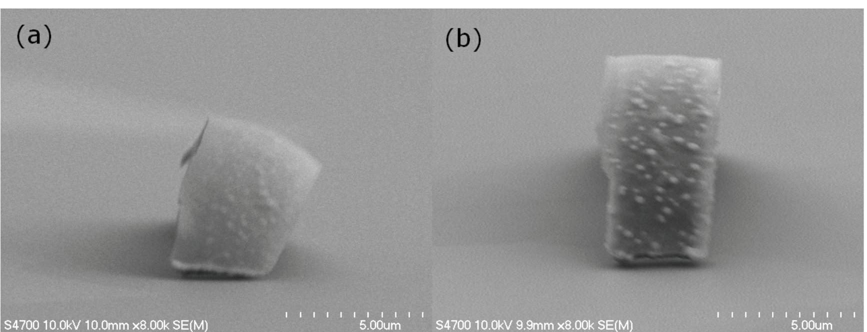

Figure 3.7 Angled SEM pictures of a trapezoid device and a rectangular device. (a) A device standing with a slant angle. (b) A device standing with an upright angle.

As mentioned above, the radiometric effect and inertial impact drive are mixed in air. To discriminate them, applications of continuous mode and modulation mode to the slanted band device give a clue to isolate one mechanism from the other. When the laser power was 8.6±0.4mW in CW mode, the device shows no motion at all, implying that the radiometric thrust is not enough to move it. Next, the driving is switched to the modulation mode and now the device begins moving. When the laser power is increased to 10.0±0.4mW the radiometric thrust acts to move the device. This means that there is a threshold for the CW driving between 8.6mW and 10.0mW and below the threshold the inertial thrust is clearly isolated from the radiometric thrust. Not just unique to this device, this method of isolation is used for other devices in general. If a device could be driven in a continuous mode, the laser power was reduced until no motion was observed in CW mode, but motion was still observable in modulation mode. If the inertial impact thrust is true, the velocity of the movement can be controlled by adjusting laser parameters. Control of the velocity of a device via laser parameters will be discussed in sections 3.9.

3.5 Dynamic Properties of the Devices in Terms of the Thin Film Mechanics

3.5.1 Deflection based on Temperature Variation

The devices constructed here are basically thin metal films and they follow the continuum mechanics equations. In this section I want to compare numerical measurements of the film deflections with analytical predictions from equation (2.1). Predictions on the deflections are done in two steps. First, I need to calculate equilibrium temperature based on a laser power. Second, I will calculate deflection at the temperature.

For the estimations of equilibrium temperature and natural relaxation time, I can solve a simple analytical model assuming a metal bar in air. I can set up an energy balance equation with energy input and outputs such as the laser power, thermal conduction, free convection and thermal radiation. For simplicity of the calculation, let the thermal conductivity, k, density, ρ, and heat capacitance, c_p, be weighted averages of Al and Cr according to their thickness ratio. For optical properties such as light energy absorptivity, α, and radiation emissivity, ε, I will use that of Au because the Al film is covered by Au. The temperature is a function of location inside the metal box, x and time, t. The change of heat energy at a location, x, in a unit time is equal to the sum of heat conduction from neighboring locations (first term on the right hand side of eq. (3.3)), energy input from the laser spot (second term), heat dissipation processes of black body radiation (third term) and air convection (final term). Because I can think of the metal box as a one-dimensional object, surface area per unit length along the box needs to be incorporated in geometrical terms like width, W, and height, H of the box. Thus the equation of energy balance is [112],

$$\rho c_p \frac{\partial T}{\partial t} = \left(\frac{\partial^2 T}{\partial x^2} + \frac{\partial k}{\partial x}\frac{\partial T}{\partial x} \right) + \frac{\alpha \dot{q}}{2LWH} - \frac{2(W+H)\varepsilon\sigma}{WH}(T^4 - T_\infty^4) - \frac{2(W+H)h}{HW}(T - T_\infty) \quad (3.3)$$

with initial conditions, $T|_{x=L} = 293K$, $\left.\frac{\partial T}{\partial x}\right|_{x=0} = 0$, and $T|_{t=0} = 293K$. The first condition means that the far end touching the substrate (x=L) is held at room temperature. The second one means that there is no temperature gradient at the middle of the box (where the laser spot is located.), because a temperature symmetry is assumed. And third one means that the initial temperature of the laser spot (x=0) is at room temperature. Here $\dot{q}$ is the power of the laser, σ is the Stephan-Boltzmann Constant, and h is the free thermal convective constant. Determinations of α and h are given in Appendix C and D. In the range of a laser power from

0 to 7mW, eq. (3.3) can be solved to produce a series of increasing temperatures. When I put these results into equation (2.1), I get the relationship between laser power and deflection like the graph in Figure 3.8 (straight line).

The device used for the deflection measurement was a happenstance device lying on its side (Figure 3.9a). When it was viewed from the top, the bending was observed clearly with the optical microscope. A laser spot with known power was aimed at one portion of the device and the curvature was modulated with a low frequency (1Hz) so that the CCD camera can capture frames when the device was curled and stretched. After the video was digitized, two frames when the laser was on and off were overlapped to compare the locations of the tip. The tip deflection was measured directly from the overlap image (Figure 3.9b). The results (dots) in the Figure 3.8 clearly show that the amount of deflection depends on the laser power. The values adhere well to the predictions within the error range and the flat region below 1mW is attributed to the resolution of the video.

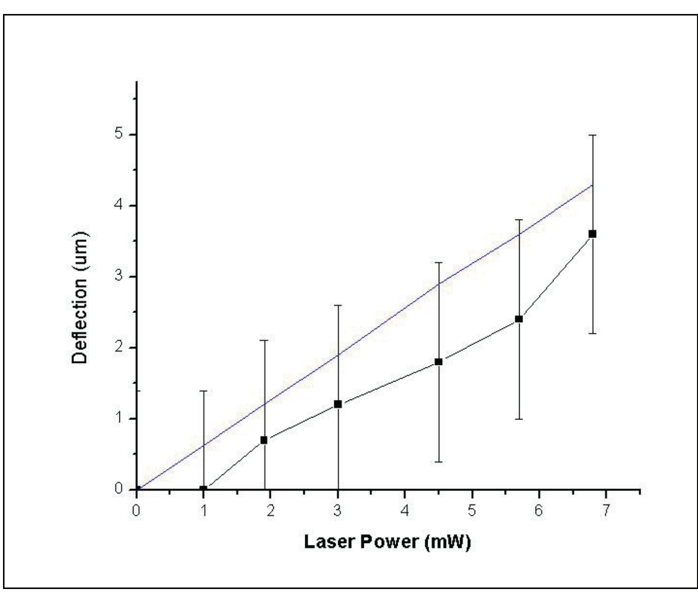

Figure 3.8 Deflection dependence on the laser power

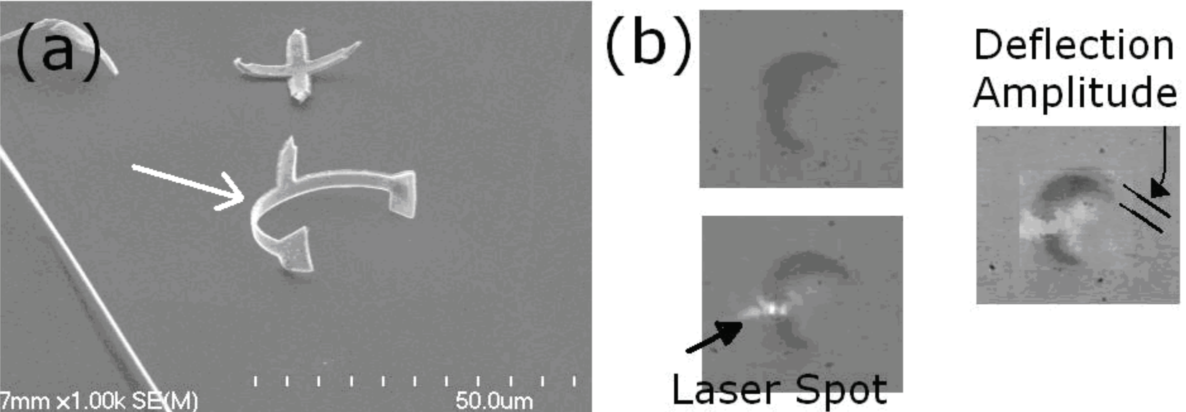

Figure 3.9 Measurements of deflections. (a) The device used for the deflection measurement (white arrow). (b) Top frames under the optical microscope when the laser was on (top) and off (bottom). The two frames are overlapped and the defection amount was measured in the digital image directly. The images were taken at the laser power, 6.8mW.

3.5.2 Time Constants of Heating and Cooling of a Device

Another interesting dynamical property of a device is the natural relaxation time, because it defines the maximum bandwidth of device performance. According to previous publications [52, 78, 84], the maximum frequency of the thermal actuation operation is in the range of kHz. I expect that my devices will have similar bandwidth. First I calculate a driving frequency by analytical calculation and simulation. When the equation (3.3) is solved, it gives the time constant (1/e of saturated temperature) of 100μs up to 10mW of the laser power. For simulation studies, I once again used Femlab. Because I wanted my simulation to represent experimental conditions closely, my model resembles an actual device (Figure 3.10a). The device is a pinwheel type, having four 7μm long legs. By thermal modulation it rotated clock-wise. The primary laser was aligned at the center junction of the device and same position was used for the simulation.

When a device has a higher equilibrium temperature than the ambient room temperature, the loss of heat energy will be proportional to the temperature deviation. Thus

the temperature profile during a heating (or cooling) phase will appear as an exponential rise (or decay).

Simulated temperature profiles for the heating and cooling processes are shown in Figure 3.10c. When the power was assumed to be 5.3mW, the calculated time constant was about 50μs and the full duration of the heating/cooling process was about 200μs. For comparison, temporal profiles of the reflections were measured in different laser powers (Figure 3.11). The probe laser, L2, was set at a midpoint along a leg. When the device was heated, the legs are curled reducing the amount of reflection. When the laser was turned off, the legs started to cool returning back to room temperature curvature increasing the reflection. Reflection decay data were fit to an exponential decay curve producing a time constant of 40±10μs, which is in good agreement with the simulations. Thus I conclude that a maximum bandwidth of contraction and relaxation can be up to 10kHz, albeit the actual maximum bandwidth of an individual device will also depend on the size of a device. A device can be driven at an arbitrarily low frequency. Thus the range of frequency for driving a device will be from 1 to 10kHz. One caution is that the pulse ramp should be kept smaller than the natural time constant not to lose the inertial impact.

The vibration bandwidth can define the speed of a contact's sliding speed. If I compare the contact slide speed with an observed device speed, I can know the behavior of the tips; whether every step of progress is identical to the deflection. It is an interesting question to ask what portion of a deflection is converted to actual device progress.

For the calculation of the slide speed, I need a reflection profile along an axis of a specific leg. A secondary laser spot in continuous mode was aimed at a leg and the amplitudes of reflections along the leg were scanned. To obtain the relationship between the

reflection angle and the laser amplitude along a leg, tangent angles along a leg were extracted from an SEM picture (Figure 3.10a) using the tube tracing software (see A.3 in appendix A for detailed explanation on the function of the software.) [127]. Then from the relationship between the angle and reflection magnitude, I can calculate a tip's slide speed from a temporal reflection variations in Figure 3.11. The graph in the Figure 3.12 indicates that the velocity of the tip sliding over the graphite becomes larger when the laser power is increased. This behavior is expected behavior because if the primary laser power becomes larger, deflection will be correspondingly larger at a given time scale due to higher equilibrium temperature. When the laser is turned off, the rate of heat energy loss will be correspondingly faster due to a larger temperature difference from the ambient temperature.

As a cross-check, multiplication of the tip sliding speed and the time constant will give a deflection. This can be compared with the calculated deflection (2.1). From the numbers in the Figure 3.12, the velocity of sliding tip at 5.3mW multiplied with time constant gives 1.6±0.6μm. Equation (2.1) gives 1.5μm with 15μm long device at the same power. Thus the two numbers agree each other.

With this information I can construct a picture of the behavior of the thermal walking devices. Although the device shown in 3.10a is a rotating one, it has a similar magnitude of deflection per thermal cycle just as any other thermal walking device would. Even though the magnitude of the deflection can be multiple micrometers, this does not mean that one step per thermal cycle really produces micrometers. As will be presented in the section 3.10, the observed velocities are in the order of hundreds of micrometers per second at best with a 1kHz driving frequency. This gives hundreds of nanometers per slide, which are 10 times

smaller than the estimated deflection. I conclude that the contact tips are mostly slipping rather than clutching the surface.

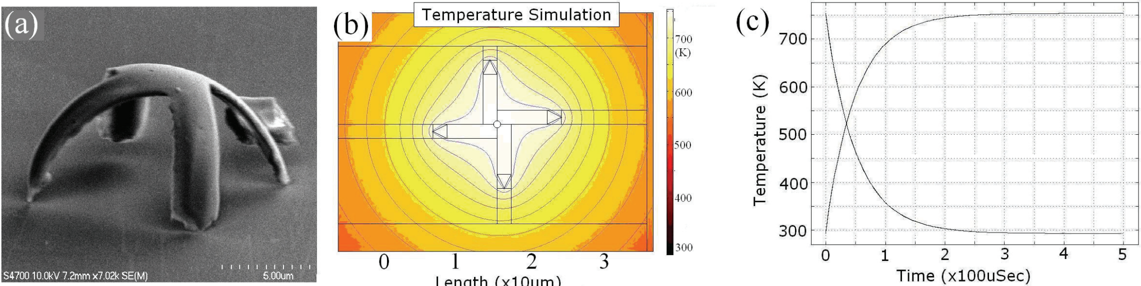

Figure 3.10 Simulation of a time constant. (a) An SEM picture of a pinwheel device. (b) A snap frame of a time simulation of the temperature distribution. The center circle is assumed to have the laser illumination. (c) The temperature profiles (one for laser on and the other for laser off.) along the time at the junction of the device when the laser power was assumed to be 5.3mW.

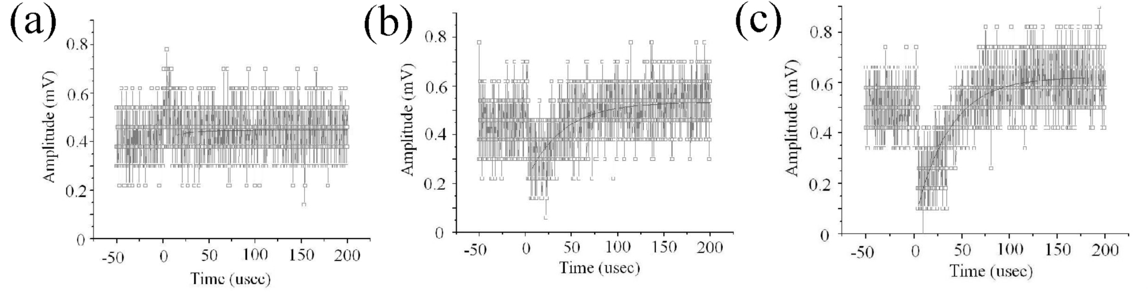

Figure 3.11 Reflection amplitude measurements with different laser power. The 0 second is the time when the primary laser was off and the device started to cool. From the left graph, the powers are 1.2±1.0mW, 4.4±1.0mW, and 5.3±1.0mW.

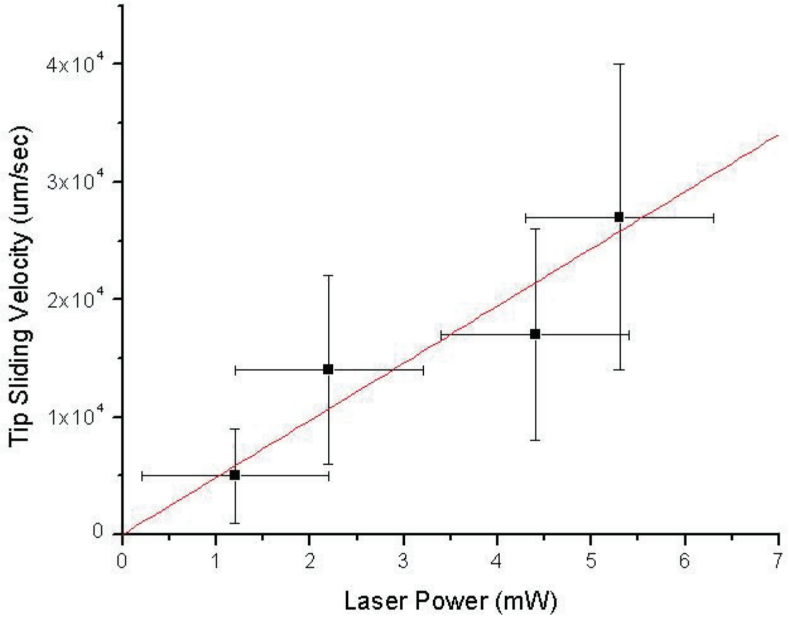

Figure 3.12 Velocity of the tip sliding depending on the laser power.

3.6 The Control of the Contraction by the Laser Power and the Pulse Width for Symmetric Tripod Device

In this section I will discuss deflection and time constants of a special type of device, symmetric tripod device, because this type of device is important for free-style movements on a flat surface. Information about the deformations will be helpful in determining the influences of friction and the overall net motion in section 3.10.

The temperature of a device is determined by the power of the primary laser and three heat dissipation processes; conduction, convection, and radiation. As seen in Figure 3.13, a geometry identical to a device was assumed and an area of $9\mu m^2$ laser illumination was assumed at the end of a spoke. The simulation method is identical to section 2.6.2, so it will not be repeated here. The equilibrium temperature can be converted to a deflection of the device. Figure 3.14 displays time evolution of a mechanical deformation.

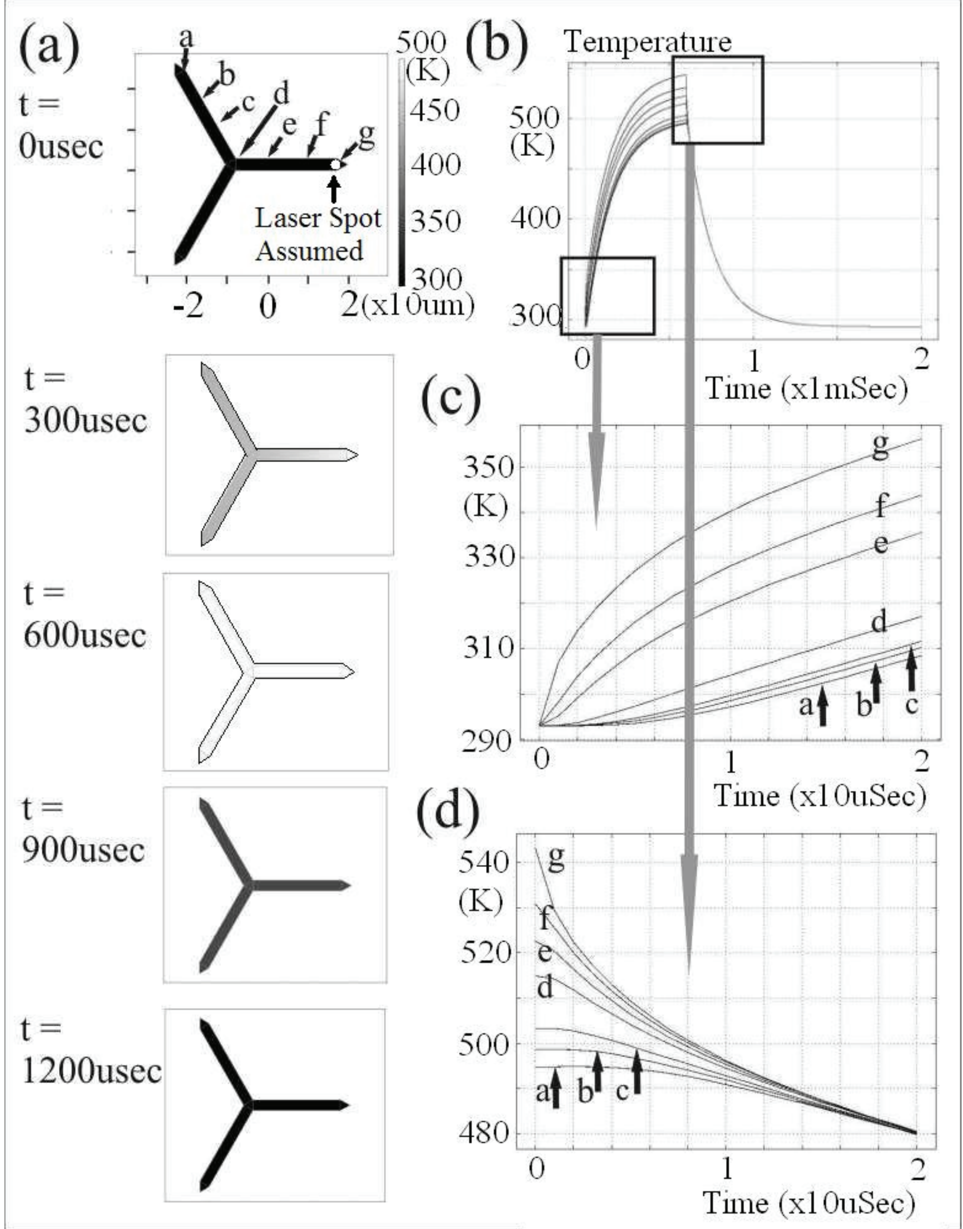

Figure 3.13 Finite element analysis results on the temperature evolution. (a) A model device with same dimensions. The laser power was assumed to be 18mW over 9μm^2 at the white circle (location g). The temperature is displayed in gray scale. The pulse width was assumed to be 600μsec. (b) Time evolutions of temperature at multiple locations, a to g. (c), (d) Enlarged graphs of the temperature evolution in initial 20μsec when the laser is assumed to be on at 0sec (c) and off at 600μsec (d). Note that different rates of temperature rise and fall indicate a delay of heat energy transfer between multiple locations.

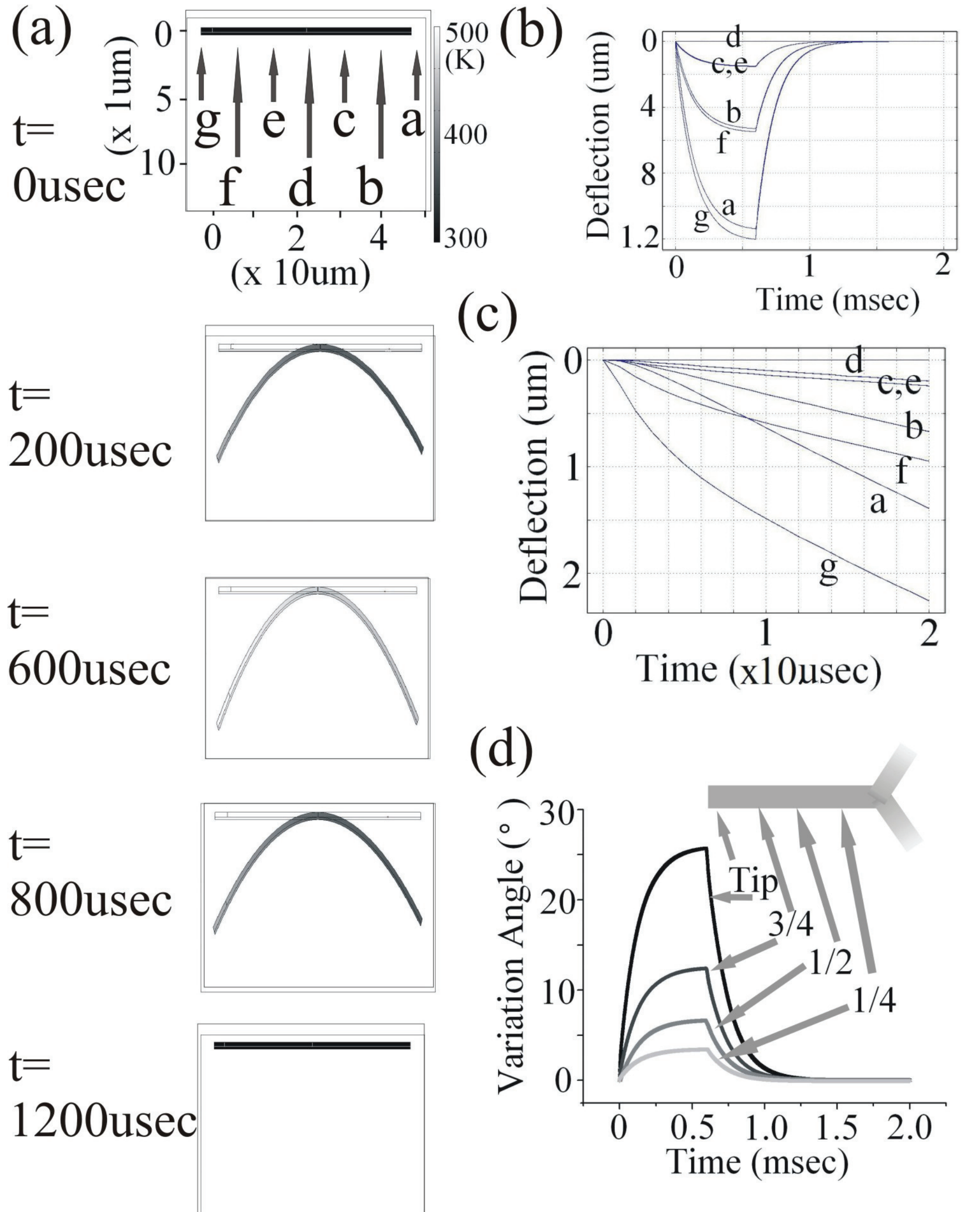

Figure 3.14 Time evolution of device deformation. (a) Initial state in a straight bar with no deflection. The locations, a to g, are identical to locations in Figure 3.13a. (b) Simulated deflection of each location. (c) Enlarged graph of the initial 20μsec. (d) Deflection is converted to variation of tangent angle at various locations along a spoke.

To check the agreement of the calculated deflection and measurements, I used the same reflection method explained in previous section, 3.5. The graph in Figure 3.15a displays reflection cycles in 3 steps of pulse widths with a fixed power, 10±2mW obtained

from an upside-down device (3.15b, inset). The recorded values are not the deflections directly but the reflections of the secondary laser at the middle location on a spoke. To convert a deflection to a reflection I performed following steps (they are basically same method already described in 3.5.2.). The reflection of the secondary laser depends on the relative angle toward the photo detector, so I measured reflections following an axis of a spoke (Figure 3.15b). Then I know the relationship between the reflection and the instantaneous angle of a specific location along the spoke. Next the bimorph deformation can be converted to a curvature assuming the device is a circular arc and the curvature can be converted to tangent angles at any specific locations along the spoke. Finally the temperature evolution could be converted to the evolution of the reflection. In every reflection measurement, I aimed the secondary laser spot at the same location, always at the middle of a spoke axis. Also in the calculations, I assumed the same location. Figure 3.15c shows that the simulated reflections are 2 times larger than actual values, but that the trend of increasing amplitudes by primary laser power and pulse width is correct. I concluded that the simulation results describe the temperature and deflection profiles with reasonable accuracy. This means that the degree of deformation can be controlled by the primary laser's parameters.

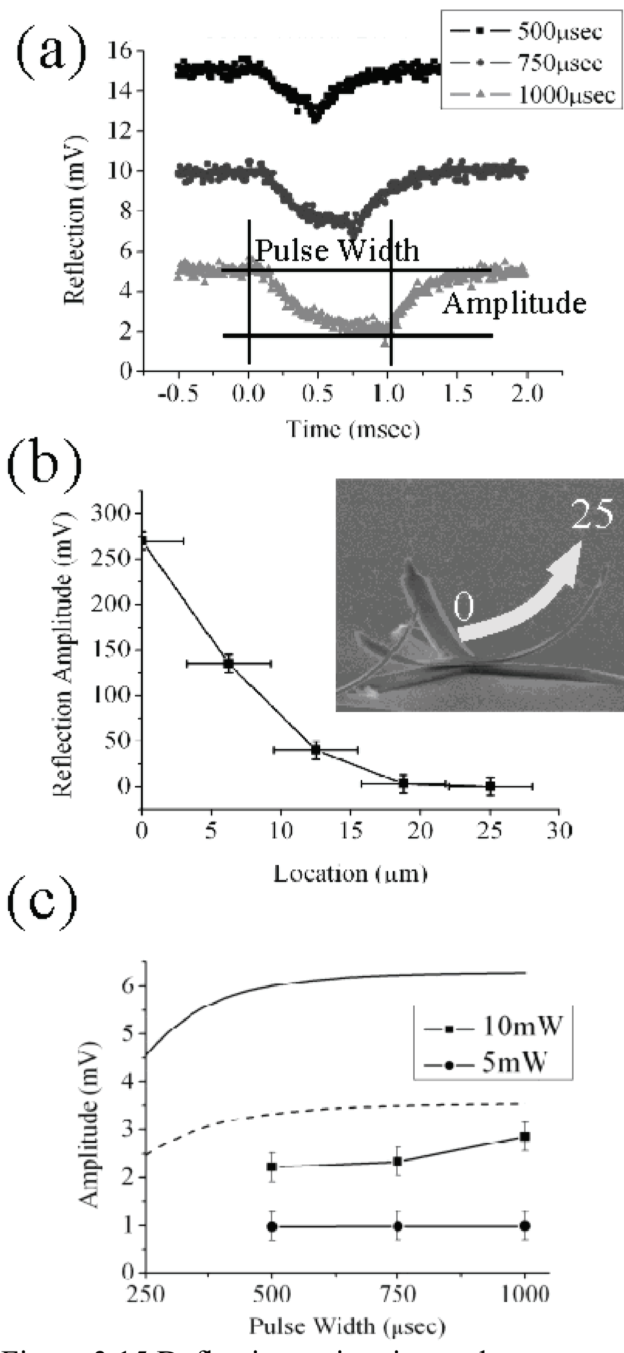

Figure 3.15 Deflection estimation and measurements by reflection. (a) Reflection waveforms recorded in three steps of pulse widths at 10mW laser power. Datasets obtained at 5mW is not shown. (b) Reflection profile measured along the axis of a spoke. (c) Simulated reflection curves (solid line at 10mW, dashed line at 5mW) compared with measured amplitudes.

3.7 Conclusions in section 3.5 and section 3.6

My devices are essentially thin metal films. The deflection of a device is based on a well known bimorph bending theory. The reflection measurements obtained using my devices indicate that the values of deflection agree well with my calculation. The thermal time constant can be calculated by an energy balance equation or simulation by finite element analysis. In summary, my devices are as small as 20μm, but still can be described in good agreement by continuum mechanics.

3.8 Proof on the Inertial Impact Drive

Another use of the reflection measurement is for isolating one of the walking models described in the Figure 3.3b. For this purpose, one cycle of reflection waveform from a device that experienced a net motion and the one from a device that did not experience a net motion, were recorded and compared. In the measurements, I used a 25μm-legged device that was capable of movement on an HOPG substrate. The top graph in the Figure 3.16a shows the recording of 5 cycles of reflection changes from a walking device. The laser parameters were 10±2mW of power, 500Hz driving frequency, and 600μs of the pulse width. As compared to the bottom graph, the bias after each cycle is reduced which can be interpreted as a net motion. The step distances were stochastic in magnitude. After some period of actuation and steering, two contacts of the device could be trapped intentionally at an edge of the graphite step. Usually, if a contact meets such a graphite step, the contact is held fixed due to increased friction, and no further motion could be achieved afterwards. Using this

setup, I can obtain standstill-walking waveforms (bottom graph, Figure 3.16a). Overlay of one cycle from each graph (A and B) is displayed in (c). The two walking models in Figure 3.3b suggest when a net motion arises. The inertial impact model assumes that the net motion is in the contraction phase, while the inchworm model assumes that this occurs in the relaxation phase. The waveforms will deform in each phase according to their own model (Figure 3.16b). As can be seen from a comparison of the two reflection datasets in Figure 3.16c, a deviation exists at the contraction phase. Thus I conclude that the inertial impact is the correct model.

I plotted several simulated curves assuming advances in the contraction phase and retreats in the unfolding phase over different distances. To remove inconsistencies of amplitudes, the curves were scaled down to fit the data. From the three curves in the contraction phase, a curve assuming an advance of 400nm matches well with the data. This is also true for the 200nm retreat curve for unfolding phase. I interpret this as the device advancing a net distance of 200nm. This is corroborated from the fact that, an interpolated secondary laser sweep for a 200nm is closer to 1mV (a value of 1±1mV), not 4mV by reflection measurement at the middle of a spoke of a non-vibrating device.

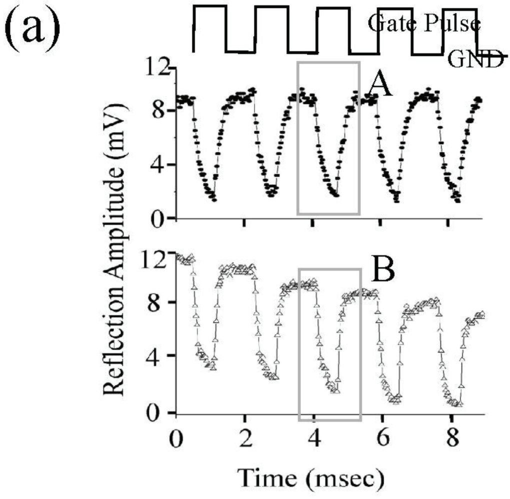

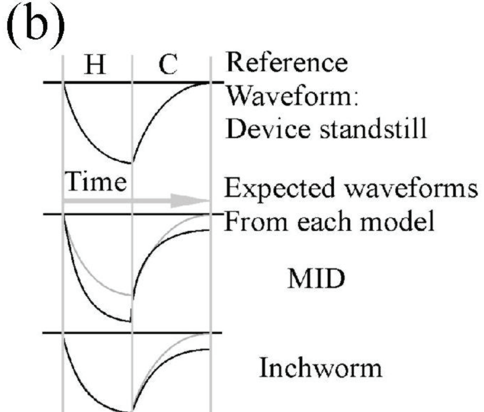

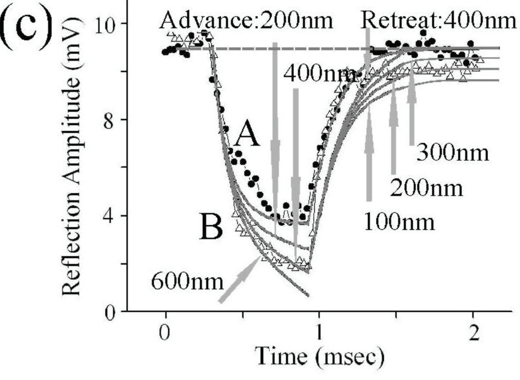

Figure 3.16 Proof of the inertial impact mechanism. (a) Waveforms recorded while a device was moving (top) and standing still with no net motion (bottom). The pulses coincided to trigger gate pulses from the pulse generator. (b) Inertial impact model has a deviation in heating phase(H), while the inchwork model has one in cooling phase(C). (c) Comparison of one cycles (A and B) in each waveform dataset. The difference in the heating phase can be seen clearly. The voltage difference corresponds to a 400nm advance. The bias difference at the end of cooling phase agrees to 200nm retreat curve. The curves are scaled down with assumed net movements being kept constant in various amounts.

3.9 Control of Velocity

3.9.1 Laser Power Dependence

The velocity can be controlled by the laser power. The other governing parameter is the size of a device. As I saw in chapter 2, if a device is smaller, the equilibrium temperature will be higher at the same laser power, but the deflections will also be smaller. Thus temperature and deflection will compete to determine the actual velocity.

In the velocity measurement experiments, three different sized devices were tested; 5µm, 15µm, and 25µm long legged devices. The power of the primary laser was varied from 0 to 18±2mW with a fixed frequency, 500Hz. The velocities were captured in video clips by a CCD camera in a top-down view. Each video clip was digitized and video spot tracker software [128] was used to track a specific feature of a device. Every device had a bright spot reflecting the background illumination light. It was stationary inside the device and it also did not change its shape while in the actuations. Thus this provided an easy feature for the software to track. Video spot tracker can generate a pixel based track record over equally timed frames. The distances in the pixel space were converted to an actual distances in the real world to provide an actual velocity. Finally a step distance was obtained by dividing the velocity by the driving frequency. The step plot is shown in the Figure 3.17a. The 5µm legged device did not show any movement up to the maximum laser power. At the laser power 16~20mW with the 5µm legged device, melting was observed as predicted by the FEA simulation study. In the case of 15µm and 25µm legged ones, the step sizes increased following the laser power. The degree of slide increase under laser power variation

determines dynamic friction. If the laser power is gradually reduced, there will be a cut-off power when a device stops actuation. Such critical power defines the stiction.

To estimate both frictions $f_{dynamic}$ and $f_{stiction}$, I use a simple mechanical model, which is already given at section 3.2. I quote the equation again here;

$$\frac{mD^2}{8\Delta t^2} = f_{dynamic} l + f_{stiction} d \quad (3.1)$$

From simulation studies, linear dependency of the deflection on the laser power was found. Then the equation can be rewritten,

$$l = \frac{1}{f_{dynamic}} \frac{mC^2P^2}{8\Delta t} - \frac{f_{stiction}}{f_{dynamic}} d \quad (3.4)$$

where C is a proportion constant specific to each device ($C = 6.3 \times 10^{-5}$m/W for 15μm device and 1.2×10^{-4}m/W for 25μm device), and P is the laser power. The contraction time, Δt does not vary much (150±10μsec). I fit the data sets with two free fit parameters, $f_{stiction}$ and $f_{dynamic}$.

The step measurements supplies additional test method for determining the walking model. If I see the equation (3.4), the laser power has a squared dependency, not a linear dependency, because I assume the inertial impact model. But if the inch-worm model is assumed, the slide will be proportional to the laser power. To verify these models, I tried the power of the laser power as the third fit parameter. The parabolic equation (3.4) can be fit to each dataset to produce the stiction, $f_{stiction}$ to be 11±10pN and 100±10pN each for 15μm and 25μm devices (same order hereafter) and the dynamic friction, $f_{dynamic}$ to be 11±5pN and 45±10pN, and the powers were 1.9±0.5 and 1.5±0.5, supporting inertial impact model. When $f_{dynamic}$ is divided by the total contact area 27nm^2 of a device, the shear stress of the HOPG

can be calculated as 0.4±0.2MPa and 1.6±0.4MPa. The results are comparable to shear stress measurements of other graphite materials, 0.4MPa [129-131].

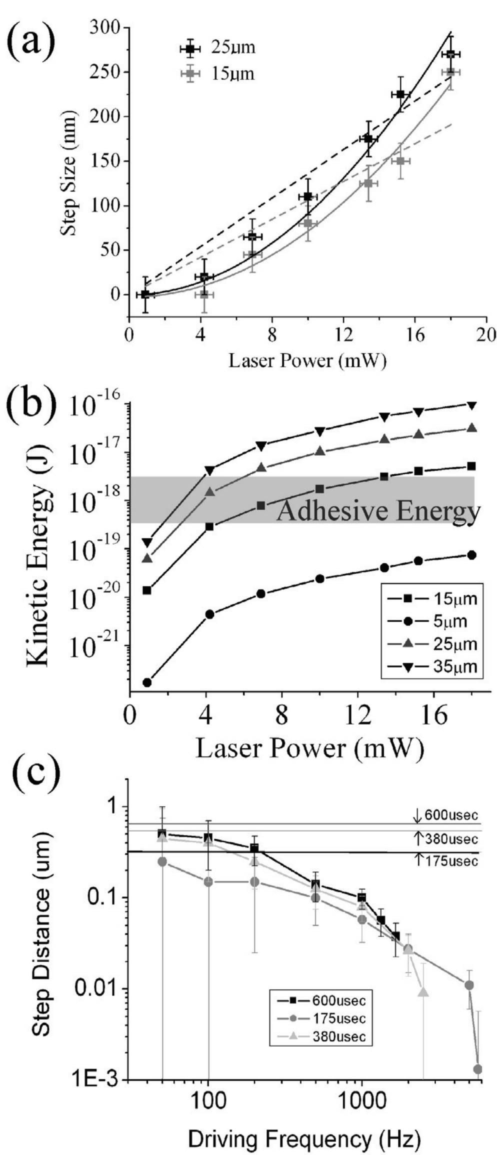

Figure 3.17 Velocity dependencies on laser parameters. (a) Step size plots for 2 different sized devices depending on the laser power. The dots are measurements and the continuous curves (black for 25µm, gray for 15µm) are fit equations from (3.4). Dashed lines are linear fit results assuming the inchworm model. For the 5µm long devices, no actuation was observed over the whole power range. (b) Simulated kinetic energy plot from equation (3.4). An adhesion barrier is assumed at around 10^{-18}J. (c) Observed steps of a device depending on the driving frequencies and pulse widths. The horizontal lines are calculated step sizes for each pulse width based on the frictions obtained in section 3.9.1.

3.9.2 Device Scaling

Figure 3.17a illustrates a scalability limit. Clearly the kinetic energy will be canceled by the stiction at a critical power or mass.

The kinetic energy is given in the left hand side of eq. (3.1). The deflection, D and contraction time constant, Δt depends on the size of a device, so will the kinetic energy. To calculate kinetic energy, the deflection, D can be calculated by eq. (2.1), and ΔT and Δt were simulated by Femlab with an assumed fixed laser power (18mW) on different sized devices. Equation (2.1) and (3.1) were combined to produce kinetic energy graphs in 3.17b.

In chapter 2 and in the previous section 3.9.1, the stiction was found to be 350pN and 25pN. Also from lateral force microcopy studies on graphite, the magnitudes of friction with nano-contacts are in the range up to 100pN to 1nN [30-33, 132]. If a device translates itself, each contact should slide a distance at least of its contact diameter, 3nm. Thus I have an energy barrier of a range, 3×10^{-19}J ~ 3×10^{-18}J. The simulated kinetic energy of a 5μm legged device is entirely dominated by the adhesive energy barrier. This explains the incapability of 5μm long legged device. In short, there is a scale limit in inertial impact thrust.

3.9.3 Dependence on Frequency

Other methods for controlling the velocity are to control the driving frequency and the pulse width. It can be expected that the velocity is proportional to the frequency. In other words, the step sizes will be constant over a given frequency, and larger pulse widths will produce faster speeds due to an enlarged deflection. I tested this with a 25μm long legged device in the driving range, 20 ~ 5000Hz with three different pulse widths, 175μsec, 380μsec and 600μs at the power 18±2mW. The measurements were obtained using the same video

tracking method described in the previous section, 3.10.1. One note on the measurements is that, of several clips showing different velocities for each configuration, only the clip showing the fastest speed was selected. Figure 3.17c shows the collection of measurements which have three obvious features. First, when the pulse width becomes larger so does the velocity. Second, when the driving frequencies approach 1kHz, the velocities decreased rapidly. When the intervals of the neighboring pulses are smaller than the natural cooling time (600μs), the amount of repeated deflections shrank due to incomplete thermal cycles. The third tendency is that steps in the range of 100~1kHz are 2 ~ 5 times smaller than lower frequencies, unlike the expectation. I attribute this to the stochastic nature of the progression of the devices. The step sizes are not uniform and higher frequencies indicate more trials on steps, thus a larger number of sizes are averaged. Also, the selection of the fastest velocity clips added to the uneven step observation. I interpret that steps measured with lower frequencies are closer to the maximum possible step distances while the values at higher frequencies are closer to average step distances. This is supported by the fact that the calculated steps are close to the values in the low frequency range.

3.10 Steering

The selection of an intended heading for a locomotive device offers great advantages over simply translating in a linear path when considering potential applications. Usually, steering needs additional sub-components inside a device, like the SDA device [95]. But in my device, I only need to control the direction of the transformed momentum. One contact with relatively smaller friction slides toward the junction of the spokes, while the remaining two are standing. Since my devices have three contacts, the friction of any specified contact

will be smaller than the combined frictions of the remaining contacts. The problem is then reduced to choosing a specific contact to slide.

3.10.1 Thermo-Mechanical Response Asymmetry

There are two factors defining the direction. When the primary laser spot illuminates one spoke, the spoke starts to curl and the curling motion confines the device object to a one dimensional movement parallel to the axis of the spoke toward the junction. In this case, the friction of the sliding spoke will be smaller than the other two. Then direction of the movements is determined by a simple selection of the laser spot location among the three spokes. Figure 3.18c shows the fidelity of controlled driving by displaying the writing of letters of the alphabet. For an intermediary heading, two legs are used alternatively in a zigzag pattern to achieve an intended direction.

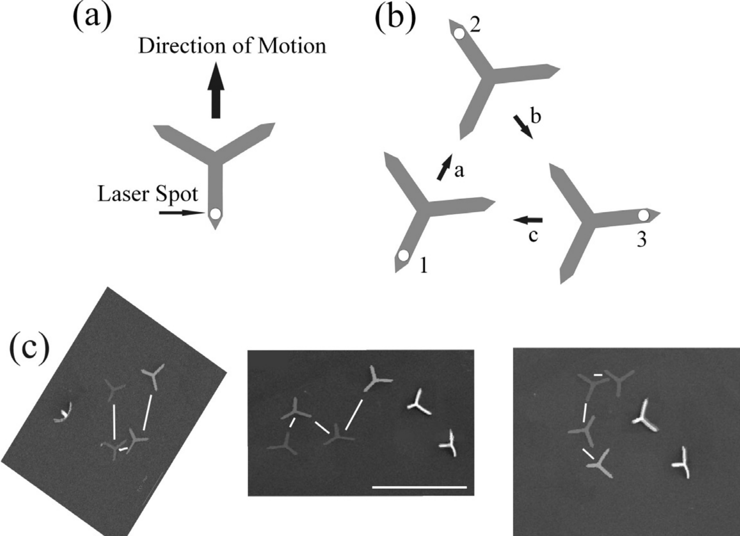

Figure 3.18 Demonstration on steered movements. (a), (b) By the selection of the location of the laser, heading of a device is selected. (b) If the laser is at location 1 (2 or 3), the device will move in ‘a’ (‘b’ or ‘c’) direction. (c) The writing of initials, 'U', 'N', and 'C'. Note that other stationary devices are translation references. The scale bar is 120µm long. The gradations of the device shade are due to overlaps of multiple partial transparent SEM images taken after each stoke at the optics stage.

There is a delay in the transfer of heat energy inside a device. When a laser is aimed at the tip of a spoke, the spot area experiences a thermal stress ahead of the rest of the device for a few micro-seconds at the early stage of heating (compare locations ‘a’ and ‘g’ in Figure 3.14c). The local preceding stress forces the chosen spoke’s contact to slide before the others. Once this contact starts to slide, it will remain the sole sliding contact until the device receives an impact. The asymmetry of the thermal stress will be maximized when a laser is set at the tip of the spoke. If instead it is set at the center of the device, the device will lose the asymmetry necessary to generate a momentum. I can expect that the velocity of a device will depend on the location of the laser along a spoke.

The delay was measured by the reflection method using an upside-down device. First, both the primary laser and the secondary laser were set to location A in Figure 3.19a to record a reflection upon a thermal vibration. Next, only secondary laser was moved to location B to detect the delay. The graph in Figure 3.19b shows initial 40μs of each contraction phase reflection at both locations. As expected in the Figure 3.14c, the delay was measured to be 5±3μs.

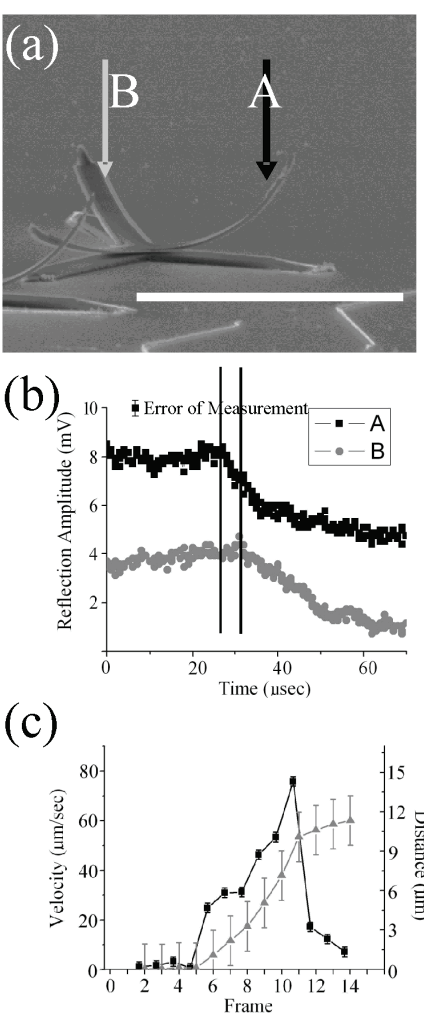

Figure 3.19 Velocity dependency on laser location. (a) An SEM picture of an upside down device used for time response measurements. The primary laser was set at the location A. The scale bar is 40μm long. (b) The records of the secondary laser reflections at A and B at the initial phase of thermal curving. The reflections drop because the thermal bending starts at around 25μsec in the graph. Black waveform was taken at the location A and gray one from B. The detected delay is displayed between vertical guide lines. (c) Time evolutions of the velocity and movement distance (black dots for velocity and gray dots for distance.). 1 Frame equals 1/25 second.

3.10.2 Velocity Dependence on the Laser Location

As a second prediction from the asymmetry, the velocity will depend on the location of the laser along a spoke. It is expected that the speed will be maximized when the laser is at the tip and that it will be minimized when the laser is at the junction. In the velocity

measurements the position of the laser was held steady and the device actuated itself along the spoke. A 25μm legged device was used with the laser parameters, 18±2mW, 500Hz, and 600μsec pulses. Figure 3.19c shows the acceleration of the device as the laser is effectively scanning along one spoke. The laser was initially set to half of a spoke. Then the device started acceleration and at the moment the laser escaped the device, the device slowed down at frame 11. Although the graph shows only one instance, this behavior was common to all three legs of the device. When the laser was set to the center of a device, it either walked randomly with significantly reduced speed or stood still.

3.11 Behaviors of Devices under Friction

In chapter 2 and in section 3.9, I estimated the friction per device of 25~350pN, which is weaker than the combined adhesion calculated in the existence of humidity. Although the strength of stiction is relatively small, once a contact is clutched to a location on HOPG, the device will act like a spring storing mechanical energy. When the contact is suddenly released, the stored energy will be large enough to eject the device from the adhesive contact. The observations show that the ejection from the graphite plane was rare in air even though in some cases one contact could be loose so that two contacts are still held down resulting in a turn-over.

The situation becomes quite different in vacuum experiments. Instantaneous ejections of devices were observed shortly after (typically within a minute) a modulated illumination began. Inside a vacuum environment the water molecules are easily vaporized. Thus there remains only vdW force for the adhesion, 1.5nN per contact, reduced from 6nN as I

calculated in section 1.4. This reduced attraction can explain the high probability of device loss. From the above observations it is thought that a humid condition is more favorable for the actuation of devices. Also an increased humidity was found to decrease the friction. The beneficiary effect of water was confirmed by previous studies using AFM contacts [133-135]. Further research should be conducted to address the optimization on the humidity.

As a final note on the surface friction, the dependency on the location can also be addressed. In the section 3.10, I explained that a temporal response asymmetry inside a device was induced by the location of a laser and also that the asymmetry disappeared when the laser was set to the center of a device. Even so, the movement did not completely disappear as the devices displayed random walk behavior. I can estimate that the contribution of the friction could manifest itself when the laser induced driving does not work. When the laser was set to a corner of a device, the inertial effects dominate the friction, and a unidirectional translation was possible. However in some cases, a device reacted in the opposite direction from what was expected, and the device was attracted towards the laser spot. This can happen if the friction of a single contact is larger than the other two contacts. More often the devices were observed to act as designed until it arrived at some location and it switched in direction so that the laser attracted the devices. It can be interpreted that the contact of the illuminated leg became much larger at a specific location on the HOPG and that it acted like an anchor. The HOPG is known to have a non-uniform friction coefficient depending on the location of the AFM tip [32, 113, 129]. Not only from the crystalline direction but also on the edges between them the value could be different by a magnitude of 10 times [31, 32, 113]. I suggest that this non-uniformity plays major roles in increasing the surface friction.

The contact radius was found to be 4nm in chapter 1. If I use this information, the combined adhesion per device (three contacts) will be 20nN. The combined attraction is much larger than the weight of the devices (~100pN). Because of the strength of the surface forces, awkwardly standing devices, which will not be possible in the macroscopic sense, were often found (Figure 3.20).

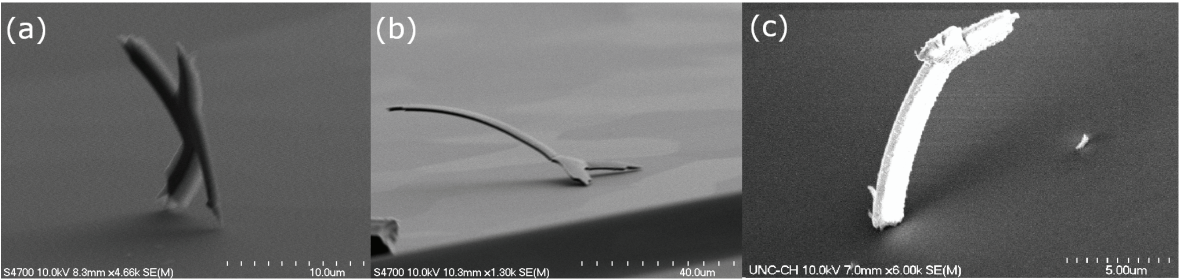

Figure 3.20 Various devices standing with 2 contacts ((a) and (b)) and 1 contact (c). The contacts will have multiple asperities to support the structures.

3.12 Consideration on Miniaturization Limits

I have already seen that there is a scale limit for 20μm long device. But there is still room for reduction. In this research, I adjusted only lengths, not the thickness and width. There are technical fabrication limits if all dimensional parameters are reduced. For example, if the thickness is reduced to 100nm, the metal films are not released from dry etching process due to insufficient film stresses. Then purely in a theoretical sense I will consider a theoretical miniaturization limit with two restrictions: (1) The device still uses inertial impact drive, and (2) the device temperature stays under melting temperature of the metal film.

A natural starting point is the equation (3.1). First I will estimate how the slide distance, l will depend on a representative length, L of a device. It will be desirable for

miniaturization if l does not strongly depend on L. Let us think of my device as a long box shaped bimorph with the longest dimension as L. I can think of two methods of scaling; linear and volumetric. The linear scaling means control of only L leaving width and thickness of the box same. The volumetric scaling means control of all dimensions in proportions. For example, width scales 1/10 of L, and thickness scales 1/100 of L. The slide distance l depends on mass, m, deflection, D, and natural relaxation time, Δt. I will assume nano-contacts as supports of the device without friction scalability. This assumption will be reasonable with a nano-contact, because, if a contact area is reduced below a nano-meter, surface forces will remain roughly equivalent due to surface forces such as capillary force. From eq. (2.1), deflection will be,

$$D = \frac{3L^2\varsigma}{t}C \quad (3.5)$$

where t is total thickness of bimorph box, C is a scale-independent constant determined by ratios of elastic properties of two films and their thicknesses. I assume a thermal strain with a constant temperature change, ΔT. Then I have the thermal strain, $\varsigma = \Delta\alpha \times \Delta T$, where Δα is difference of thermal expansion rates. Depending on scaling method, D will depend on different power laws of L.

$D_V = C_V L\Delta T$ (V:volumetric, 3.6) $D_L = C_L L^2 \Delta T$ (L:linear, 3.7)

From equation (3.1),

$$l \propto \frac{mD^2}{(\Delta t)^2} \quad (3.1)$$

I have two scaling dependencies on step distance, l,

$$l_V \propto \frac{L^3(L\Delta T)^2}{(\Delta t)^2} \propto \frac{L^5(\Delta T)^2}{(\Delta t)^2} \quad (3.8) \qquad l_L \propto \frac{L(L^2\Delta T)^2}{(\Delta t)^2} \propto \frac{L^5(\Delta T)^2}{(\Delta t)^2} \quad (3.9)$$

Now I need to know the size dependencies of ΔT and Δt. To make the problem simple, I will consider the box in air with only one dissipation process, convection. Laser power, P impinges on a device and the convection cools the device with a proportional constant, h. If heat capacitance is assumed as c_p, I have the energy balance equation,

$$P = hA(T - T_{amb}) + c_p m \frac{dT}{dt} \quad (3.10)$$

where P is laser power, A is total surface area, and T is temperature. Then the time constant, $\Delta t = \frac{c_p m}{hA}$ and saturated temperature, $\Delta T = \frac{P}{hA}$ will be $\Delta t_V \propto L$, $\Delta t_L \propto L^0$, $\Delta T_V \propto L^{-2}$, and $\Delta T_L \propto L^{-1}$. As a comment, non-scalability of time constant in linear mode is confirmed by simulation study in earlier section. Finally I have equation (3.8) and (3.9) in revision,

$$l_V \propto \frac{1}{L} \quad (3.8\text{`}) \qquad\qquad l_L \propto L^3 \quad (3.9\text{`})$$

I have already seen the result (3.9`) in the section 3.9. The step size of a device increased with leg extension at a given laser power. The step increased with an extended leg, although the step ratio between them is smaller than expected by eq. (3.9`). I also have seen that miniaturization limit for linear reduction is about 10μm long leg with 3μm width and 600nm thickness, which is overall 20μm long device. But equation (3.8`) suggests that volumetric reduction is better for miniaturization with fixed power. Then the problem is the absolute magnitude of a step under the limits of device melting and friction.

Let us consider a device made of carbon nanotubes. Metal-carbon nanotube bimorphs can be mechanical actuators by bending themselves (see appendix A). The imaginary device has three single-wall or multi-wall nanotube bimorphs to stand on a surface with nanotube tips as its contacts. Let us assume further that the diameter of the carbon nanotube is 1% of it

length. Then the volume and surface area will be, $V = \pi 10^{-4} L^3 m^3$, $A = 2\pi 10^{-2} L^2$. Density and heat capacity will be similar to those of graphite. $\rho_{graphite}$=2.3x10^{3}kg/m^3, c_p=8.0x10^{2}J/kg·K. Then I have time constant, Δt and saturated temperature, ΔT,

$$\Delta t = \frac{c_p m}{hA} = \frac{8.0\times10^2 J/kg\cdot K\times7.1\times10^{-1}\times L^3 kg}{9.0\times10^3 W/K\cdot m^2\times2\pi\times10^{-2}\times L^2 m^2} = L\sec \quad (3.11)$$

$$\Delta T = \frac{P}{hA} = \frac{PW}{9.0\times10^3 W/K\cdot m^2\times2\pi\times10^{-2} L^2 m^2} = \frac{P}{560L^2}K \quad (3.12)$$

From equation (2.1), I get deflection, D.

$$D = \frac{3L^2\varsigma 2}{0.01L} / \left(\frac{Y_{Al}}{Y_{CNT}} + 14 + \frac{Y_{CNT}}{Y_{Al}}\right) \cong 20L\varsigma \quad (3.13)$$

where $Y_{Al}/Y_{CNT} \sim 1/100$ was assumed. The difference of thermal expansion is 2.0x10^{-5}/K, allowing us to calculate the temperature change from eq. (3.12). Finally I have the inertial force (kinetic energy divided by contact diameter) from equation (3.1),

$$InertialForce = \frac{K.E.}{0.01L} = \frac{2.3\pi\times10^{-1} L^3 kg\times(20L\times2\times10^{-5}(P/560L^2))^2}{0.01L\times8\times(L)^2} = \frac{4.6\times10^{-10} P^2}{L^2}$$

(3.14)

If a device thrusts itself, its inertial force should be larger than friction. In chapter 2 and this chapter, I found that the friction is 10~100pN. Now I have two restrictions on power and length from equation (3.12) and (3.14). The temperature change (3.12) should be lower than melting temperature of metal (Al), 933K, and the thrust (3.14) should be larger than 100pN. Finally I have two inequalities.

$\frac{P}{560L^2} < 900$ (3.15) and $\frac{4.6\times10^{-10} P^2}{L^2} > 10^{-10}$ (3.16)

If I make the above expressions equal and draw graphs, I have Figure 3.21. If a device walks without melting, the power should be below eq. (3.15) but above eq. (3.16). This indicates that there is minimum length at 1μm with 0.5μW. The maximum deflection per thermal cycle will be 100nm from (3.13). The kinetic energy will be 1.2×10^{-21}J. A step distance will be given by the kinetic energy divided by friction, 0.1~1Å, which is similar to atomic scale. This means that the device will barely walk, since the friction can be as low as 10pN from my results in section 3.10. The natural time constant is from (3.11), 1μs. So the possible maximum velocity will be 10^{-5}m/sec.

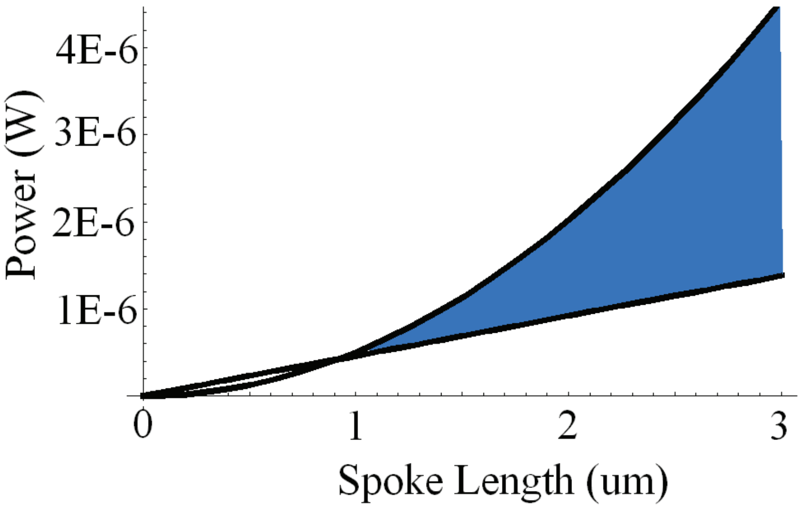

Figure 3.21 Parameter space plot for the device feasibility. Blue colored region means a device can walk against friction without melting.

3.13 Summary of Chapter 3

In this final section I will discuss a few remaining technical problems and give conclusions.

One problem is off-axis movement. Mostly the headings of a device were skewed and, in some minor cases, there were torques in the normal direction out of the substrate. Fortunately, if I use other legs in the correct order, the devices can be driven toward a desired location, but with the requirement of additional maneuvers. The reason for such skewing can be easily understood if one observes a top-down SEM picture of a device. The lengths of all three legs are rarely identical, but rather are minutely different, although they are designed to be equal. Also some of the legs are twisted. Incomplete fabrication was inevitable to some degree.

Now I can summarize new facts found and what I learned from this chapter.

1. I proved that the thrust came from the inertial impact through thermal modulation.

2. The devices are the smallest walking devices ever built. The size of the smallest device fabricated is 30μm long. This point is important because I wanted to build a miniaturized device. Besides, the capability of steering was also achieved with no additional parts incorporated in the device or treatments on the substrate. In terms of application, the structural simplicity and such minimum requirements have greater advantages over any other devices developed by others.

3. The double layer beam bending equations described the structural deformation and natural time constant of a device with given laser power and dimension of a device. These are verified by analytical calculations, simulation studies, and comparisons with measurements. This information is valuable for the design and prediction of the performance of various devices.

4. The inertial impact drive has been demonstrated in a macroscopic device (more than 1mm size) in other literature [136]. The inertial impact was employed in a mobile micro-device for the first time in this research.

5. By repetitive contractions with minimal friction, a micro-object can thrust itself by sliding rather than by footsteps-like walking. The control of the slide distance could be achieved through laser parameter controls.

6. Through the understanding of control mechanism, a miniaturization limit could also be elucidated. I also understand that the sizes of my devices are close to the theoretical limit in the linear scaling fashion. For example, a 15micron long legged device was capable of moving, but not 5micron legged one.

7. By the selection of the laser spot location, a mechanical deformation asymmetry arises inside the body of a device, which can be used for steering. The degree of asymmetry was measured and found to be consistent with the simulation study.

APPENDIX

Appendix A: Metal-Multiwall Carbon Nanotube Bimorph Actuator

A.1 Causes of Strain and Bimorph Bending Theory

In this appendix, I will discuss a kind of fixed thermal actuator composed of a metal film and a multiwall carbon nanotube. As seen in the chapter 1, the thermal stress is greater than any other types of actuations in magnitude. Also it has an additional advantage of simplicity by controlling the temperature of the device itself without an additional component.

Since the discovery by Iijima, carbon nanotubes (CNT) have been shown to have useful properties in electronic and mechanical applications. Carbon nanotubes are essentially graphene in cylindrical form. It can be imagined as a rolled graphite sheet with a direction. Its radius can be as small as 1nm with a shell only one atom in thickness. Depending on the rolling direction (also called chirality), its electronic properties can be either metallic or semi-conducting. If a carbon nanotube has just one shell, it is called a singlewall carbon-nanotube. If it has multiple concentric shells, it is called a multiwall carbon-nanotube. The mechanical sturdiness of carbon nanotubes makes them good candidate for mechanical MEMS devices. Their tensile strength is greater than any other known material [137, 138] and it has a high Young's modulus [139].

If a carbon nanotube is used as a template of a bimorph, it supplies a basis for a micro-actuator due to its smallness in length and diameter. I used carbon nanotubes grown by

the arc-discharge method [140, 141], which are a few microns in length and up to 100nm in diameter. Although the nanotubes' diameters are usually in nanometers to tens of nanometers, their resilience to breaking is extremely good under bending [142, 143]. Thus, carbon nanotubes are ideal materials for bimorphs.

Three goals of this project are: (1) Measurement of the thermal expansion coefficient of multiwall carbon nanotubes; the amount that a bimorph deflects is determined by a difference of thermal expansions of two materials and if I know the property of one of the two materials. In this research, I used Al as the other material, whose thin film elastic property is known from other studies. (2) The compliance of the bimorph capability to the bimorph bending equation; although my devices are only microns in size, they can be treated by continuum mechanics. Under a given temperature change, I can predict the deflection with the thickness of the Al film, the diameter of carbon nanotube, and elastic properties of both materials. (3) Demonstration of nanometer actuation by nanotube bimorphs; the thermal bending with carbon nanotubes is a promising nano-actuation method, and at the time I started this research, it had not been attempted.

I can generate nano-meter actuations from a micron sized metal-nanotube bimorph actuator. A metal film can be unevenly deposited on the surface of a nanotube. To simplify the calculation, I can think of a carbon nanotube as a 'thin film'. To analyze thermal bending, I need a bimorph bending theory. Let me assume that my bimorph has a length, L, a radius of curvature, R, and that it has a rectangular cross-section in a double stack with thicknesses of each layer, t_a and t_b. The material properties of the two films are assumed to be homogeneous and isotropic with Young's moduli of Y_a and Y_b respectively. An internal stress of a film or a

difference of stresses between the two films generates a deflection. Whatever the cause of an internal stress, a curvature can be generated by a mechanical strain, ζ [126].

$$\rho = \frac{1}{R} = \frac{\varphi}{L} = \frac{6\zeta(t_a + t_b)}{t_a t_b} \times \left[\left(\frac{t_b}{t_a} \right)^2 \frac{Y_b}{Y_a} + 4\frac{t_b}{t_a} + 6 + 4\frac{t_a}{t_b} + \left(\frac{t_a}{t_b} \right)^2 \frac{Y_a}{Y_b} \right]^{-1} \quad \text{(A.1)}$$

where ρ is the curvature, ζ is the strain, Y is the modified Young's modulus, E/(1-ν), where E is Young's modulus, and ν is the Poisson ratio. In the induction of eq. (A.1), a small deflection approximation, $D \cong L\varphi/2$ is assumed, where φ is an angular difference of tangents at the root and tip of a bimorph. In my bimorph actuators, there exist two kinds of stress. The first kind is the intrinsic stress. In the case of thermal stress, ζ becomes $\Delta\alpha \times \Delta T$, where $\Delta\alpha$ is the difference of thermal expansion coefficients of the two materials, and ΔT is the change of temperature.

The intrinsic stress generated during an evaporation step is the cause of an initial curvature and it is often quite large (up to a few GPa). Due to such a large magnitude it may exceed the strength of metal films used as, for example, interconnects in VLSI. Thus, it has been a processing and reliability concern for the microelectronics industry. Origins of intrinsic stress in a film extend beyond simple temperature difference during a deposition [144]. Changes in volume during the formation of the film can lead to intrinsic stress [145]. Grain morphology evolution after a deposition can be another cause [102]. Intrinsic stress can also develop from the coalescing of islands of material during the initial stages of film formation [144, 146]; stress was found to exist in these islands because of lattice mismatches. Although sputtering is not used in my fabrication method, the gas pressure of bombarding ions has an effect on the intrinsic stress [147]. Even if the same material is plated, the stress depends strongly on the plating method [148, 149].

Before any thermal actuation, SEM pictures of the bimorphs were taken and their curvatures were obtained by a graphical analysis tool. Some parameters in equation (A.1) could be measured directly. The thickness of each layer will be measured in the pictures and the Young's modulus of an Al film is well known (70±20GPa) [150-152]. Then I fit the initial curvatures with equation (A.1) to get the intrinsic strains, ζ of metal films.

When the bimorph undergoes a thermal cycle, it experiences a thermal strain. The variation of the curvature is measured by a change of the tip angle. With a preset temperature variation, ΔT, I can obtain a fit result to the thermal strain, which yields α_{CNT}.

A.2 Fabrication, Bending Experiments

A.2.1 Nanotube Cartridge Preparation and Cold Evaporation

I fabricated suspended CNT cartridges on AFM tipchips by depositing CNTs from a suspension onto the backs of atomic force microscope (AFM) cantilevers. After breaking the AFM cantilevers I found nanotubes protruding from the broken cantilever edges. These cartridges were anchored to a cooled stage in the thermal evaporator. I found that evaporating metal onto a nominally room-temperature cartridge led to metal migration on the surface of the CNT and eventual uniform encapsulation. After the stage was cooled to 150K, Cr or Al was evaporated. On the cooled stage, Al covered the CNTs only on one side. It should be noted that, although the temperature of the stage could be measured accurately, the temperature of the CNT itself during evaporation was difficult to estimate and could have been substantially warmer. The cartridge was allowed to warm up to room temperature in vacuum over hours after the evaporation was completed.

Transmission electron microscope (TEM) images provided measurements of the thicknesses of the metal and the CNT. Cr and Al both formed bimorph structures. They exhibited a

variety of grain morphologies that depended on evaporation temperature, evaporation rate and other environmental factors that are difficult to asses. Since Al tended to deposit more smoothly and since it has a greater coefficient of thermal expansion coefficient than Cr, I used Al in all further work. I fabricated samples with Al thicknesses from 4nm to 140nm. The thicker films displayed a variety of grain morphologies as illustrated in Figure A.3. For each different tipchip, different thickness of Al film was deposited. For tipchip 0813, it was 22±5nm, for 0821, 4±1nm, for 0910, 49±12nm, and for 0927, 66±15nm. Although control of metal thickness was possible, it was not possible to control diameters of carbon nanotubes, as they were randomly distributed.

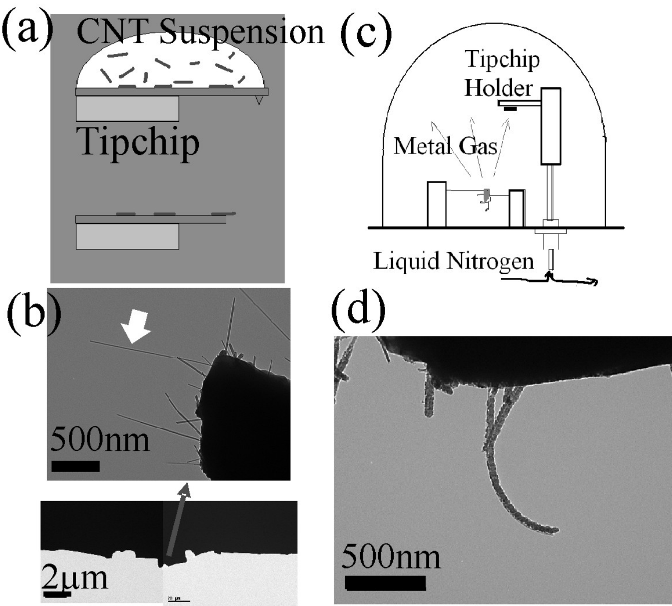

Figure A.1 Cold evaporation. (a) Carbon nanotubes are suspended over an edge of a broken cantilever. (b) TEM pictures show protruding tubes. The multiwall carbon nanotubes are initially straight. (c) A schematic of the cold evaporation method. Liquid nitrogen flows through a pipeline that passes through a feedthrough. (d) A TEM picture after the cold evaporation. The carbon nanotube is the same as in (b). (white arrow) The sample stage holding the tipchip was rotated 45° to reveal the bending. The metal (Al) film is inside of the curve. The nanotubes were found bent due to residual stress of Al film.

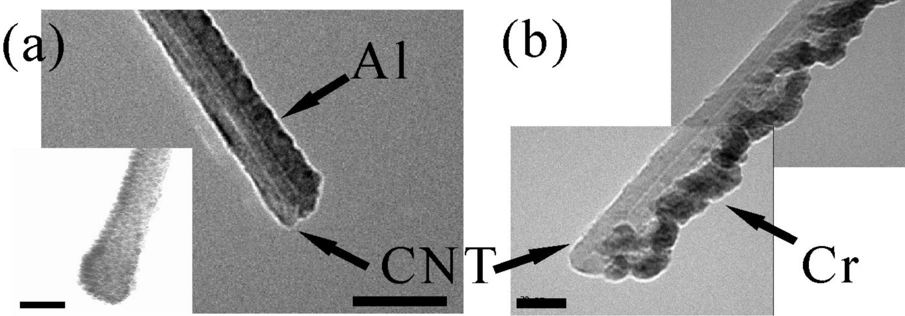

Figure A.2 Metal depositions on carbon nanotubes. (a) An angled TEM picture of Al-CNT bimorph. Inset: Al evaporated at non-cooled stage. CNT is completely covered by Al film. The scale bars are 50nm. (b) A Cr-CNT bimorph. The scale bar is 20nm.

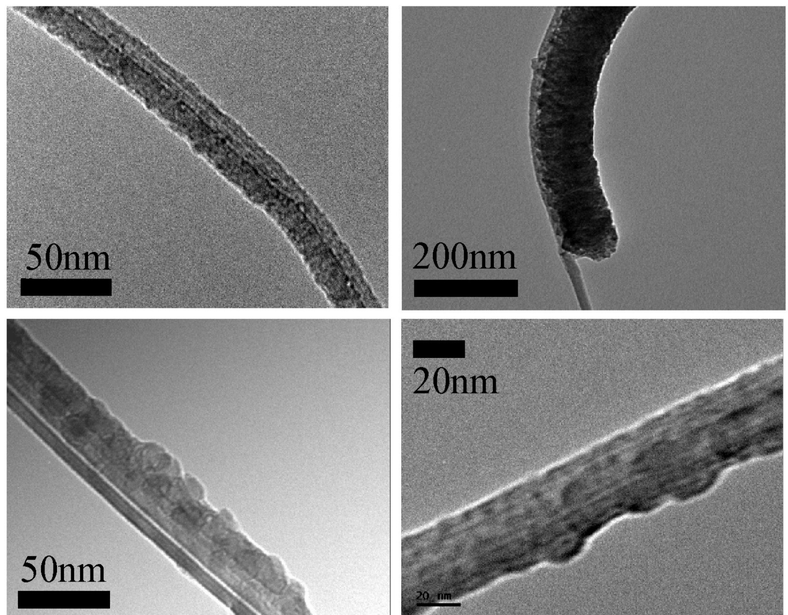

Figure A.3 Various Al depositions.

A.2.2 Thermal Bending Experiments

Thermal bending experiments were done inside an SEM chamber while the electron beam continuously imaged the bimorphs. A home-built thermal stage was prepared that could be mounted on an SEM sample sledge (Figure A.4). A feedthrough in the SEM chamber was bored to provide power to the thermal stage. The driving power (30W for the

heater) was supplied from a temperature controller and the voltage was lowered through a transformer from 110V to 3V according to the specification of the heater. The power was transferred through an electric relay, which controls the flow of the power circuit. The control signal for the relay was supplied from a source meter to the relay. When the control voltage from the source meter is larger than a threshold value ("ON" signal), the relay allows the power to the heater until the surface of the heater reaches a targeted temperature. Nominally a temperature change of 170K was set for the temperature controller throughout the entire thermal bending experiments. A thermocouple buried inside a copper cap converts the temperature into a voltage, which is routed back to the temperature controller as feedback.

Because the thermal capacity of a tipchip is much smaller than the copper cap (2% of copper cap from a simple calculation) and there is only trace amounts of gas to cool the surface of a tipchip inside the SEM sample chamber, the temperature of a tipchip is assumed to be same as the copper cap.

The thermal stage has a 45° slant angle so that curvature of the bimorphs could be imaged by the electron beam. To record the bending, a minimum of three pictures were needed. One picture was taken before the heating phase, a second picture was taken at a specified elevation temperature, and after the cooling phase, a final picture was taken. A comparative analysis of these pictures provides a quantitative estimate of deflection. The whole process was repeated if more thermal cycles were needed. Figure A.6 is a series of such SEM pictures in two thermal cycles.

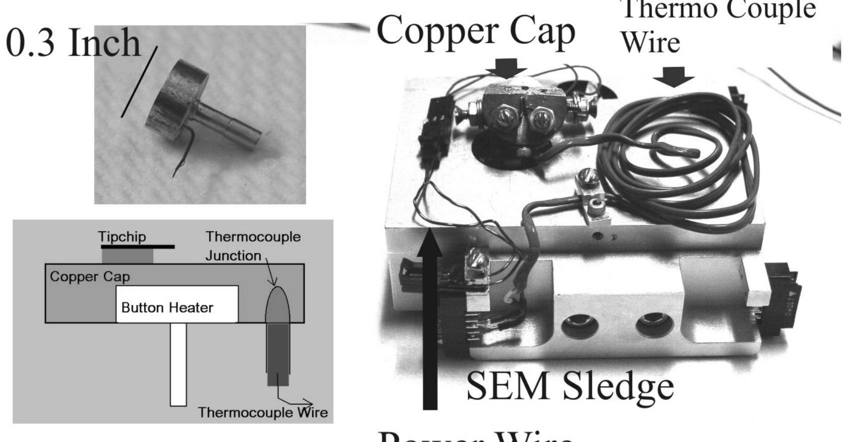

Figure A.4 SEM sample sledge and button heater.

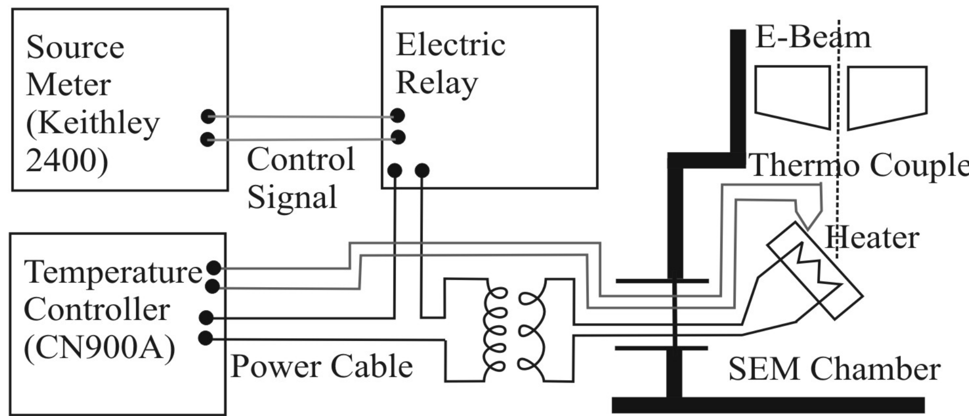

Figure A.5 Diagram of experimental setup

Item	Model	Vendor
UHV Button Heater	101136	HeatWave Labs, Inc.
Temperature Controller	CN9000A	Omega
Source Meter	2400	Keithley
Electric Relay	SSRL240DC10	Omega
Thermo Couple Junction	K type	Omega

Table A.1 Parts List

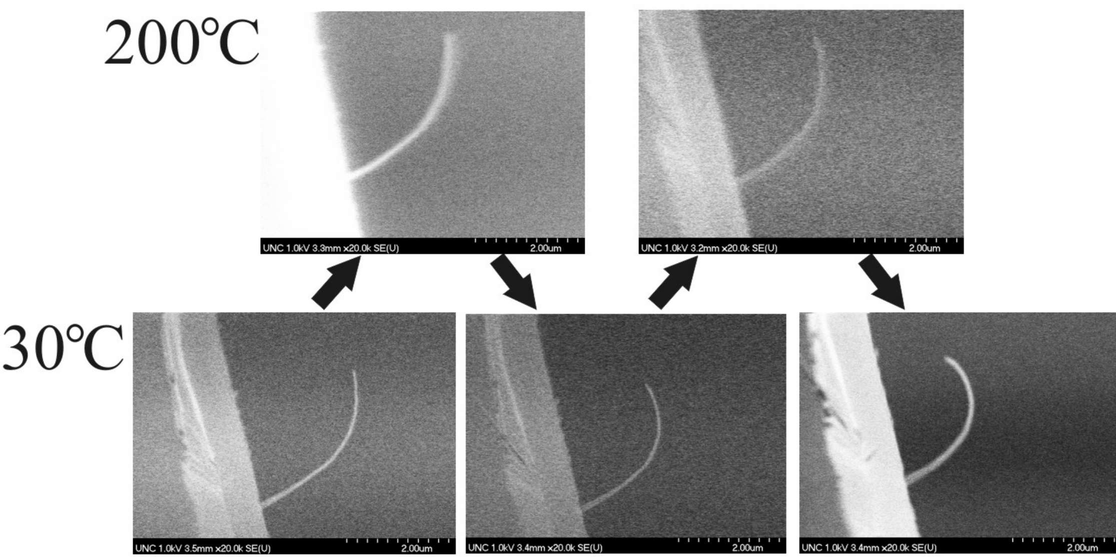

Figure A.6 Variation of curvature in two cycles of temperature shuttling between 303K and 473K. The bimorph stretches because the metal layer is along the inner edge of the curvature (leftside in above pictures).

A.3 Analysis

A.3.1 Graphical Analysis Tool

Because all of the data are images that contain critical geometrical (angular and linear) information, image information extraction software is needed. I used home-built software called, “Tube Tracer” developed at the UNC department of computer science department [127]. The software is developed to find a ‘track line’ along a tubular-shaped structure in a two-dimensional gray scale image. A cross section of the tubular object can be thought of as a profile of the brightness variation. The software finds the edges where the brightness changes most dramatically (Figure A.7b). The numerical center of the two edge pixels is determined to be the center pixel. If this method of edge finding is continued along a path of the tubular object, a series of centers makes a track. The distance between the edges becomes the ‘diameter’ of the object. The track output parameters consist of four elements, x coordinate, y coordinate, radius in pixels, and tangent angle in radians. The tangent angle is

the angle defined by two consecutive pixels. The horizontal direction of the image is defined as zero radian and the angle increases in the counter clockwise direction.

When the track data is obtained, the tangent angle data was extracted and fit to a line assuming that the bimorph has a constant curvature. If an initial curvature is of concern, the tangent angles at the root and the tip were subtracted to give the initial bending angle. If instead the curvature variation was of concern, data from two tracks, one obtained at the room temperature and the other obtained at high temperature, were compared to find the difference in the tangent angles at the tip. By considering the bending plane with respect to the electron beam direction, a true angle could be calculated in both cases above.

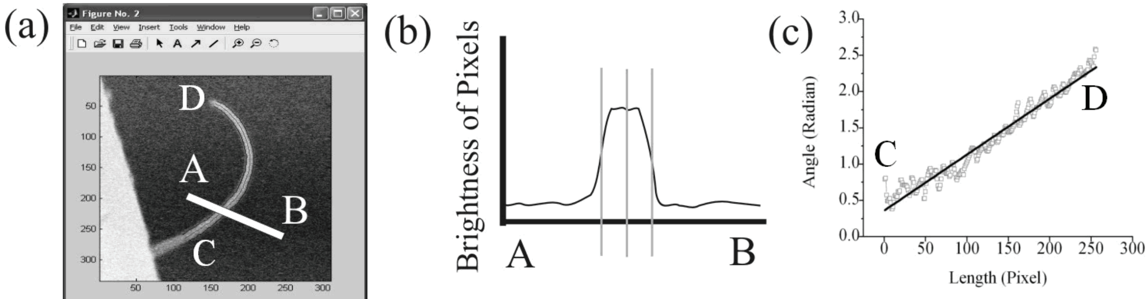

Figure A.7 Tube tracing algorithm. (a) A track software window. (b) A schematic shows how the software determines center pixel. 'A' and 'B' are end points in the Figure (a). (c) An angular track result with a fit line. An angular difference between 0 pixel (location C in image (a)) and 250pixel (location D) in the graph is a bending angle.

A.3.2 Curvature Correction

Before doing further analysis, I need to consider two things; verification of the small deflection assumption and the dependence of bending on the cross-sectional shape. Measurements on thicknesses, bending angle, and length and calculated curvature are supplied in Table A.2. In the bending angle column in Table A.2, some bending angles are as large as 100°. Although the bending angles are not small, the assumption is still valid (see

appendix B for an explanation.). Secondly, equation (A.1) assumes a doubly stacked rectangular box, which is an oversimplification. This point is illustrated by TEM (transmission electron microscope) images of middle portions of the bimorphs at different observation angles. The pictures in Figure A.8 suggest cylindrical cross sections of the Al layer rather than a rectangular box. Thus the metal film and CNT share a cylindrical shape, which will modify mechanical properties of a bimorph significantly. To verify this, finite element analysis was done to compare deflections in two different configurations; rectangular cross-section and cylindrical cross-section (Figure A.9a). First I did bending simulation in the rectangular cross-section with a thickness of Al film and a diameter of CNT. The ratio (thickness ratio defined as the metal thickness divided by the diameter of CNT) was varied from 1 to 7 in steps of 2. Next I did same bending simulation in the cylindrical cross-section with identical thicknesses and their ratio. To simulate an intrinsic or a thermal bending, I assumed a mechanical strain in the Al film. Whatever the cause of strain, the quantity is a pure number expressing an extension rate for a given length. Then I can represent an intrinsic or thermal stress bending with a mechanical strain, ζ. A mechanical strain of 0.2%, which is a close number to the ones obtained in the following analyses, was assumed in Al film on both models regardless of their thickness ratio. The simulated results show great differences between the two models in the amounts of deflections when the metal thicknesses were increased to 3 ~7 times the CNT diameter.

Based on above simulation results, I corrected all the curvature measurements to supplement the cross-sectional difference. Assuming a phenomenological square-root dependence of the deflection ratio (the deflection magnitude of the cylindrical cross-sectional model divided by that of the rectangular model, see Figure A.9b.), the curvature correction

factor is $0.085+1.54\sqrt{x}$, where x is the thickness ratio. Then the measured curvatures in the sixth column of Table A.2 were divided by this factor to give corrected curvatures in the final column. The correction was also applied to the thermal bending results in Table A.3.

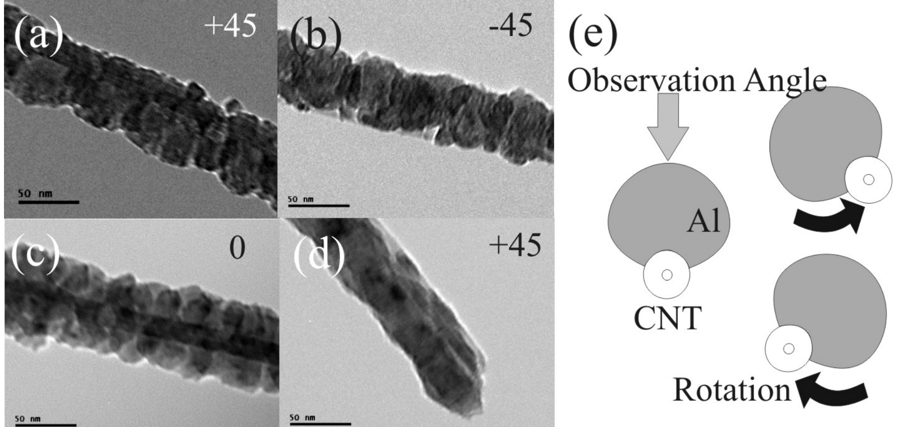

Figure A.8 Cross-section of Al film. (a) and (b) TEM images of a Al-CNT bimorph in two different observation angles. A carbon nanotube can be seen shaded by the metal film close to a top edge in (a) and to a bottom edge in (b). 0 degree corresponds to top view. (c) and (d) TEM pictures of another bimorph in two different angles. (e) Explanitory cartoon. The arrows mean the rotational direction of sample stage.

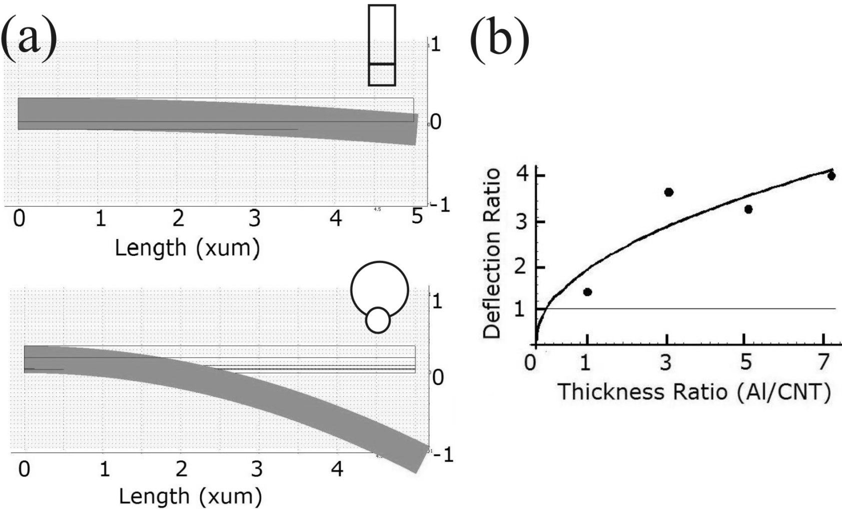

Figure A.9 Simulations on two cross-section model. (a) Simulated results for the two different cross sections. Thickness ratio is 3:1 (Al:CNT). (b) A graph of the deflection ratio dependence on the thickness ratio. The continuous curve assumes a square-rooted dependency on thickness ratio, x. (Deflection Ratio = $0.085+1.54\sqrt{x}$)

A.4 Intrinsic Curvature

Curvature was calculated by φ / L, where φ is the bending angle from an imaginary straight device, and L is the length of the bimorph. Thicknesses of the metal films and diameters of nanotubes were measured from TEM pictures. The Young's modulus of the Al film is assumed to be 70GPa (bulk). The mechanical properties of nanometer-thick Al films have been measured by other group [153], and the values were close to the bulk value. Furthermore its variation is only fractional (~4%) in the thickness range of 50~150nm. Several theoretical and experimental publications estimated the elastic property of multi-walled carbon nanotubes to be 1TPa regardless of tube diameter and chirality [139, 154-158]. Although there are some theoretical publications of the dependence of Young's modulus on the nanotubes diameters, these studies focused single-walled nanotubes and the variation of the elastic property came from primarily sub-nanometer diameter tubes [159, 160]. As can be seen in the Figure A.10, diameters of my nanotubes are much larger than 1nm. Thus I can set Y_{cnt}=1TPa. For each tipchip having different metal thickness, corrected curvatures were fit to the equation (A.1) with a free parameter, $\zeta_{intrinsic}$. The fit result for intrinsic strain of $\zeta_{intrinsic}$ is in Figure A.11.

The strain increased weakly depending on thickness of metal film with strains, 0.4~1.3±0.1%. The number is larger than the strain limit (0.3%) found in a stress-strain measurement with thin aluminum films [161]. In some extreme cases with a different metal thin film (Au), more than 10% of stretching was also reported, thus the number is not too divergent [162, 163]. Such a dependency of the strain on thickness can be understood by a reduction in Young's modulus, but the amount of change in the graph requires a variation of elastic property of the metal film by a factor of 10, which is hardly plausible. Therefore I

speculate that there is only a minor contribution from the variation of elastic property of Al film, but the major contribution came from thicknesses of the metal films. Figure A.11 is interpreted that a thicker metal film has stronger compression. Also metal film stress dependencies on varying thickness have been reported before [104, 144, 164-166].

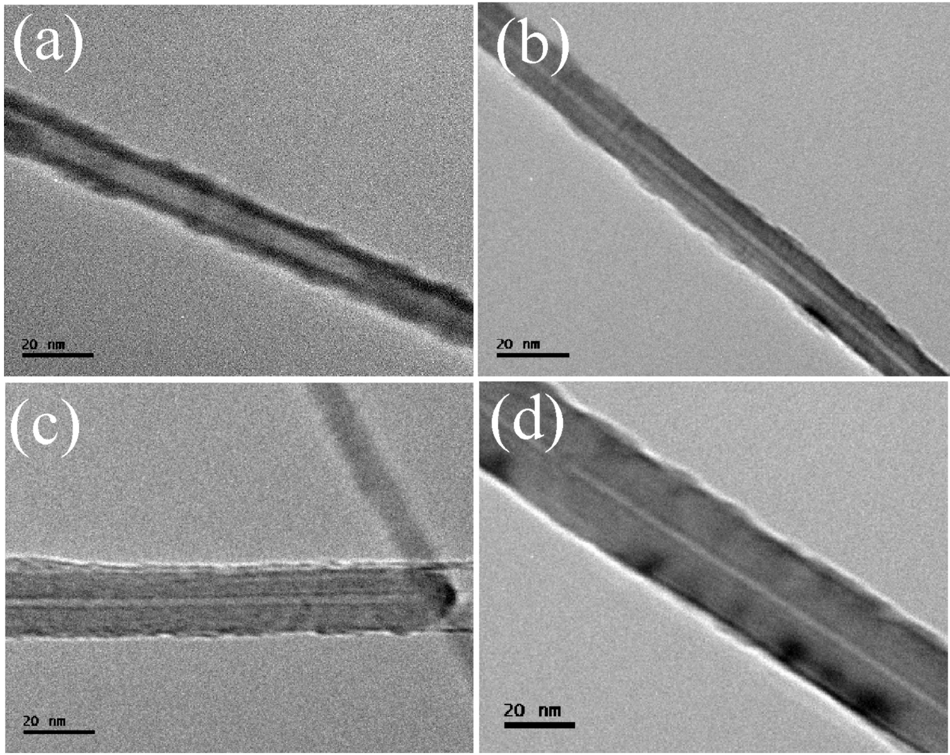

Figure A.10 High magnification TEM pictures on bare. All scale bars are 20nm long.

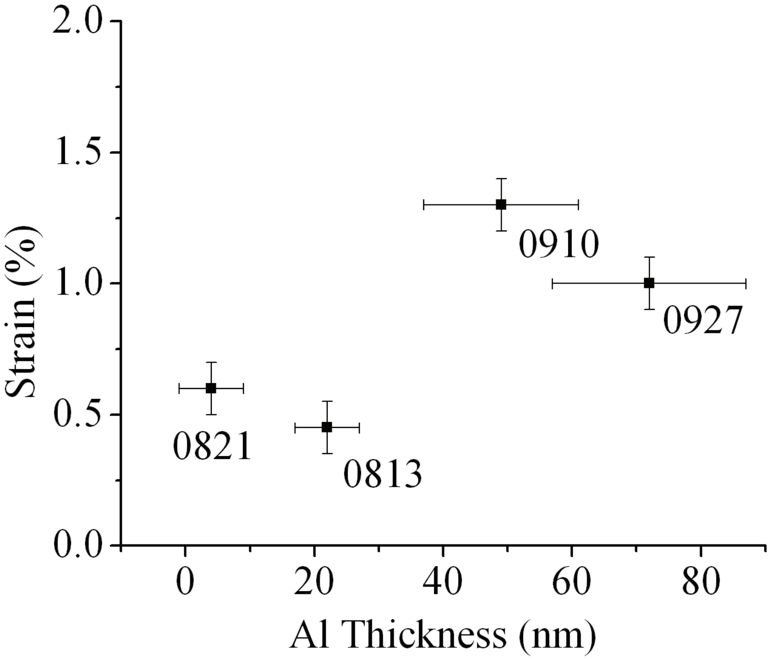

Figure A.11 Fit result plot on metal film strain, ζ for each tipchip. Each data point is obtained by a fit from multiple data in the same tipchip. The name of each tipchip is written beside a data point.

A.5 Thermal Curvature Change

In this analysis, the software tool and the analysis method are identical. This time, however, the intrinsic curvature in the previous section is replaced by the change of the existing curvature and the intrinsic strain is replaced by the thermal strain. The measurements are summarized in the Table A.3. In this second fit process, I assumed the same Young's modulus for the carbon nanotubes, 1TPa. Thus the only free fit parameter is the thermal strain, $\zeta_{thermal}$. Equation (A.1) is again fit to the corrected curvatures to give the thermal stain. Figure A.12 shows 0.3~0.7±0.1% of thermal expansion for the metal films at a temperature change 170±3K.

I want to make a few comments about the thermal strains. First, the thermal bendings were in the expected direction, i.e. when a bimorph was heated, it stretched because the aluminum film is inside the curve, and when it cools to room temperature, it folded backward. The bending direction is repeatable, but the amounts of bendings were not identical under multiple actuations. However a progressive reduction of deflection amplitudes was not observed up to third thermal cycle. Instead the amplitudes fluctuated. (For example, 0813-1 in the table A.3) This is clear in the SEM pictures in the Figure A.6. This suggests that this irregularity of bending amplitudes is not from thermal migration of metal atoms. TEM pictures after thermal cycles support this point (Figure A.13). What were found after multiple thermal cycles were thick layers of amorphous carbon materials created by continuous exposure to the electron beam. This unwanted buildup is a suspected cause of the irregular bendings through modifying elastic properties of the bimorph. The continuous exposure was needed to track the location of the bimorph on the tipchip. When the tipchip experiences a temperature variation, the whole structure also expands bringing the electron microscope out of focus, if the electron beam focus does not follow the thermal drifts. Thus, to reduce the influence of amorphous carbon, only bendings in the first cycles were used for the fit.

Second, the strain can be converted to the thermal expansion coefficient of the carbon nanotubes. The essential information of exact thermal expansion of the one dimensional aluminum film of nanometer thickness is not known, however if I use the coefficient of thermal expansion of thin Al film, 2.3×10^{-5}/K [167], α_{CNT} is found to vary from $5\pm2\times10^{-6}$/K to $-1.8\pm2\times10^{-5}$/K at ΔT=170K. However this range is very large, if I compare it to the range of thermal expansion coefficients of most elements in the periodic table ($0 \sim 3\times10^{-5}$/K).

Although theoretically large axial contraction of multiwalled carbon nanotubes under the 500K temperature elevation has been reported (-1×10^{-5}/K) [168], my measurements are too scattered to provide a conclusive number.

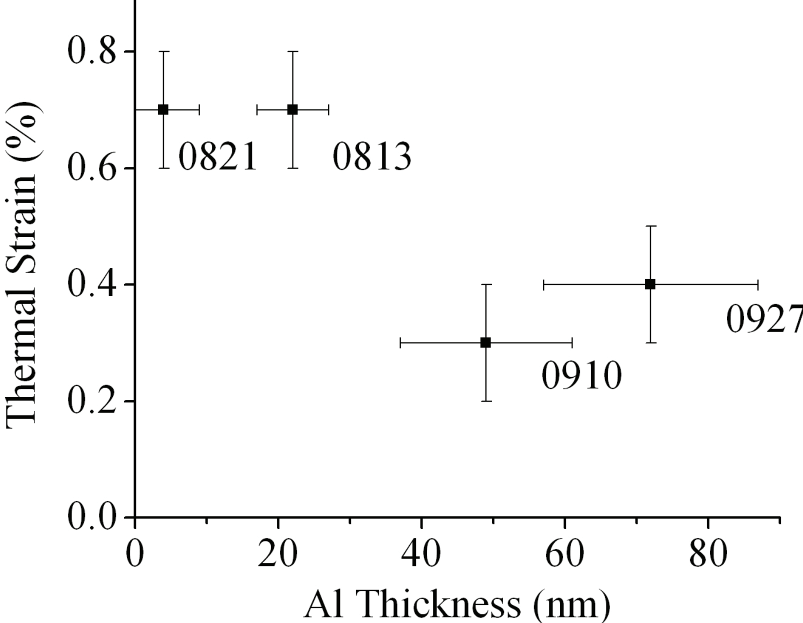

Figure A.12 Fit results on thermal strain. Each data point is obtained by a fit from multiple data in the same tipchip. The name of each tipchip is written beside each data point.

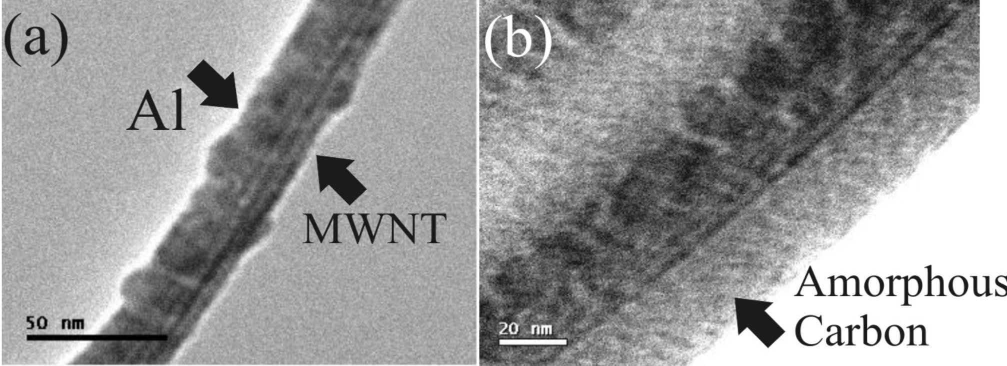

Figure A.13 Accumulation of amorphous carbon. (a) A TEM picture before any thermal actuation test. (b) A TEM picture at the same location in (a) after multiple thermal bending experiments. A thick covering amorphous carbon films are deposited due to electron beam scanning.

A.6 Conclusion

In this appendix, I demonstrated repeatable deflections from Al-carbon nanotube bimorphs. Thin metal films were deposited on one side of multi-wall carbon nanotubes to make double layer bimorphs. Right after the cold evaporation step initial curvatures were found and it is believed that the internal film stresses during the evaporation phase causes initial bendings. The intrinsic strain was found to be 0.4~0.7±0.1% depending on thickness and the numbers agree to other thin film strain tests. A temperature variation of 170K generated 0.3~0.7±0.1% thermal strains. Thermal bending was in the expected direction, but the magnitudes of deflection were not entirely repeatable. When the thermal strain is converted to α_{CNT}, it ranged from 5 to $-18\pm2\times10^{-6}$/K. The true value can be inside this range, but my results are limited from being more specific.

In summary, the goal of my research, demonstrations of nano-actuations, was achieved. However I could not reach conclusions on the other two goals: thermal expansion of carbon nanotubes and the compliance of bimorph actuators to the bending equation.

Although I could not achieve the other two goals, there are suggestions for better measurements. The scatter of α_{CNT} came from imprecise measurements on some quantities such as elastic properties of one-dimension Al film.

If I examine equation (A.1) again, there are 5 parameters determining curvature, ρ; ζ, t_{CNT}, t_{Al}, Y_{CNT}, and Y_{Al}. The elastic properties of carbon nanotubes have been measured and predicted as uniform over wide range of diameters by other studies. Thus the value Y_{CNT} =1TPa can be used safely. The curvature is calculated from the bending angle and length of

each bimorph, which were measured from SEM pictures. Also the thickness of each film was measured from TEM pictures. The precision of those quantities is ~10%.

To my knowledge, there has not been a measurement of the elastic properties of thin Al film that is close to one-dimensional structure. I tried to obtain a novel measurement for one property of carbon nanotubes, but actually I was also dealing with another material whose elastic property is not known. Naturally the first amendment of the research will be the quality of Al film. Ikuno et al [169] achieved a superior quality of Al films through a pulsed laser deposition technique (actually aluminum oxide film in the publication.). Their TEM picture shows a continuous and homogeneous film. Also measurement of Y_{Al} can be done by other techniques such as X-ray diffraction [170, 171].

The second suggestion regards the measurement of a temperature change. In equation (A.1) there is another measurement, a temperature change in the thermal strain, $\zeta_{thermal}$, which is another source of error. From the discussion in section A.5, a temperature change of 170K is assumed, but there can be a temperature gradient between the thermocouple and the tipchip. Moreover, repeatability of the temperature cycle is also questionable. As can be seen in the Figure A.4, the thermocouple was located inside the copper cap. However, if the temperature of the tipchip could be measured by putting a thermocouple junction right at the back of a tipchip, measurement precision will be greatly enhanced. It is recommended that the design for temperature detection be revised.

Finally, the thermal curvature changes will be more uniform over individual bimorphs if carbon nanotubes that have similar diameters are used [172-175]. If diameters of nanotubes are similar, their bending moments will be similar. Then deflections will be identical under

uniform Al thicknesses and temperature change, which will make it easier to extract the thermal expansion properties of CNTs.

Name of Bimorphs (Tipchip-Bimorph#)	Thickness of Metal (nm, Error=±5nm)	Diameter of Nanotube (nm, Error=±5nm)	Length (um, Error=±0.2µm)	Bending Angle (°, Error=±5)	Curvature (m^{-1})	Corrected Curvature (m^{-1})
0813-1	26	13	2.2	64	226841	159325
0813-2	23	9	1.7	46	219441	115300
0813-3	21	17	1.1	67	449302	509092
0813-4	16	12	2.1	63	241997	250580
0813-6	17	14	1.2	15	106076	109161
0813-7	29	15	0.85	2	21533	14064
0821-10	4	11	0.99	2	22644	70229
0821-5	4	14	0.76	6	73176	279059
0821-6	4	12	2.4	20	72533	245065
0910-1	70	23	1.5	24	140130	59643
0910-2	47	12	1.3	138	551199	299734
0910-3	40	18	1.4	22	133845	77353
0910-4	38	14	0.79	98	840767	506128
0910-5	59	20	0.81	45	457328	208145
0910-6	33	9	1.1	48	344398	127596
0910-8	55	13	2.8	55	154434	50570
0910-9	49	16	2.6	104	253630	140102
0927-1	100	47	1.2	27	405719	120692
0927-3	60	10	0.52	26	435097	95042
0927-4	65	29	1.1	22	174535	99937
0927-5	77	10	1.2	43	308396	54234
0927-6	74	11	1.2	79	490437	110656
0927-7	58	15	3.2	59	146695	53105

Table A.2 Measurements on thickness of metal film, diameter of CNT, bimorph length, bending angle, and initial curvature calculation with corrected curvature.

Name	Al Thickness (nm,Error =±5nm)	CNT Diameter (nm,Error=± 5nm)	Length (um,Error=± 0.2µm)	Bending Angle (°,Error=±5°)	Change of Curvature (m^-1)	Corrected Curvature Change (m^-1)
0821-5 first heating(stretching)	4	14	0.75	2	46144	50990
0821-5 first cooling(curling)	4	14	0.75	2	46144	50990
0821-3 first heaing(stretching)	6	38	0.51	4	134354	193441
0821-3 first cooling(curling)	6	38	0.51	4	134354	193441
0813-1 first heating(stretching)	21	17	1.1	17	267860	149647
0813-1 first cooling(curling)	21	17	1.1	15	236347	132041
0813-1 second heating(stretching)	21	17	1.1	3	47269	26408
0813-1 second	21	17	1.1	3	47269	26408

cooling(curling)						
0813-1 third heating(stretching)	21	17	1.1	15	236347	132041
0813-1 third cooling(curling)	21	17	1.1	6	94539	52816
0813-2 first heating(stretching)	26	13	1.9	9	80219	35583
0813-2 first cooling(curling)	26	13	1.9	33	294136	130472
0813-2second heating(stretching)	26	13	1.9	11	98045	43490
0813-2 second cooling(curling)	26	13	1.9	34	303050	134425
0813-2 third heating(stretching)	26	13	1.9	25	222830	98842.
0813-2 third cooling(curling)	26	13	1.9	9	80219	35583
0910-4 first heating(stretching)	38	14	1.1	18	270770	103652
0910-4 first cooling(curling)	38	14	1.1	15	225641	86377
0910-3 first heating(stretching)	40	18	1.4	4	47292	19939
0910-3 first coolign(curling)	40	18	1.4	21	248284	104683
0910-2 first heating(stretching)	47	12	1.3	18	239135	76624
0910-2 first cooling(curling)	47	12	1.3	2	26570	8513
0910-9 first heating(stretching)	49	16	2.6	11	71147	25689
0910-9 first cooling(curling)	49	16	2.6	7	45275	16347
0910-7 first heating(stretching)	50	21	2.8	4	24179	9860
0910-7 fist cooling(curling)	50	21	2.8	3	24179	9860
0910-5 first heating(stretching)	59	20	0.81	7	149567	54993
0910-5 first cooling(curling)	59	20	0.81	2	42733	15712
0927-6 first heating(stretching)	74	11	1.1	3	45860	11285
0927-6 first cooling(curling)	74	11	1.1	25	382173	94044
1021-2 first heating(stretching)	122	23	1.2	9	144584	39962
1021-2 dirst cooling(curling)	122	23	1.2	11	144584	39962
1021-1 first heating(stretching)	143	31	0.75	8	184477	54584
1021-1 first cooling(curling)	143	31	0.75	7	161417	47761

Table A.3 Measurements on thermal bending parameters. Parameters are identical to except that the bending angle is change of angle from thermal bending.

Appendix B: Consideration on Small Angle Approximation

From Gehring et al [126], a deflection, Δ is assumed to be (see Figure B.1),

$$\Delta \cong \frac{D\varphi}{2} \quad \text{(B.1)}$$

where D is projected length of a bimorph arc and φ is bending angle of the bimorph. In exact calculation, it is also,

$$\Delta = R(\sin\varphi - \tan\frac{\varphi}{2})\tan\varphi \quad \text{(B.2)}$$

To compare them, I need to convert D into R with a bending angle, φ.

$$D = (2R^2(1-\cos\varphi))^{1/2} = R(2(1-\cos\varphi))^{1/2} \quad \text{(B.3)}$$

Then D is inserted in (B.1).

$$\Delta \cong \frac{\varphi}{2} R(2(1-\cos\varphi))^{1/2} \quad \text{(B.4)}$$

If the above equations are plotted from 0 to π/2, I have Figure B.1, (b). At 90°, their difference is only about 10%, which is small deviation. In conclusion, I can safely use the deflection equation (2.1) even a bending angle is close to 90°.

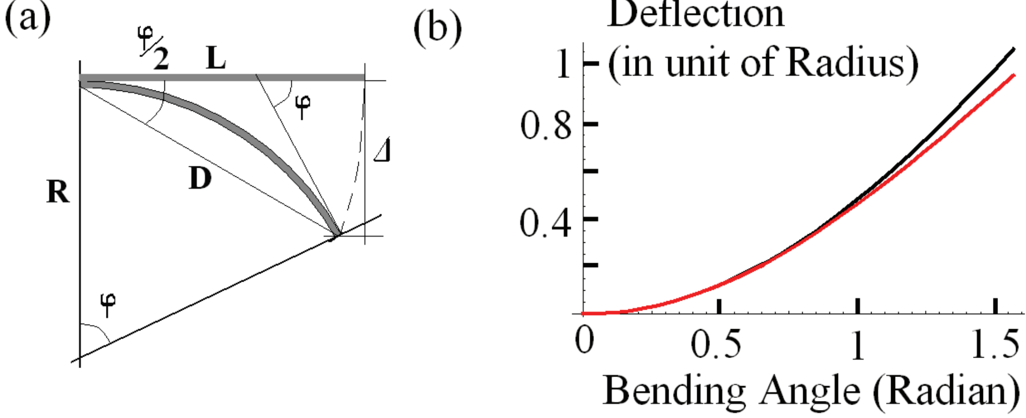

Figure B.1 Large deflection approximation. (a) A drawing on deflection calculation. (b) Comparison of equation (B.2) and (B.4). Black curve from (B.4) and red curved from (B.2).

Appendix C: Determination of the Absorptivity of A Thin Au Film

The arguments below are from Bauerle [176]. The absorption properties of a bulk material and a thin film are different, and I need to determine that 5nm (= h_s, s means substrate.) Au film is a thin film. For this purpose, I will calculate penetration depth, (also called skin depth) l_α.

$$l_\alpha = \sqrt{\frac{2\rho}{2\pi f \mu_0 \mu_r}} \quad (C.1)$$

where ρ is bulk resistivity, $2.2\times10^{-8}\Omega\cdot m$, f is frequency of impinging light, 100~1kHz, μ_0 is permeability constant, $4\pi\times10^{-7}$H/m, μ_r is relative permeability, 1. When calculated, l_α turns out to be 60nm, which is much thicker than my film. For weak to moderate absorption (l_α>h_s), multiple-reflection within the slab cannot be ignored and the absorptivity becomes dependent on the thickness of the slab, i.e., A=A(h_s). Let us consider the situation for uniform irradiation of a slab with permittivity ε_s, in an ambient medium with ε_M = 1. Due to energy conservation, the absorptivity, A, is related to the reflectivity, R = $|r|^2$, and transitivity, D=$|d|^2$, by A + R + D = 1.

The amplitude reflection, r, and transmission coefficients, d are given by

$$r = \frac{r_{Ms}[1 - \exp(-i2\psi))]}{r_{Ms}^2 - \exp(-i2\psi)} \text{ and } d = \frac{(r_{Ms}^2 - 1)ex[(-i\psi)}{r_{Ms}^2 - \exp(-i2\psi)} \quad (C.2)$$

where

$r_{Ms} = \frac{1-\sqrt{\varepsilon_s}}{1+\sqrt{\varepsilon_s}}$; $\psi = \frac{2\pi h_s}{\lambda}\sqrt{\varepsilon_s} = k_l h_s \sqrt{\varepsilon_s}$ and $\sqrt{\varepsilon_s} = n + i\kappa$, where λ is wavelength, n and κ are real and complex refraction indices respectively. For the finite thickness, weak absorption,

l_α>h_s, $R = \frac{(1-n^2)^2 \sin^2(\frac{1}{2}\beta h_s)}{\xi}(1-A)$ (C.3)

$$A = 2\kappa \frac{(1+n)\beta h_s - (1-n)\sin(\beta h_s)}{\xi} \text{ (C.4)}$$

$$D = \frac{4n^2}{\xi}(1-A) \text{ (C.5)}$$

with $\xi = 4n^2 + (1-n^2)^2 \sin^2(\frac{1}{2}\beta h_s)$ and $\beta = 4\pi n/\lambda$. In case of Au with λ = 660nm, and $\sqrt{\varepsilon_s} = n + i\kappa_a$ = 0.2 + i 3.3 [11]. The value, A, is 0.08.

Appendix D: Determination of the Convective Heat Transfer Coefficient and Thermal Radiative Coefficient.

For preliminary preparation before calculation the convective coefficient, h, I will give definitions on some quantities related to this issue.

1. The Grashof number, Gr_L, is defined as the ratio of the buoyancy force to the viscous force in the fluid.

   $$Gr = \frac{g\beta(T_s - T_\infty)L^3}{\nu^2} \text{ (D.1)}$$

   where g is the gravitational acceleration, 9.8m/s^2, β is the volumetric thermal expansion coefficient, 0.0033K^{-1}, T_S and T_{inf} are temperatures of surface and at infinity, L is typical length, 10μm, and ν is kinematic viscosity of the air, 15.9×10^{-6}m^2/s.

2. The ratio of the momentum and thermal diffusivities is defined as Prandtl number and equal to the ratio of the kinematic viscosity over heat diffusivity.

   $$\Pr = \frac{c_p\mu}{k} = \frac{\nu}{\alpha} \text{ (D.2)}$$

where c_p is the heal capacity, μ is the viscosity, k is thermal diffusivity, and α is the heat diffusivity of the air, $22.5\times10^{-6}m^2/s$. For the air, this number is 0.71(unitless).

3. The Rayleigh number is the ratio of the inertial to viscous forces acting on a fluid element.

$$Ra = Gr \times \Pr = \frac{g\beta(T_S - T_\infty)L^3}{\nu\alpha} \quad (D.3)$$

From the numbers given above, the calculated value is

$$Ra = 3.0\times10^{-11}(T-293)$$

4. Nusselt number is the dimensionless temperature gradient at the surface and is defined as

$$Nu = \frac{hL}{k} \quad (D.4)$$

First, I will think of Nusselt number of vertical plate which is more precise than that of horizontal plates. For any Rayleigh number, the Nusselt number can be calculated by [112, 177]

$$Nu = \left\{0.825 + \frac{0.387Ra^{1/6}}{[1+(0.492/\Pr)^{9/16}]^{8/27}}\right\}^2 \quad (D.5)$$

From (D.2) and (D.4), the calculated Rayleigh number is,

$$Ra = \frac{g\beta(T_s - T_\infty)L^3}{\nu\alpha} = \frac{(9.8m/s^2)(0.0033K^{-1})(T-300K)(700\times10^{-9})^3(m^3)}{(16.2\times10^{-6}m^2/s)(22.9\times10^{-6}m^2/s)} = 3.0\times10^{-11}(T-300K)$$

(for vertical surface) (D.6)

The Nusselt number can be known if Ra and Pr are inserted in (D.5). Next, I will consider the top and bottom heated surface. From Incropera [112], the Nusselt numbers in each case,

(1) For upper surface of heated plate or lower surface of cooled plate:

a. $Nu = 0.54Ra^{1/4}$ (10^4<Ra<10^7) (D.7)

b. $Nu = 0.15Ra^{1/3}$ ($10^7 < \mathrm{Ra} < 10^{11}$) (D.8)

(2) For lower surface of heated plate or upper surface of cooled plate:

a. $Nu = 0.27Ra^{1/4}$ ($10^5 < \mathrm{Ra} < 10^{10}$) (D.9)

Unfortunately, the Ra number for my device in micrometer regime is too far smaller than 10^4, it makes impossible to use (D.7) to (D.9). Instead the same Nusselt equation in (D.5) will be used for both top and bottom plate without too much error.

From eq. (D.4), I can calculate h.

$h = 3.8\times10^4(0.68 + 0.0012\times(T - 293)^{1/4})W/m^2K$ (for all surfaces) (D.10)

Finally, I get the radiation constant, C.

C is the product of the Stephan-Boltzmann number and the emissivity of the materials.

$C = c \times \varepsilon$ (D.11)

where $\sigma=5.67\times10^{-8} W/m^2\cdot K^4$, $\varepsilon_{Al}=0.02$, $\varepsilon_{Cr}=0.17$

REFERENCES

1. Bohringer, K.P., Fearing, R. S., Goldberg, K. Y., *The handbook of industrial robotics*, ed. S. Nof. 1998: Wiley & Sons.

2. Israelachbili, J., *Intermolecular & surface forces*. 1992.

3. Bailey, A.I., *Friction and adhesion of clean and contaminated mica surfaces.* J. Appl. Phys., 1961. **32**(1407).

4. Bradley, R.S., *The cohesive force between solid surfaces and the surface energy of solids*. Phil. Mag. Vol. 13. 1932. 853.

5. Bhushan, B., *Principles and applications of tribology*. 1999.

6. Skriver, H.L., Rosengaard, N. M., *Surface energy and work function of elemental metals.* Phys. Rev. B, 1992. **46**(11): p. 7157.

7. de Boer, M.P., Luck, D. L., Ashurst, W. R., Maboudian, R., Corwin, A. D., Walraven, J. A., Redmond, J. M., *High-performance surface-micromachined inchworm actuator.* Journal of microelectromechanical systems, 2004. **13**(1): p. 63.

8. Bryant, P.J., Gutshall, P. L., Taylor, L. H., *Mechanics of solid friction.* 1964.

9. Hamaker, H.C., *Loden van der Waals attraction between spherical bodies.* Physica, 1937. **4**: p. 1058.

10. Vidali, G., Ihm, G., Kim, H. Y., Cole, M. W., *Cole. Surf. Sci. Rep.* 12, 1991(133).

11. Torii, A., Sasaki, M., Hane, K., and Okuma, S., *Adhesive force distribution on microstructures investigated by an atomic force microscope.* Sensors and Actuators A, 1994. **44**(2): p. 153.

12. Bowling, R.A., *Particle on surfaces 1: Detection, adhesion and removal*, ed. K.L. Mittal. 1988, New York: Plenum Press.

13. Werder, T., Walther, J. H., Jaffe, R. L., Koumoutsakos, P., *Water-carbon interactions: Potential energy calibration using experimental data.* Technical proceedings of the 2003 nanotechnology conference and trade show, 2003. **3**: p. 546.

14. Landman, U., Luedtke, W. D., Gao, J., *Atomic-Scale Issues in Tribology: Interfacial Junctions and Nano-elastohydrodynamics.* Langmuir, 1996. **12**: p. 4514.

15. Yoshizawa, H., Chen, Y. L., Israelachvili, J., *Fundamental Mechanism of Interfacial Friction. 1. Relation between Adhesion and Friction.* J. Phys. Chem., 1992. **97**: p. 4128.

16. Mak. C., K., J., *Quantz-crystal microbalance studies of the velocity dependence of interfacial friction.* Physical Review B, 1998. **58**(9): p. 5157.

17. Liebsch, A., *Density-functional calculation of electronic friction of ions and atoms on metal surfaces.* Physical Review B, 1997. **55**(19): p. 13263.

18. Liebsch, A., Goncalves, S., Kiwi, M., *Electronic versus phononic friction of xenon on silver.* Physical Review B, 1999. **60**(7): p. 5034.

19. Cieplak, M., Smith, E. D., Robbins, M. O., *Molecular Origins of Friction: The Force on Adsorbed Layers.* Science, 1994. **265**: p. 1209.

20. Persson, B.N.J., Zhang, Z., *Theory of friction: Coulomb drag between two closely spaced solids.* Physical Review B, 1998. **57**(12): p. 7327.

21. Bruch, L.W., *Ohmic damping of center-of-mass oscillations of a molecular monolayer.* Physical Review B, 2000. **61**(23): p. 16201.

22. Budakian, R., Putterman, S. J., *Correlation between charge transfer and stick-slip friction at a metal-insulator-interface.* Phys. Rev. Lett., 2000. **85**: p. 1000.

23. Pendry, J.B., *Shearing the vacuum - quantum friction.* J. Phys.: Condens. matter, 1997. **9**: p. 10301.

24. Persson, B.N.J., *Surface resistivity and vibrational damping in adsorbed layers.* Physical Review B, 1991. **44**(7): p. 3277.

25. Sokoloff, J.B., Tomassone, M. S., Widow, A., *Strongly Temperature dependent sliding friction for a superconducting interface.* Physical Review Letters, 2000. **84**(3): p. 515.

26. Dayo, A., Alnasrallah, W., Krim. J., *Superconductivity-dependent Sliding Friction.* Physical Review Letters, 1998. **80**(8): p. 1690.

27. Volokitin, A.I., Persson, B. N. J., *Noncontact friction between nanostructures.* Phys. Rev. B, 2003. **68**: p. 155420.

28. Carpick, R.W., Salmeron, M., *Scratching the Surface: Fundamental Invenstigations of Tribology with Atomic Force Microscopy.* Chemical Review, 1997. **97**: p. 1163.

29. Krim, J., *Friction at macroscopic and microscopic length scales.* Resource Letter, Am. J. Phys., 2002. **70**(9): p. 890.

30. Mechler, A., et al., *Cantilever flexure, adhesive/attractive and lateral force measurements on highly-oriented pyrolytic graphite by scanning force microscopy.* Vacuum, 1998. **50**(3-4): p. 281-287.

31. Muller, T., Kasser, T., Labardi, M., Lux-Steiner, M., Marti, O., Mlynek, J., Krausch, G., *Scanning force and friction microscopy at highly oriented polycrystalline graphite and Cup2(100) surfaces in ultrahigh vacuum.* J. Vac. Sci. Technol. B, 1996. **14**(2): p. 1296.

32. Ruan, J.A., Bhushan, B., *Frictional Behavior of highly oriented pyrolytic graphite.* J. Appl. Phys., 1994. **76**(12): p. 8117.

33. Ruan, J.A., Bhushan, B., *Atomic-scale and microscale friction studies of graphite and diamond using friction force microscopy.* J. Appl. Phys., 1994. **76**(9): p. 5022.

34. Tambe, N.S., Bhushan, B., *Identifying materials with low friction and adhesion for nanotechnology applicatioins.* Appl. Phys. Lett., 2005. **86**: p. 061906.

35. Tambe, N.S., Bhushan, B., *nanoscale friction mapping.* Appl. Phys. Lett., 2005. **86**: p. 193102.

36. Derjaguin, B.V., Muller, V. M., Toropov, Y. P., J. Colloid Interface Sci., 1975. **53**: p. 314.

37. Derjaguin, B.V., Churayev, N. V., Muller, V. M., *Surface forces.* 1985.

38. John, K.L., Kendall, K., Roberts, A. D., *Surface energy and the contact of elastic solids.* Proc. R. Soc. London, Ser. A, 1971. **324**: p. 301.

39. Maugis, D., *Adhesion of Spheres - The JKR-DMT Transition Using a Dugdale Model.* J. Colloid Interface Sci., 1992. **150**(1): p. 243.

40. Carpick, R.W., Ogletree, D. F., Salmeron, M., *A general equation for fitting contact area and friction vs. load measurements.* Journal of Colloid and Interface Science, 1999. **211**: p. 395.

41. Arai, F., Ando, D., Fukuda, T., Nonoda, Y., Oota, T. *Micro manipulation based on microphysics: Strategy based on attractive force reduction and stress measurement*. in *International Coference on Intelligent Robots and Systems*. 1995.

42. Drexler, K.E., *Nanosystems: Molecular Machinery, Manufacturig, and Computation*. 1992: Wiley & Sons.

43. Rida, A., Gijs, M. A. M., *Manipulation of self-assembled structures of magnetic beads for microfluidic mixing and assaying.* Anal. Chem., 2004. **76**: p. 6239.

44. Qiu, J., Lang, J. H., Slocum, A. H., Weber, A. C., *A bulk-micromachined bistable relay with U-shaped thermal actuators.* Journal of microelectromechanical systems, 2005. **14**(5): p. 1099.

45. Hickey, R., Kujath, M., Hubbard, T., *Heat transfer analysis and optimization of two-beam microelectromechanical thermal actuators.* J. Vac. Sci. Technol. A, 2002. **20**(3): p. 971.

46. Wang, R.X., Zohar, Y., Wong, M., *Residual stress-loaded titanium-nickel shapte-memory alloy thin-film micro-actuators.* J. Micromech. Microeng., 2002. **12**: p. 323.

47. Fu, Y.Q., Du, H., Huang, W., Zhaing, S., Hu, M., *TiNi-based thin films in MEMS applications: a review.* Sensors and Actuators A, 2004. **112**: p. 395.

48. Ree, M., Chen, K. J., Kirby, D. P., *Anisotropic properties of high-temperature polyimide thin films: Dielectric and thermal-expansion behaviors.* J. Appl. Phys., 1992. **72**(5): p. 2014.

49. Ebefors, T., Kalvesten, E., Stemme, G. *Dynamic actuation of polyimide V-grooves joints by electrical heating*. in *Eurosensors XI*. 1997. Warsaw, Poland.

50. Ebefors., T., Kalvesten, E., Stemme, G., *New small radius joints based on thermal shringage of polyimide in V-grooves for robust self-assembly 3D microstructures.* J. Micromech. Microeng., 1998. **8**: p. 188.

51. Ebefors, T., Ulfstedt-Mattson, J., Kalvesten, E., Stemme, G. *3D micromachined devices based on polyimide joint technology*. in *Conference on devices and process technologies for MEMS and microelectronics, SPIE*. 1999. Royal pines resort, Gold coast, Queensland, Australia.

52. Ebefors, T., et al., *A robust micro conveyer realized by arrayed polimide joint actuators.* Journal of Micromechanics and Microengineering, 2000. **10**(3): p. 337-349.

53. Miura, H., Yasuda, T., Fujisawa, Y. K., Shimoyama, I. *Insect-model based microrobot*. in *Transducers '95, Eurosensors IX, The 8th international conference on solid-state sensors and actuators, and eurosensors IX*. 1995. Stockholm, Sweden.

54. Jager, E.W.H., Smela, E., Inganas, O., *Microfabricating conjugated polymer actuators.* Science, 2000. **290**: p. 1540.

55. Smela, E., Kallenbach, M., Holdenried, J., *Electrochemically driven polypyrrole bilayers for miving and positioning bluk micromachined silicon plates.* Journal of microelectromechanical systems, 1999. **8**(4): p. 373.

56. Jager, E.W.H., Smela, E., Inganas, O., *On-chip microelectrodes for electrochemistry with moveable PPy bilayer actuators as working electrodes.* Sensors and Actuators B, 1999. **56**: p. 73.

57. Jager, E.W.H., Inganas, O., Lundstrom, I., *Microrobots for micrometer-size objects in aqueous media: Potential tools for single-cell manipulation.* Science, 2000. **288**: p. 2335.

58. Chan, H.Y., Li, W. J. *A thermally actuated polymer micro robotic gripper for manipulation of biological cells*. in *Proceedings of the 2003 IEEE International conference on robotics & automation*. 2003. Taipei, Taiwan.

59. Zhou, J.W.L., et al., *Polymer MEMS actuators for underwater micromanipulation.* Ieee-Asme Transactions on Mechatronics, 2004. **9**(2): p. 334-342.

60. Nguyen, N.T., S.S. Ho, and C.L.N. Low, *A polymeric microgripper with integrated thermal actuators.* Journal of Micromechanics and Microengineering, 2004. **14**(7): p. 969-974.

61. Bernstein, J.J., Taylor, W. P., Brazzle, J. D., Corcoran, C. J., Kirkos, G., Odhner, J. E., Pareek, A., Waelti, M., Zai, M., *Electromagnetically actuated mirror arrays for use in 3-D optical switching applications.* Journal of microelectromechanical systems, 2004. **13**(3): p. 526.

62. Van Kessel, P.F., Hornbeck, L. J., Meier, R. E., Douglass, M. R., *A mems-based projection display.* Proceedings of the IEEE, 1998. **86**(8): p. 1687.

63. Jain, A., Qu, H., todd, S. Xie, H., *A thermal bimorph micromirror with large bi-directional and vertical actuation.* Sensors and Actuators A, 2005. **122**: p. 9.

64. Ferriera, A., *Design of a flexible converyer microrobot with electromagnetic field-based friction drive control for microfactory stations.* Journal of microelectromechanical systems, 2000. **1**(1): p. 49.

65. Goosen, J.F.L., Wolffenbuttel, R. F. *Object positioning using a surface micromachined distributed system*. in *The 8th international conference on solid-state sensors and actuators, and eurosensors IX*. 1995. Stockholm, Sweden.

66. Nakazawa, H., Wantanabe, Y., Morita, O. *The two-dimentional micro conveyer*. in *1997 international conference on solid-state sensors and actuators*. 1997. Chicago.

67. Pester, K.S.J., Fearing, R. S., Howe, R. T. *A planar air levetated electrostatic actuator system*. 1990.

68. Guenat, O.T., Hirata, T., Akashi, T., Gretillat, M-A., de Rooij, N. F., *A pneumatic air table realized by micro-edm.* Journal of microelectromechanical systems, 1998. **7**(4): p. 380.

69. Konishi, S., Fujita, H., *A conveyance system using air flow based on the concept of distributed micro motion systems.* Journal of microelectromechanical systems, 1994. **3**(2): p. 54.

70. Suh, J.W., Darling, R. B., Bohringer, K. F., Donald, B. R., Baltes, H., Kovacs, G. T. *Fully programmable mems ciliary actuator arrays for micromanipulation tasks*. in *'00 IEEE international conference on robotics and automation*. 2000.

71. Mohebbi, M.H., Terry, M. L., Bohringer, K. F. *Omnidirectional walking microrobot realized by thermal microactuator arrays*. in *Proceedings of 2001 ASME international mechanical engineering congree and exposition*. 2001. New York, NY.

72. Ataka, M., Omodaka, A., Takeshima, N., Fujita, H., *Fabrication and operation of polyimide bimorph actuators for a ciliary motion system.* Journal of microelectromechanical systems, 1993. **2**(4): p. 146.

73. Kladitis, P.E., Bright, V. M., *Prototype microrobots for micro-positioning and micro-unmanned vehicles.* Sensors and Actuators, 2000. **80**: p. 132.

74. Bohringer, K.F., Donald, B. R., MacDonald, N. C., Kovacs, T. A., Suh, H. W., *computational methods for design and control of mems micromanipulator arrays.* Computational science and engineering, IEEE, 1997. **4**(1): p. 17.

75. Shu, J.W., Glander, S. F., Darling, R. B., Storment, C. W., Kovacs, G. T. A., *Organic thermal and electrostatic ciliary microactuator array for object manipulation.* Sensors and Actuators A, 1997. **58**: p. 51.

76. Luo, J.K., et al., *Comparison of microtweezers based on three lateral thermal actuator configurations.* Journal of Micromechanics and Microengineering, 2005. **15**(6): p. 1294-1302.

77. Kim, K., et al., *Metallic microgripper with SU-8 adaptor as end-effectors for heterogeneous micro/nano assembly applications.* Microsystem Technologies-Micro- and Nanosystems-Information Storage and Processing Systems, 2004. **10**(10): p. 689-693.

78. Krulevitch, P., Lee, A. P., Ramsey, P. B., Trevino, J. C., Hamilton, J., Northrup, M. A., *Thin film shape memory alloy microactuators.* Journal of microelectromechanical systems, 1996. **5**(4): p. 270.

79. Darling, R.B., Suh, J. W., Kovacs, T. A., *Ciliary microactuator array for scanning electron microscope positioning stage.* J. Vac. Sci. Technol. A, 1998. **16**(3): p. 1998.

80. Tabata, O., Hirasawa, H., Aoki, S., Yoshida, R., Kokufuta, E., *Ciliary motion actuator using self-oscillating gel.* Sensors and Actuators A, 2002. **95**: p. 234.

81. Ok, J., Chu, M., Kim, C-J. *Pneumatically driven microcage for micro-objects in biological liiquid*. in *Twelfth IEEE international conference on Micro Electro Mechanical Sysmtes*. 1999.

82. Luo, J.K., et al., *Fabrication and characterization of diamond-like carbon/Ni bimorph normally closed microcages.* Journal of Micromechanics and Microengineering, 2005. **15**(8): p. 1406-1413.

83. Takeda, M. *Applications of MEMS to industrial inspection*. in *The 14th international conference on Micro Electro Mechanical Systems*. 2001.

84. Dariot, P., Valleggi, R., Carrozza, M. C., Montesi, M. C., Cocco, M., *Microactuators for microrobots: a critical survey.* J. Micromech. Microeng., 1992. **2**: p. 141.

85. Komvopoulos, K., *Adhesion and friction forces in microelectromechanical systems: mechanisms, measurements, surface modification techniques, and adhesion theory.* J. Adhesion Sci. Technol., 2003. **17**(4): p. 477.

86. Tambe, N.S., Bhushan, B., *Scale dependence of micro/nano-friction and adhesion of MEMS/NEMS materials, coatings and lubricants.* Nanotechnology, 2004. **15**: p. 1561.

87. Scherge, M., Li, X., Schaefer, J. A., *The effect of water on friction of MEMS.* Tribol. Lett., 1999. **6**: p. 215.

88. Mastrangelo, C.H., *Adhesion-related failure mechanisms in micromechanical devices.* Tribol. Lett., 1997. **3**: p. 223.

89. Rymuza, Z., *Control tribological and mechanical properties of MEMS surfaces. Part1:critical review.* Microsystem Technologies, 1999. **5**: p. 173.

90. Maboudian, R., Ashurst, W. R., Carraro, C., *Self-assembled monolayers as anti-stiction coatings for MEMS: characteristics and recent developments.* Sensors and Actuators, 2000. **82**: p. 219.

91. Akiyama, T., Shono, K., *Controlled stepwise motion in polysilicon microstructures.* Journal of microelectromechanical systems, 1993. **2**(3): p. 106.

92. Akiyama, T., Collard, D., Fujita, H., *Scratch drive actuator with mechanical links for self-assembly of three-dimensional MEMS.* Journal of microelectromechanical systems, 1997. **6**(1): p. 10.

93. Donald, B.R., Levey, C. G., McGray, C. D., Rus, D., Sinclair, M., *Power delivery and locomotion of untethered microactuators.* Journal of microelectromechanical systems, 2003. **12**(6): p. 947.

94. Donald, B.R., Christopher, G. L., McGray, C. D., Rus, D., Sinclair, M., *Untethered micro-actuators for autonomous micro-robot- locomotion: Design, fabrication, control, and performance*. 2003: Springer-Verlag.

95. Donald, B.R., Levey, C. G., McGray, C. D., Rus, D., Paprotny, I., *An untethered, electrostatic, globally controllable MEMS micro-robot.* Journal of microelectromechanical systems, 2006. **15**(1): p. 1.

96. Dreyfus, R., Baudry, J., Roper, M. L., Fermigier, M., Stone, H. A., Bibette, J., *Microscopic artificial swimmers.* Nature, 2005. **437**(6): p. 862.

97. Ehrenhaft, F., Annalen der physic, 1918. **56**(10): p. 81.

98. Greene, W.M., Journal of optical society of america, B, 1985. **2**(6): p. 998.

99. Zhao, B., Katoshevski, D., Bar-Ziv, E., Meas. Sci. Techno., 1999. **10**: p. 1222.

100. Ghernyak, V.G., Klitenik, O. V., Phys. Rev. E, 203. **68**: p. 061205.

101. Hirai, A., Monjushiro, H., Watarai, H., Langmuir, 1996. **12**: p. 5570.

102. Janssen, G.C.A.M., Kamminga, J. D., *Stress in hard metal films.* Applied Physics Letters, 2004. **85**(15): p. 3086.

103. Chen, S.T., Yang, C. H., Faupel, F., Ho, P. S., *Stress relaxation during thermal cycling in metal/polyimide layered films.* J. Appl. Phys., 1988. **64**(12): p. 6690.

104. Hodge, T.C., Bidstrup-Allen, S. A., Kohl, P. A., *Stresses in thin film metallization.* IEEE Transcations on components, packaging, and manufacturing technology - Part A., 1997. **20**(2): p. 241.

105. Planck, M., *Zur theorie des gesetzes der energieverteilung im normalspektrum.* Verhandl. Duetsch. phys. Ges., 1900. **2**: p. 237.

106. Ruan, J.A., Bhushan, B., J. Appl. Phys., 1994. **76**(9): p. 5022.

107. Dienwiebel, M., Verhoeven, G. S., Pradeep, N., Frenken, J. W. M., Phys. Rev. Lett., 2004. **92**(12): p. 126101-1.

108. Ostrach, S., *An analysis of laminar free-convection flow and heat transfer about a flat plate parallel to the direction of the generationg body force.* National Advisory Comittee for Aeronautics, 1953. **Report 1111**: p. 63.

109. Kierkus, W.T., Int. J. Heat Mass Transfer, 1968. **11**: p. 241.

110. Bauerle, D., *Laser processing and chemistry*. 2 ed. 1996: Springer.

111. Gushterova, P., *On determination of optical constants of very thin metallic films.* 2005.

112. Incropera, F.P., *Fundamentals of heat and mass transfer*. 5th ed. 2002: John Wiley & Sons.

113. Falvo, M., *Gearlike Rolling Motion Mediated by Commensurate Contact: Carbon Nanotubes on HOPG.* Phys. Rev. B, 2000. **62**(16): p. R10665.

114. Schwarz, U.D., Zworner, O., Koster, P., Wiesendanger, R., *Quantitative analysis of the frictional properties of solid materials at low loads. I. Carbon compounds.* Phys. Rev. B, 1997. **56**(11): p. 6987.

115. Suh, J.W., Glander, S. F., Darling, R. B. Storment, C. W., Kovacs, G. T. A., *Organic thermal and electrostatic ciliary microactuator array for object manipulation.* Sensors and Actuators, A, 1997. **58**: p. 51.

116. Suh, J.W., Darling, R. B., Bohringer, K. F., Donald, B. R., Baltes, H., *CMOS integrated ciliary actuator array as a general-purpose micromanipulation tool for small objects.* J. Microelectomech. Sys., 1999. **8**(4): p. 483.

117. Ruffieux, D., de Rooij, N. F. *A 3DOF bimorph actuator array capable of locomotion*. in *13th Eur. Conf. on solid-state transducers*. 1999. Hague, The Netherlands.

118. Ressejac, I.C., Landsberger, L.. M., Currie, J. F., *Bistable microelectrothermal actuator in a standard complementary metal-oxide-semiconductor process.* J. Vac. Sci. Technol. A, 1999. **18**(2): p. 746.

119. Lin, G., Kim, C. J., Konishi, S., Fujita, H. *Design, fabrication, and testing of a C-shape actuator*. in *The 8th international conference on solid state sensors and actuators, and eurosensors IX*. 1995. Stockholm, Sweden.

120. Haga, Y.Y., Y. Esashi, M. *Small diameter active catheter using shape memory alloy*. in *Proceedings of microelectromechanical systems, MEMS98, The eleventh annual international workshop*. 1998.

121. Park, K.T., Esashi, M., *A multilink active catheter with polyimide-based integrated CMOS interface circuits.* Journal of microelectromechanical systems, 1999. **8**(4): p. 349.

122. Yang, J.P., Deng, X. C., Chong, T. C., *A self-sensing thermal actuator incorporating micromirror for tracking mechanism of optical drive.* Sensors, 2004, Proceedings of IEEE, 2004. **2**: p. 900.

123. Bonvilain, A., Chaillet, N. *Microfabricated thermally actuated microrobot*. in *Procedings of the 2003 IEEE international conference on robotics & automation*. 2003. Taipei, Taiwan.

124. Stoney, G.G., *The tension of metallic films deposited by electrolysis.* Nature, 1908. **August, 20**: p. 366.

125. Timoshenko, S.J., J. Opt. Soc. Am., 1925. **11**: p. 233.

126. Gehring, G.A., Cooke, M. D., Gregory, I. S., Karl, W. J., Watts, R., *Cantilever unified theory and optimization for sensors and actuators.* Smart Mater. Struct., 2000. **9**: p. 918.

127. For more information on the Tube Tracer, v.t.w.h.w.c.u.e.R.n.c.d.t.i.h.

128. For the information on the software "Video Spot Tracker" check here, h.w.c.u.e.R.n.c.d.s.v.s.t.h.

129. Falvo, M., *Nanoscale-scale Rolling and Sliding of Carbon Nanotubes.* nature, 1999. **397**(6716): p. 236.

130. Cumings, J., Zettle, A., *Low-friction nanoscale linear bearing realized from multiwall carbon nanotubes.* Science, 2000. **289**: p. 602.

131. Schwarz, U.D., et al., *Quantitative analysis of the frictional properties of solid materials at low loads .1. Carbon compounds.* Physical Review B, 1997. **56**(11): p. 6987-6996.

132. Bhushan, B., Israelachvili, J. N., Landman, U., *Nanotribology: friction, wear and lubrication at the atomic scale.* Nature, 1995. **374**(6523): p. 607.

133. Binggeli, M., Mate, C. M., *Influence of Capillary Condensation of Water on Nanotribology studied by force microscopy.* Appl. Phys. Lett., 1994. **65**(4): p. 415.

134. Binggeli, M., Mate, C. M., *Influence of water vapor on nanotribology studied by friction force microscopy.* J. Vac. Sci. Technol. B, 1995. **13**(3): p. 1312.

135. Sirghi, L., *Effect of capillary-condensed water on the dynamic friction force at nanoasperity contacts.* Appl. Phys. Lett., 2003. **82**(21): p. 3755.

136. Ohmichi, O., Yamagata, Higuchi, T., *Micro impact drive mechanisms using optically excited thermal expansion.* Journal of microelectromechanical systems, 1997. **6**(3): p. 200.

137. Li, F., et al., *Tensile strength of single-walled carbon nanotubes directly measured from their macroscopic ropes.* Applied Physics Letters, 2000. **77**(20): p. 3161-3163.

138. Walters, D.A., et al., *Elastic strain of freely suspended single-wall carbon nanotube ropes.* Applied Physics Letters, 1999. **74**(25): p. 3803-3805.

139. Wong, W.E., Sheehan, P. E., Lieber, C. M., *Nanobeam Mechanics: Elasticity, Strength, and Toughness of Nanorods and Nanotubes.* 1997. **277**: p. 1971.

140. Shi, Z.J., et al., *Large scale synthesis of single-wall carbon nanotubes by arc-discharge method.* Journal of Physics and Chemistry of Solids, 2000. **61**(7): p. 1031-1036.

141. Ajayan, P.M., P. Redlich, and M. Ruhle, *Balance of graphite deposition and multishell carbon nanotube growth in the carbon arc discharge.* Journal of Materials Research, 1997. **12**(1): p. 244-252.

142. Li, C. and W.L. Guo, *Continuum mechanics simulation of post-buckling of single-walled nanotubes.* International Journal of Nonlinear Sciences and Numerical Simulation, 2003. **4**(4): p. 387-393.

143. Hur, S.H., O.O. Park, and J.A. Rogers, *Extreme bendability of single-walled carbon nanotube networks transferred from high-temperature growth substrates to plastic and their use in thin-film transistors.* Applied Physics Letters, 2005. **86**(24): p. -.

144. Winau, D., Koch, R., Fuhrmann, A., Rieder, K. H., *Film growth studies with intrinsic stress measurement: Polycrystalline and epitaxial Ag, Cr, and Au films on mica(001).* J. Appl. Phys., 1991. **70**(6): p. 3081.

145. Irene, E.A., Tierney, E., Angilello, J., *A viscous flow model to explain the appearance of high density thermal SiO2 at low oxidation temperatures.* J. Electrochem. Soc., 1982. **129**: p. 2594.

146. Koreo, K., *Recent developments in the study of mechanical properties of thin films.* Thin Solid Films, 1972. **12**(1): p. 17.

147. d'Heurie, F.M., *Aluminum films deposited by RF sputtering.* Metallurgical Trans., 1970. **1**: p. 725.

148. Flinn, P.A., Gardner, D. S., Nix, W. D., *Measurement and interpretation of stress in aluminum-based metallization as a function of thermal history.* IEEE Transcations on electron devices, 1987. **34**(3): p. 689.

149. Flinn, P.A., *Measurement and interpretation of stress in copper films as a fucntion of thermal history.* J. Mater. Res., 1991. **6**(7): p. 1498.

150. de Lima, M.M., Jr., Lacerda, R. G., Vilcarromero, J., Marques, F. C., *Coefficient of thermal expansion and elastic modulus of thin films.* Journal of Applied Physics, 1999. **86**(9): p. 4936.

151. Jamting, A.K., Bell, J. M., Swain, M. V., Schwarzer, N., *Investigation of the elastic modulus of thin films using simple biaxial bending techniques.* Thin Solid Films, 1997. **308**: p. 304.

152. Lee, S.H., Evans, J. W., Pak, E., Jeon, J. U., and Kwon, D., *Evaluation of elastic modulus and yield strength of Al film using an electrostatically actuated test device.* Thin Solid Films, 2002. **408**: p. 223.

153. Son, D., Jeong, J-H., Kwon, D., *Film-thickness considerations in microcantilever-beam test in measuring mechanical properties of metal thin film.* Thin Solid Films, 2003. **437**: p. 182.

154. Lu, J.P., *Elastic properties of single and multilayered nanotubes.* J. Phys. Chem. Solids, 1997. **38**(11): p. 1649.

155. Lu, J.P., *Elastic Properties of Carbon Nanotubes and Nanoropes.* Phys. Rev. Lett., 1997. **79**(7): p. 1297.

156. Li, C., *Elastic moduli of multi-walled carbon nanotubes and the effect of van der Waas forces.* Composites Science and Technology, 2003. **63**: p. 1517.

157. Tu, Z.-C., *Single-walled and multiwalled carbon nanotubes viewed as elastic tubes with the effective Young's moduli depednt on layer number.* Phys. Rev. B, 2002. **65**: p. 233407.

158. Salvetat, J.-P., Briggs, G. A. D., Bonard, J-M., Bacsa, R. R., kulik, A. J., *Elastic and shear moduli of single-walled carbon nanotube ropes.* Phys. Rev. Lett., 1999. **82**(5): p. 944.

159. Chang, T., Gao, H., *Size-dependent elastic properties of a single-walled carbon nanotube via a molecualr mechanics model.* Journal of the Mechanics and Physic of Solids, 2003. **51**: p. 1059.

160. Chang, T., Geng, J., Guo, X., *Chirality- and size-depedent elastic properties of single-walled carbon nanotubes.* Applied Physics Letters, 2005. **87**: p. 251929.

161. Griffin, A.J., Jr., Brotzen, F. R., *Mechanical testing of thin metal films.* Thin Solid Films, 1992. **220**: p. 265.

162. Lacour, S.P., Wagner, S., Huang, Z., Suo, Z., *Stretchable gold conductors on elastomeric substrates.* Applied Physics Letters, 2003. **82**(15): p. 2404.

163. Lacour, S.P., Jones, J., Wagner, S., Li, T., Suo, Z., *Stretchable interconnects for elastic electronic surfaces.* Proceddings of the IEEE, 2005. **93**(8): p. 1459.

164. Spaepen, F., *Interfaces and stresses in thin films.* Acta. Mater., 2000. **48**: p. 31.

165. Schell-Sorokin, A.J., and Tromp, R. M., *Mechanical stresses in (sub) monolayer epitaxial films.* Phys. Rev. Lett., 1990. **64**(9): p. 1039.

166. Wedler, G., Walz, J., Hesjedal, T., Chilla, E., Koch, R., *Intrinsic stress upon Stranski-Krastanov growth of Ge on Si(001).* Surface Science, 1998. **402-404**: p. 290.

167. Zhao, J.-H., Du, Y., Morgen, M., Ho, P. S., *Simultaneous measurement of Young's modulus, Poisson ratio, and coefficient of thermal expansion of thin films on substrates.* Journal. of Applied Physics, 2000. **87**(3): p. 1575.

168. Kwon, Y.K., Berber, S., Tomanek, D., *Thermal contraction of carbon fullerences and nanotubes.* Physical Review Letters, 2004. **92**(1): p. 015901-1.

169. Ikuno, T., Honda, S., Yasuda, T., Oura, K., Katayama, M., Lee, J. G., Mori, H, *Thermally driven nanomechanical deflection of hybrid nanowires.* Applied Physics Letters, 2005. **87**: p. 213104.

170. Vinci, R., Vlassak, J. J., *Mechanical behavior of thin films.* Annu. Rev. Mater. Sci., 1996. **26**: p. 431.

171. Villain, P., Goudeau, P., Renault, P. O., Badawi, K. F., *X-ray diffraction study of thin film elastic properties.* Advanced Engineering Materials, 2002. **4**(8): p. 554.

172. Sato, S., Kawabata, A., Nihei, M., Awano, Y., *Growth of diameter-controlled carbon nanotubes using monodisperse nickel nanoparticles obtained with a differential mobility analyzer.* Chemical Physics Letters, 2003. **382**: p. 361.

173. Yuan, Z.-H., Huang, H., Liu, L, Fan, S-S., *Controlled growth of carbon nanotubes in diameter and shape using template-synthesis method.* Chemical Physics Letters, 2001. **345**: p. 39.

174. Ahir, S.V., A.R. Tajbakhsh, and E.M. Terentjev, *Self-assembled shape-memory fibers of triblock liquid-crystal polymers.* Advanced Functional Materials, 2006. **16**(4): p. 556-560.

175. Peng, F., Wang, H. J., *Study on diameter controlled growth of carbon nanotubes by LaAl1_xFex03 catalysts.* Chemical Research in chinese universities, 2005. **21**(1): p. 4.

176. Bauelrle, D., *Laser processing and chemistry*. 2nd ed.

177. Churchill, S.W., Chu, H. H. S., *Correlating equations of laminar and turbulent free convection from a vertical plate.* Int. J. Heat Mass Transfer, 1975. **18**: p. 1323.